The Effect of Atmosphere on Lead Halide Perovskites

by

Roberto Brenes

B.S. Massachusetts Institute of Technology (2017)

Submitted to the Department of Electrical Engineering and Computer Science
in partial fulfillment of the requirements for the degree of

Master of Engineering in Electrical Engineering and Computer Science

at the

MASSACHUSETTS INSTITUTE OF TECHNOLOGY

February 2019

Author .....
Department of Electrical Engineering and Computer Science
January 29, 2019

Certified by .....
Vladimir Bulović
Professor of Electrical Engineering and Computer Science
Thesis Supervisor

Accepted by .....
Katrina LaCurts
Chair, Master of Engineering Thesis Committee

The Effect of Atmosphere on Lead Halide Perovskites

by

Roberto Brenes

Submitted to the Department of Electrical Engineering and Computer Science
on January 29, 2019, in partial fulfillment of the
requirements for the degree of
Master of Engineering in Electrical Engineering and Computer Science

Abstract

Metal halide perovskites are exciting materials for low-cost optoelectronic devices such as solar cells and LEDs. At present, perovskite materials still suffer from substantial non-radiative decay, particularly under solar illumination conditions, and are therefore yet to reach their full potential. In this thesis, we demonstrate the use of light and atmospheric treatments on polycrystalline perovskite films, resulting in minimal non-radiative losses and properties approaching those of perovskite single crystals and even the best crystalline semiconductors reported to date. We show that by combining light and atmospheric treatments, we can increase the internal luminescence quantum efficiencies of polycrystalline perovskite films from 1% to 89%, with carrier lifetimes of 32 μs and diffusion lengths of 77 μm, comparable with perovskite single crystals. Remarkably, the surface recombination velocity of holes in the treated films is 0.4 cm/s, approaching the values for passivated crystalline silicon, which has the lowest values for any semiconductor to date. The enhancements translate to solar cell power-conversion efficiencies of 19.2%, with a near-instant rise to stabilized power output, consistent with suppression of ion migration. Also, we use in-situ microphotoluminescence measurements to elucidate the impact of light-soaking individual methylammonium lead iodide grains while immersing them with different atmospheric environments. We show that emission from each grain depends sensitively on both the environment and the nature of the specific grain, i.e., whether it shows good (bright grain) or poor (dark grain) luminescence properties. We find that the dark grains show substantial rises in emission, while bright grain emission is steady when illuminated in the presence of oxygen and/or water molecules. We find that oxygen molecules bind particularly strongly to surface iodide vacancies which, in the presence of photoexcited electrons, lead to efficient passivation of the carrier trap states that arise from these vacancies. This thesis reveals a unique insight into the nature of nonradiative decay and the impact of atmospheric passivation on the macro- and micro-scale properties of perovskite films.

Thesis Supervisor: Vladimir Bulović
Title: Professor of Electrical Engineering and Computer Science

Acknowledgments

I want to thank, first and foremost, my parents Fernando and Adelita for all their support throughout my life. Without their love, education and guidance I would not be anywhere close to where I am now. It also would not have been possible without the unconditional love from my siblings, Eduardo, Nano and Carolina who are an integral part of my life. Bhalu, my dog, should also get a mention for making our home even happier than what it already was.

Tuto, Dan, Thomas and all my other friends, thank you for being an invaluable part of my life and for all the support throughout this whole process.

I would also like to thank my advisors, Vladimir Bulović and Samuel Stranks for their guidance throughout undergraduate and graduate life. Their drive and support has been second to none in pushing me to be better scientist.

This work was completed with the help of all my past and present coworkers in ONELab, whom I would like to acknowledge for the valuable discussions, advice and all the enjoyable moments we have spent together. Maddie, Dane, Panda, Melissa, Michel, Joel, Max, Rich, Mayuran, Farnaz, Mengfei, Ella, Ryan, Tom, Anna, Annie, Melany, Melody and all the others, I want to thank you for being an important part of my academic life.

Finally, I would like to acknowledge all of those outside of MIT who have contributed to these projects and made this thesis possible: Sandeep Pathak, Eline Hutter, Saiful Islam, Nakita Noel, Christopher Eames, Dengyang Guo, Henry Snaith, Tom Savenije and Sir Richard Friend.

Contents

1 Introduction **29**

1.1 Confocal Microscopy 30

1.2 Time-correlated single photon counting 34

1.3 Thesis Outline 36

2 Metal Halide Perovskite Polycrystalline Films Exhibiting Properties of Single Crystals **37**

2.1 Introduction 37

2.2 Results 38

2.2.1 Macro- and Micro-photoluminescence Enchancements 38

2.2.2 Enhancements in Film Photoconductance and Diffusion Length 41

2.2.3 Enhancements in Solar Cell Device Performance 45

2.2.4 Mechanism of Photobrightening 47

2.3 Discussion 48

2.4 Experimental Procedures 50

2.4.1 Sample Preparation 50

2.4.2 Macro-photoluminescence Measurements 51

2.4.3 Micro(Confocal)-photoluminescence Measurements 52

2.4.4 Time-Resolved Microwave Conductivity Measurements 52

2.4.5 Device Fabrication and Characterization 53

3 The Impact of Atmosphere on the Local Luminescence Properties of Metal Halide Perovskite Grains **57**

3.1 Introduction . . . 57
3.2 Results . . . 60
3.2.1 Local Grain Luminescence Under N_2 . . . 60
3.2.2 Local Grain Luminescence Under O_2 . . . 61
3.2.3 Local Grain Luminescence After Humidity Exposure . . . 63
3.2.4 Density Functional Theory Calculations . . . 65
3.3 Discussion . . . 68
3.4 Experimental Section . . . 70
3.4.1 Photoluminescence Measurements . . . 70
3.4.2 Ab-initio Calculations . . . 71

4 Conclusion **73**

A Supplementary Information to Chapter 2 **75**
A.1 Kinetic Model . . . 75
A.2 Importance of combination of light, oxygen and humidity . . . 82
A.3 Sensitivity of reported values . . . 100
A.4 Extracting relative fractions of k_R and k_n . . . 102
A.5 Surface recombination velocity . . . 103
A.6 Ab-initio calculations . . . 103
A.7 Surface characterization . . . 104
A.8 Device external quantum efficiency (EQE) measurements . . . 105

B Supplementary Information to Chapter 3 **107**

List of Figures

1-1 Standard confocal microscope setup as depicted by Semwogerere et al.[71]. 31

1-2 Left: Airy Disc intensity distribution. Right: Intensity distribution p_{conf} for a typical confocal setup. Plots from Robert H. Webb[88]. . . 33

1-3 a) Scheme for measuring photon arrival times. b) Histogram built from the photon arrival times [86]. 35

1-4 Typical TCSPC setup as detailed by Michael Wahl. An ND filter is used to reduce the intensity of the laser and a cutoff filter (normally a dichroic filter) to remove any scattered light from the laser and only collect the wavelengths of interest [86]. 35

2-1 *Macro- and Micro-photoluminescence Enhancements of Thin Films under Solar Illumination Conditions* (a–c) Internal PLQE η measurements over time under illumination with a CW 532-nm laser at an excitation intensity equivalent to 2 sun (150 mW/cm^2) in dry N2 (a), dry air (b), and humid air (c). Inset: Time-resolved PL decays of the films after the stated treatment with pulsed excitation at 405 nm (excitation density of 5.4×10^{15}cm^{-3}). (d–h) In situ confocal PL maps with 405-nm excitation measured in (d) dry air, (e) humidified air, (g) after light soaking for 10 min under excitation with a 532-nm laser equivalent to 10 sun under humid air, (g) after returning to dry air, and (h) measured the next day with storage in dry air. Insets to (d) and (g): emission stability of the films in dry air before and after the treatment, respectively, with excitation at 532-nm at intensity equivalent to 10 sun. 40

2-2 *Enhancements in Film Photoconductance Determined from Time-Resolved Microwave Conductivity Measurements* (a) Photoconductance measurements for a $MAPbI_3$ film after storage in dry air and after being subjected to light soaking for 30 min in humid air (40% humidity) under a constant photon flux similar to solar conditions. The TRMC trace taken after storing the same sample in a nitrogen glove box for a week after the treatment is also shown. The TRMC decays were recorded by photo-exciting the samples in dry N_2 with pulsed illumination at 500 nm and an excitation density of 5×10^{14}cm^{-3}. (b) TRMC decays (normalized to absorbed flux) of the treated samples with the initial charge excitation density as indicated. (c) Dashed lines are fits to the data using the trap model summarized in (c), where G_c is the generation rate and k_T and k_D are the trapping and trap recombination rates, respectively. (d) Diffusion lengths of the electrons and holes before and after the treatments. 42

2-3 *Enhancements in Solar Cell Device Performances* (a) Light and dark J-V curves of champion devices for the devices containing untreated (stored in dry air) and treated (light soaked in humid air) films measured under AM1.5 100 mW/cm^2 simulated sunlight. (b) Stabilized power output of the devices presented in (a) measured by holding the devices at their maximum power point (as determined from J-V curves) for 50 s. 46

2-4 *Mechanism of Photobrightening* (a) Schematic showing non-radiative recombination (k_n) dominating owing to shallow surface states, which are removed in the treatment to lead to radiative-dominant (k_R) recombination. (b–d) Untreated $MAPbI_3$ films (b) containing non-radiative trap states that are passivated by exposure of $MAPbI_3$ to (c) light and oxygen and (d) light, oxygen, and water. 49

3-1 *Microscale photoluminescence properties in dry and humid nitrogen.* (a) Confocal PL map of a $MAPbI_3$ perovskite film in dry nitrogen normalised to the maximum intensity. (b, c) Monitoring the PL intensity (emission count rate) over time under illumination from (b) a bright grain (blue circle in a) and (c) a dark grain (pink circle in a) under dry nitrogen and under humidified (45% relative humidity) nitrogen. The PL intensity for each trace over time is given relative to the starting value for the bright grain in nitrogen, which is normalised to 1. (d, e) PL decays from the same (d) bright and (e) dark grains under dry nitrogen, and before and after light soaking in humidified nitrogen. Samples were photoexcited with a 405 nm laser with a repetition rate of 0.5 MHz and a fluence of $\sim$ 1 μJ/cm^2/pulse ($\sim$500 mW/cm^2), and this same laser was used for local light-soaking (total photon dose of $\sim$150 J/cm^2). 61

3-2 *Microscale photoluminescence properties in dry and humid air.* (a) Confocal PL map of a $MAPbI_3$ perovskite film in dry air normalised to the maximum intensity. (b, c) Monitoring the emission (PL count rate) over time under illumination from (b) a bright grain (blue circle in a) and (c) dark grain (pink circle in a) under dry air and under humidified (45% relative humidity) air. The PL intensity for each trace over time is given relative to the starting value for the bright grain in air, which is normalised to 1. (d, e) PL decays from the same (d) bright and (e) dark grains under dry air before and after the light-soaking. (f, g) PL decays from the same (f) bright and (g) dark grains under dry air, humidified air, and after the light-soaking in humidified air. Samples were photoexcited with a 405 nm laser with a repetition rate of 0.5 MHz and a fluence of $\sim$1 μJ/ cm^2/pulse ($\sim$500 mW/cm^2), and this same laser was used for local light-soaking (total photon dose of $\sim$150 J/cm^2). 62

3-3 *Local grain emission stability after humidity exposure.* (a) Confocal PL map of a $MAPbI_3$ perovskite film in dry air following exposure to humid air for 60 minutes, normalised to the same intensity value as Fig. 3-2A to allow direct comparison. (b) Monitoring the emission intensity (count rate) from various bright and dark grains denoted in (a) over time under illumination, normalised to the intensity of the same grain as in Fig. 3-2b. Inset: emission from the same grains under continuous illumination before the exposure to humidity. (c) Confocal PL map of a $MAPbI_3$ perovskite film in dry nitrogen following exposure to humid nitrogen for 60 minutes, normalised to the same intensity value as Fig. 3-1a. (d) Monitoring the emission intensity (count rate) from various bright and dark grains denoted in (c) over time under illumination, normalised to the intensity of the same grain as in Fig. 3-1b. Samples were photoexcited with a 405 nm laser with a repetition rate of 0.5 MHz and a fluence of $\sim$1 $\mu J/cm^2$/pulse ($\sim$500 mW/cm^2), and this same laser was used for local lightsoaking (total photon dose of $\sim$150 J/cm^2). 64

3-4 *Surface atomic and electronic structures.* Schematic of the local atomic-scale configurations of the surface termination layer (top row) and calculated band structures (bottom row) for the (110) surface of $MAPbI_3$. (a) Pristine uncharged surface, (b) negatively-charged iodine vacancy into which the following molecules are adsorbed; (c) N_2, (d) H_2O and (e) O_2. Key: purple - iodine, grey - lead, blue - nitrogen, red - oxygen, white - hydrogen. We note that our calculations explicitly included excess electrons; hence the Fermi level (red line) is above any trap states because those states are filled. See Figures B-6 to B-9 for other configurations. 68

A-1 Schematic of the recombination and generation pathways in the kinetic model (a) with photon recycling and (b) when excluding the effects of photon recycling. G_c is the generation rate, k_R is the radiative bimolecular rate, k_n is the non-radiative bimolecular rate, k_T is the trapping rate, k_D is the trap depopulation rate, N_t is the deep trap density, p_0 is the background hole density [39], η_{esc} is the escape probability of photons [68]. 76

A-2 (a-d) External PLQE η_{meas} measurements over time under illumination with a 532-nm laser at an excitation intensity equivalent to ∼2 sun (∼150 mW/cm^2) in (a) dry nitrogen, (b) dry compressed air, (c) humidified compressed air, and (d) after returning to dry compressed air. (e-h) show the same plots but after converting the external values to internal PLQE η. 77

A-3 Time-resolved PL decays of the (a) untreated (dry N_2) and (b) treated (humid air + light, where light is equivalent to 1 sun illumination intensities) samples. Samples were excited with a 405-nm pulsed laser with the stated excitation densities (realized through use of optical filters) and a repetition rate of 20 kHz. 78

A-4 In-situ confocal PL maps measured in (a) dry N_2, and (b) after light soaking for 10 minutes under excitation with a 532-nm laser equivalent to ∼10 sun under dry N_2. (c-d) Show the same measurements under dry air. PL maps were collected by photo-exciting with a 405-nm laser with a repetition rate of 0.5 MHz and a fluence of ∼1 μJ/cm^2/pulse. 79

A-5 (a) Emission of the films in Figure A-4a and c in dry air and dry nitrogen during the light-soaking with excitation at 532-nm and intensity equivalent to ∼10 sun. (b, c) Histograms showing the distribution of average lifetimes corresponding to the respective maps in Figure A-4. (d, e) Histograms showing the distribution of emission intensities corresponding to the respective maps in Figure A-4. 80

A-6 (a) Emission of the films in Fig. 2-1d-h during the light-soaking with excitation at 532-nm and intensity equivalent to ∼10 sun under the stated atmospheric conditions. (b) The PL decays summed across the map before the treatment (cf. Fig. 2-1d) and after the treatment with light, air and humidity (cf. Fig. 2-1g). The corresponding distributions of the average lifetime and intensity are shown in (c) and (d), respectively. 81

A-7 PL stability immediately after the treatment (red) and after 3 weeks of storage in a nitrogen-filled glove box for a (a) bare film and (b) film coated with a spin-coated layer of PMMA. 82

A-8 In-situ confocal PL maps measured in (a) dry air, (b) humidified air, (c) after returning to dry air (i.e. without any light soaking). PL maps were collected by photo-exciting with a 405-nm laser with a repetition rate of 0.5 MHz and a fluence of ∼1 μJ/cm^2/pulse. (d) Histograms of the intensity distribution of each map. These distributions should be compared to those in Figure A-6, where illumination under humidity leads to substantial increases in the intensity. 83

A-9 External PLQE η_{meas} measurements over time under illumination with a 532-nm laser at an excitation intensity equivalent to ∼2 sun (∼150 mW/cm^2) in nitrogen (black) and compressed air (red) under (a) dry conditions, (b) humid conditions, and (c) after returning to dry conditions. The effects are far better retained for the sample light-soaked in air and humidity. 84

A-10 PL measurements over time under illumination with a 532-nm laser at an excitation intensity equivalent to ∼2 sun (∼150 mW/cm^2) in humidified air (45% RH) showing a decrease in emission at longer times. 85

A-11 (a) Photoconductance measurements for a $MAPbI_3$ film after storage in dry nitrogen and then after being subjected to light-soaking for 30 minutes in dry nitrogen under a white light LED source generating a similar photon flux to AM1.5 sunlight. The TRMC decays were taken by photo-exciting the samples in dry N_2 with pulsed illumination at 500 nm and an excitation density of $4.75 \times 10^{14}cm^{-3}$. The inset shows the half lifetimes of the corresponding decays at different excitation densities (other decays not shown here). The other panels show similar measurements but under the stated atmosphere and conditions, i.e. (b) humid nitrogen (40% relative humidity) (excitation density of $4.93 \times 10^{14}cm^{-3}$), (c) dry air (excitation density of $3.87 \times 10^{14}cm^{-3}$) and (d) humid air (40% relative humidity) (excitation density of $5.07 \times 10^{14}cm^{-3}$). Panels b and d also show the decays taken after storing the same sample in a nitrogen-filled glove box for various times after treatment. 86

A-12 Excitation-dependent TRMC decays of the (a) untreated samples and (b) samples 1 week after treatment (with storage in a nitrogen-glove box in between), with the initial charge excitation density (pulsed illumination at 500 nm) as shown in the legends. Dashed lines are fits to the data using the trap model described in Chapter 2. The corresponding data for the freshly-treated sample are shown in Figure 2-2b 87

A-13 The effective TRMC decay curves for each stated treatment for electrons (dashed lines) and holes (solid lines) decoupled using the rate equations in the trapping model incorporating electron traps N_t [7] (Scheme A-1) when including photon recycling ($k_2^{eff} = \eta_{esc}k_R + k_n$) (a-c) and when subtracting off the effects of photon recycling ($k_2^{int} = k_R + k_n$) (d-f). 88

A-14 Half lifetime of the electron and holes extracted from the decays in Figure A-13a-c with photon recycling (a) and Figure A-13d-f without photon recycling (b). We use these lifetimes to calculate the resulting diffusion length of each carrier using $L_D = \sqrt{k_B T \mu \tau_{1/2}/e}$, where k_B is the Boltzmann constant, T the temperature, e the electron charge and μ the mobility extracted from the photo-conductance measurements. The diffusion lengths are shown with (c) and without photon recycling (d). The diffusion lengths in the former case are interpreted as the cumulative diffusion length of a charge carrier including photon recycling events (but not including distance travelled by photons until reabsorption), while the latter is interpreted as the diffusion length of a charge carrier from initial excitation to first recombination event. 89

A-15 (a) Light and dark J-V curves of champion devices for the devices containing acetonitrile-based films stored in dry air, humid air (45% relative humidity), and light-soaked under dry air and humid air for 20 minutes with a white light LED array with an intensity similar to simulated sunlight. Device measurements were taken under AM1.5 100mW/cm^2 simulated sunlight and the presented scans were measured scanning from 1.4 V to 0 V (open-circuit to short-circuit, OC-SC). The comparison of the curves scanning from OC-SC and then from SC-OC are presented in (b), showing that there is some hysteresis in the devices under these scan conditions but this effect is reduced for the treated sample. 90

A-16 (a-d) Device performance statistics for devices containing acetonitrile-based films stored in dry air in the dark (DAD), light-soaked in dry air (DAL), stored in humid air (45% relative humidity) in the dark (HAD) and light-soaked under humid air (45% relative humidity) (HAL). The light-soaking treatments were performed in the stated conditions by illuminating with a white-light LED array with an intensity similar to simulated sunlight for 20 minutes. Device measurements were taken under AM1.5 100mW/cm^2 simulated sunlight. 91

A-17 Stabilized maximum power output for devices containing acetonitrile-based films stored in (a) dry air in the dark (DAD), (b) light-soaked in dry air (DAL), (c) stored in humid air (45% relative humidity) in the dark (HAD) and (d) light-soaked under humid air (45% relative humidity). The light soaking treatments were performed in the stated conditions by illuminating the half-constructed devices with a white light LED array with an intensity similar to simulated sunlight for 20 minutes. The measurements were taken by holding at the maximum power point voltage and measuring current under AM1.5 100mW/cm^2 simulated sunlight. 92

A-18 (a) Light and dark J-V curves of champion devices for the devices containing acetonitrile-based films stored in dry air in the dark (DAD) and light-soaked in humid air (45% relative humidity) for 20 minutes with a white light LED array with an intensity similar to simulated sunlight (HAL). The measurements were taken fresh after the treatments and then after storage in a nitrogen-filled glove box for 3 weeks and 8 weeks. Device measurements were taken under AM1.5 100mW/cm^2 simulated sunlight. (b) External quantum efficiency (EQE) measurements on the devices stored for 8 weeks showing the integrated currents match those obtained from the current-voltage curves. 93

A-19 Light and dark J-V curves of champion devices for the devices containing acetate/HPA-based films stored in dry nitrogen (DND), dry air (DAD), humid air (45% relative humidity, HAD), and light-soaked under dry nitrogen (DNL), dry air (DAL) and humid air (HAL) for 20 minutes with a white light LED array with an intensity similar to simulated sunlight. Device measurements were taken under AM1.5 100mW/cm^2 simulated sunlight. 94

A-20 L(a-d) Device performance statistics for devices containing acetate-based films stored in dry nitrogen in the dark (N2D), light-soaked in dry nitrogen (N2L), dry air in the dark (DAD), light-soaked in dry air (DAL), stored in humid air (45% relative humidity) in the dark (HAD) and light-soaked under humid air (45% relative humidity) (HAL). The light soaking treatments were performed in the stated conditions by illuminating with a white light LED array with an intensity similar to simulated sunlight for 20 minutes. Device measurements were taken under AM1.5 100mW/cm^2 simulated sunlight. 95

A-21 Stabilized maximum power output for devices containing acetate/HPA-based films stored in (a) dry nitrogen in the dark (DND), (b) light-soaked in dry nitrogen (DNL), (c) dry air in the dark (DAD), (d) light-soaked in dry air (DAL), (e) stored in humid air (45% relative humidity) in the dark (HAD) and (f) light-soaked under humid air (45% relative humidity). The light soaking treatments were performed in the stated conditions by illuminating the half-constructed devices with a white light LED array with an intensity similar to simulated sunlight for 20 minutes. These measurements were taken by holding the full devices at the maximum power point voltage and measuring current under AM1.5 100mW/cm^2 simulated sunlight. 96

A-22 Electronic structure of $MAPbI_3$ (001) surface calculated by density functional theory. (a) band structure and D.O.S. for (001) surface containing an iodine vacancy occupied by a photogenerated electron showing shallow trap states below the conduction band. (b) band structure and D.O.S. for (001) surface containing an iodine vacancy occupied by a photogenerated electron into which an O_2 molecule is chemisorbed and reduced to form a superoxide species O_2^-. The sub gap shallow trap states indicated in (a) are now significantly reduced in density. 97

A-23 (a) PL measurements over time under illumination with a 532-nm laser at an excitation intensity equivalent to ∼2 sun (∼150 mW/cm^2) in dry air (blue) and humidified air (red). (b) X-Ray Photoemission Spectroscopy (XPS) measurements of the (b) I3d, (b) O1s, (d) N1s, (e) C1s, (f) Pb4f signatures in the regions of the sample light-soaked (light) and regions of the same films without light-soaking (dark). The atomic percent of oxygen species is labelled for each treatment. We find an increase in the O content after light-soaking in dry air, a substantial further increase in O when bringing into humid air, and a further increase again after light-soaking in humid air for 1000 seconds. We note that these O1s peaks are broad and likely consist of a range of species including, among others, superoxides and hydroxides. We do not observe dramatic changes in the other species, nor in the peak positions of each species. 98

A-24 Atomic force microscopy (AFM) images of the films for (a) a film stored in dry air without any light and (b) a region illuminated in humid air for 10 minutes with a 532-nm laser at an excitation intensity equivalent to ∼2 sun (∼150 mW/cm^2). The root-mean-square (RMS) variations of the surface over larger scan areas excluding pin-holes is 40.2 ± 4.0 nm (dry air) and 44.5 ± 4.5 nm (humid air + light). This represents a negligible change in roughness though potentially a very slight texturing after exposure to humidity and light. We note that this increase could not explain the increased external PLQE measurements we observe. 99

A-25 (a) PL measurements over time under illumination with a 532-nm laser at an excitation intensity equivalent to ∼2 sun (∼150 mW/cm^2) in dry air. (b-c) In-plane grazing incidence X-Ray Diffraction (IP-GIXD) for the (b) light-soaked region of a and (c) another region of the same sample without light-soaking (dark). (d-f) The same series but with humid air conditions. We do not find any significant changes after treatment in atmosphere or light for the short soaking periods in which we see the PL enhancements, suggesting we are not substantially perturbing the surface crystallinity or creating crystalline surface material. Significantly, no PbI2 is detected (expected ∼ 12.5°). 100

B-1 PL decays from the same bright and dark grains shown in Figure 3-1a, before and after light soaking in dry nitrogen. Samples were photoexcited with a 405 nm laser with a repetition rate of 0.5 MHz and a fluence of ∼1 μJ/cm^2/pulse (∼500 mW/cm^2), and this same laser was used for local light-soaking (total photon dose of ∼150 J/cm^2). 108

B-2 Compressed air storage over time in the dark. Confocal PL map of $MAPbI_3$ films prepared in a nitrogen glove box and maps acquired (a) in dry nitrogen, and in dry air after (b) 1 hour, (c) 24 hours and (d) 48 hours in dry compressed air. (e) A film stored for 48 hours in dry air but then measured in dry nitrogen after 1 hour storage in dry nitrogen, suggesting the oxygen pre-soaking (loading) effects can be removed. The map intensities are given relative to the maximum value in (a), which is normalised to 1. Samples were photoexcited with a 405 nm laser with a repetition rate of 0.5 MHz and a fluence of ∼1 $\mu J/cm^2$/pulse (∼500 mW/cm^2). (f) Total summed intensity of each map relative to the summed intensity of (a), which is normalised to 1. The blue symbol corresponds to the map in (e). 109

B-3 PL from a $MAPbI_3$ film measured *in-vacuo* (pressure $< 10^{-4}$ mbar) under continuous illumination with a 532-nm laser with excitation density similar to solar illumination conditions (∼2 sun, 150 mW/cm^2). . 110

B-4 (a) Confocal PL map of a $MAPbI_3$ perovskite film in dry air normalised to the maximum intensity. (b) Monitoring the emission intensity (count rate) from various bright and dark grains denoted in (a) over time under illumination in dry air. The PL intensity for each trace over time is given relative to the starting value for the highest initial intensity (blue grain), which is normalised to 1. These correspond to the same grains as shown in Figure 3-3a and b but before the exposure to humidity (cf. Figure 3-2). Samples were photoexcited with a 405 nm laser with a repetition rate of 0.5 MHz and a fluence of ∼1 $\mu J/cm^2$/pulse (∼500 mW/cm^2), and this same laser was used for local light-soaking (total photon dose of ∼150 J/cm^2). 113

B-5 (a) Confocal PL map of a $MAPbI_3$ perovskite film in dry air normalised to the maximum intensity. (b) Monitoring the emission intensity (count rate) from the same grain while light-soaking in dry air (cyan), humid air (blue) and after returning the sample to dry air (purple). This grain is unstable while light-soaking in humid air but retains its emission stability after returning to dry air. The emission intensities were normalised to the same initial value as the dry air measurement in Fig. 3-3c. Samples were photoexcited with a 405 nm laser with a repetition rate of 0.5 MHz and a fluence of $\sim$1 $\mu J/cm^2$/pulse ($\sim$500 mW/cm^2), and this same laser was used for local light-soaking (total photon dose of $\sim$150 J/cm^2). 114

B-6 Electronic structures and density of states (DOS) for the (110) surface of $MAPbI_3$ in the absence of any molecules. Columns 1, 2 and 3 correspond to the vacancies being negatively, neutral, and positively charged, respectively. (a)-(c) (row 1) corresponds to surface sites above Pb^{2+} on the PbI_2-terminated surface and (d)-(f) (row 2) in an iodine vacancy on defect-rich PbI_2 surface terminations. In the band structures the Fermi level is indicated by a red line. 115

B-7 Electronic structures and density of states (DOS) for the (110) surface of $MAPbI_3$ with adsorption of N_2. Columns 1, 2 and 3 correspond to the vacancies being negatively, neutral, and positively charged, respectively. (a)-(c) (row 1) corresponds to surface sites above Pb^{2+} on the PbI_2-terminated surface and (d)-(f) (row 2) in an iodine vacancy on defect-rich PbI_2 surface terminations. In the band structures the Fermi level is indicated by a red line. 115

B-8 Electronic structures and density of states (DOS) for the (110) surface of $MAPbI_3$ with adsorption of H_2O. Columns 1, 2 and 3 correspond to the vacancies being negatively, neutral, and positively charged, respectively. (a)-(c) (row 1) corresponds to surface sites above Pb^{2+} on the PbI_2-terminated surface and (d)-(f) (row 2) in an iodine vacancy on defect-rich PbI_2 surface terminations. In the band structures the Fermi level is indicated by a red line. 116

B-9 Electronic structures and density of states (DOS) for the (110) surface of $MAPbI_3$ with adsorption of O_2. Columns 1, 2 and 3 correspond to the vacancies being negatively, neutral, and positively charged, respectively. (a)-(c) (row 1) corresponds to surface sites above Pb^{2+} on the PbI_2-terminated surface and (d)-(f) (row 2) in an iodine vacancy on defect-rich PbI_2 surface terminations. In the band structures the Fermi level is indicated by a red line. 117

B-10 (001) Surface atomic and electronic structures. Local atomic configuration in surface termination layer (top row) and band structure (bottom row) for the (001) surface of $MAPbI_3$ (cf. Figure 3-4 for (110) results). (a) Pristine uncharged surface, (b) negatively-charged iodine vacancy into which the following molecules are adsorbed; (c) N_2, (d) H_2O and (e) O_2. Key: purple - iodine, grey - lead, blue - nitrogen, red - oxygen, white - hydrogen. In the band structures the Fermi level is indicated by a red line. 117

B-11 Electronic structures and density of states (DOS) for the (001) surface of $MAPbI_3$ in the absence of any molecules. Columns 1, 2 and 3 correspond to the vacancies being negatively, neutral, and positively charged, respectively. (a)-(c) (row 1) corresponds to surface sites above Pb^{2+} on the PbI_2-terminated surface and (d)-(f) (row 2) in an iodine vacancy on defect-rich PbI_2 surface terminations. In the band structures the Fermi level is indicated by a red line. 118

B-12 Electronic structures and density of states (DOS) for the (001) surface of $MAPbI_3$ with adsorption of N_2. Columns 1, 2 and 3 correspond to the vacancies being negatively, neutral, and positively charged, respectively. (a)-(c) (row 1) corresponds to surface sites above Pb^{2+} on the PbI_2-terminated surface and (d)-(f) (row 2) in an iodine vacancy on defect-rich PbI_2 surface terminations. In the band structures the Fermi level is indicated by a red line. 119

B-13 Electronic structures and density of states (DOS) for the (001) surface of $MAPbI_3$ with adsorption of H_2O. Columns 1, 2 and 3 correspond to the vacancies being negatively, neutral, and positively charged, respectively. (a)-(c) (row 1) corresponds to surface sites above Pb^{2+} on the PbI_2-terminated surface and (d)-(f) (row 2) in an iodine vacancy on defect-rich PbI_2 surface terminations. In the band structures the Fermi level is indicated by a red line. 120

B-14 Electronic structures and density of states (DOS) for the (001) surface of $MAPbI_3$ with adsorption of O_2. Columns 1, 2 and 3 correspond to the vacancies being negatively, neutral, and positively charged, respectively. (a)-(c) (row 1) corresponds to surface sites above Pb^{2+} on the PbI_2-terminated surface and (d)-(f) (row 2) in an iodine vacancy on defect-rich PbI_2 surface terminations. In the band structures the Fermi level is indicated by a red line. 121

B-15 Effect of vacancy charge state on photobrightening. Effect of iodine vacancy charge state on the photobrightening effect in an oxygen atmosphere on the (001) surface. All three types of surface vacancy (a-c) possess trap states. The photobrightening effect increases in the order: (d) positively charged, (e) neutral and (f) negatively charged (where we judge the effect by the final DOS near the Fermi level). In dark conditions all three charge states are possible but the intrinsic vacancy concentration will be much lower due to photo-induced iodine vacancy creation in the illuminated case. 122

List of Tables

2.1 Summary of Parameters from TRMC Measurements and Fits for Thin Films of $MAPbI_3$ Untreated and Treated 43

3.1 Adsorption energies of N_2, H_2O, and O_2 molecules onto iodine vacancies on a PbI_2-terminated (110) surface of $MAPbI_3$, with the vacancy in three possible charge states due to photoexcitation. See Table B.1 for adsorption energies for binding to Pb^{2+} on the PbI_2-terminated surface and Table B.2 for the (001) configuration 67

A.1 Relevant parameters extracted from the fits to the data with the kinetic model for the untreated (Figure A-12a) and treated (Fig. 2-2b) films, and 1 week after treatment (Figure A-12b). 101

B.1 Adsorption energies of N_2, H_2O, and O_2 molecules on the (110) surface of $MAPbI_3$ in three possible charge states due to photoexcitation. Favourable surface sites are on the Pb^{2+} on the PbI_2-terminated surface and in an iodine vacancy on defect-rich PbI_2 surface terminations. 111

B.2 Adsorption energies of N_2, H_2O, and O_2 molecules on the (001) surface of $MAPbI_3$ in three possible charge states due to photoexcitation. Favourable surface sites are on the Pb^{2+} on the PbI_2-terminated surface and in an iodine vacancy on defect-rich PbI_2 surface terminations. 112

Chapter 1

Introduction

The human's population demand for energy has increased almost two-fold in the past 30 years [12] and shows no sign of slowing down. At the same time, climate change, largely due to human CO_2 emissions from fuel sources has threatened the way of life for future generations [50]. In order to meet the energy demand and mitigate climate change, renewable energy sources must become predominant in the future. Photovoltaic devices represent one of the key renewable energy sources since the sun is the largest source of energy available to humans. The International Energy agency estimates that the total global energy consumption by 2035 will be approximately 20 TW, which could be easily satisfied if we harnessed even a fraction of the 89,000 TW of power from the Sun incident on Earth [41].

Crystalline silicon dominates the current photovoltaic market as the main semiconductor used for absorbing solar energy, but its complex and high temperature production methods lead to high module costs and limit its competitiveness in the energy market [50, 55]. Therefore, research into new photovoltaic technologies which utilise less material and have higher absorption in the solar spectrum. Metal halide perovskites have emerged as a new material which could disrupt the crystalline silicon market, due to its high absorption coefficient, ability for low temperature solution processing, high tolerance to defects and compatibility with flexible substrates [79]. Furthermore, the power conversion efficiency (PCE) of perovskite photovoltaics has increased from 3% to over 23% in the span of 8 years, while crystalline silicon photo-

voltaic devices took 30 years to reach this mark[62].

Nevertheless, perovskite devices are still far from their potential. They suffer from non-radiative recombination which hinders them from reaching the thermodynamic efficiency limit of $\sim 30\%$ power conversion efficiency [49]. In addition, perovskite thin films exhibit heterogeneous radiative efficiencies from crystal grain to crystal grain in the microscale, indicating that certain grains present more non-radiative recombination possibly due to increased trap densities [19]. In this thesis, we explore through confocal microscopy and supplemental techniques how a specific combination of air, moisture and light can lead to the elimination of most non-radiative recombination pathways and radiative heterogeneity. Also, we investigate how other gases such as nitrogen, oxygen or lack thereof impact the radiative properties of crystal grains in the microscale.

1.1 Confocal Microscopy

Confocal microscopy is a well-known imaging technique for fluorescent samples that offers high-resolution and contrast, reaching close to the limits of resolution due to diffraction. Furthermore, since these microscopes collect fluorescence from small regions, it allows for two or three-dimensional micron-scale maps of fluorescent samples by movement of the sample stage or parts of the optical system[88]. As such, it has been extensively used in biological applications to image dynamic processes through the use of fluorophores[71].

Nevertheless, we can use confocal microscopy for more than biological applications. In this case, we can study the photoluminescence (PL) micro-structure of semiconductor thin films that are used in optoelectronic applications, specifically methylammonium lead halide perovskites semiconductors. PL is a significant figure of merit to analyze since significant variations in PL intensities and lifetimes between grains in the micro-scale are indicative of a significant presence of trap-states that act as non-radiative recombination sites, even for high-performing films in optoelectronic devices[19]. Non-radiative recombination limits their performance in photovoltaic

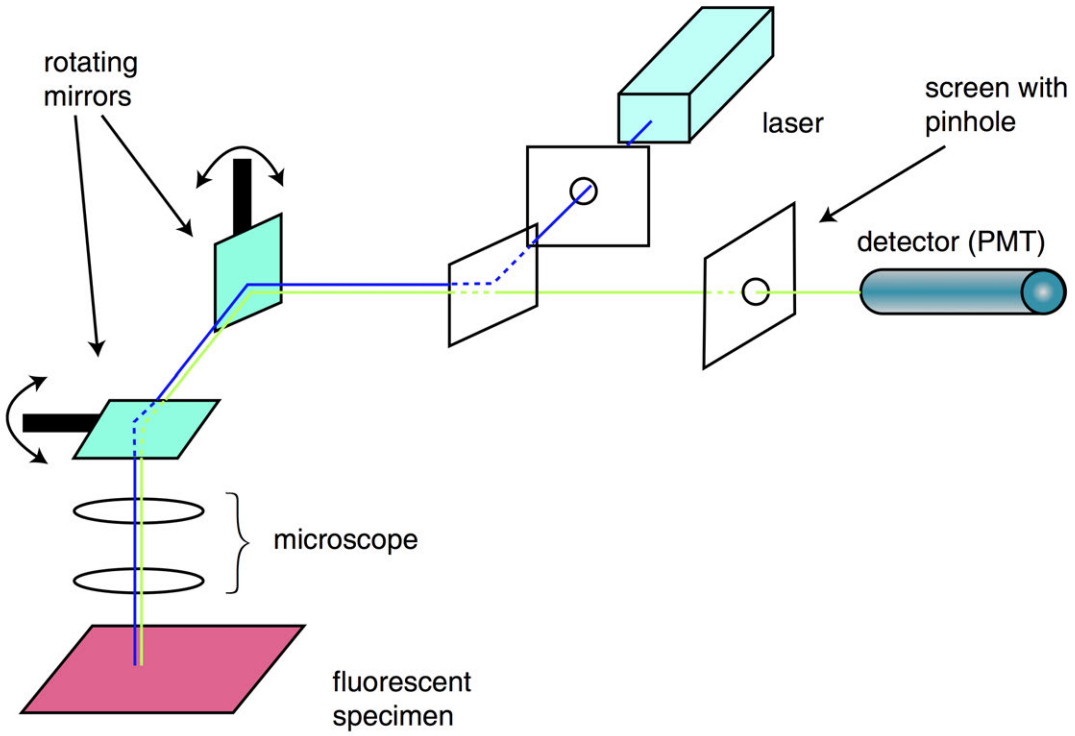

Figure 1-1: Standard confocal microscope setup as depicted by Semwogerere et al.[71].

and light emitting devices, since thermodynamic limits of efficiency are only achieved when all recombination is radiative [49]. As such, we can study the effect of different surface passivation methods on perovskite thin films in the micro-scale, in our case moisture and oxygen, in order to determine whether these techniques can lead to reaching thermodynamic limits of performance.

A standard confocal microscope setup is shown on Figure 1-1[71]. In these microscopes, both the detector and the illumination source are placed at the conjugate plane (focal plane) of the microscope with completely equivalent optical paths after the beam splitter. In the setup shown on Figure 1-1, a pinhole is placed in front of the illumination source in order to obtain an Airy disc diffraction pattern to obtain a uniform illumination profile regardless of the alignment of the illumination source. In this case, even if the illumination source becomes misaligned, the illumination profile will remain the same and only the intensity of the illumination will change. In our setup, detailed in the experimental methods section, we utilize a coherent laser beam with a width of about 3mm which is then further focused down to ∼600nm for the

first radial null of the Airy disc pattern. As such, we do not utilize a pinhole aperture to create a uniform illumination profile. Instead, the Airy disc pattern arises from the fact that the lenses in the system have a finite width, which is equivalent to passing a coherent light source through a circular aperture followed by an ideal lens[88]. The purpose of the second pinhole aperture in front of the photodetector is to limit the collected fluorescence to only that coming from between the first maxima and minima of the Airy disc pattern produced by the lenses and thus limit any stray fluorescence. In our setup, we utilize an avalanche photodiode with a $50\mu m$ active area, which doubles as the PL detector and a square pinhole since it only collects light incident upon its active area.

The improved resolution of the confocal microscope compared to other optical microscopes comes from the use of the same optical lens system to both illuminate and collect the fluorescence from the sample. The regular Rayleigh criterion states that, in order to resolve two distinct images without considering aberration, the first maxima of one diffraction pattern must coincide with the first minima of the other [88]. Assuming and Airy disc diffraction pattern, the first minima and thus the minimum resolvable length happens at $r = \frac{0.61\lambda}{\text{NA}}$, where $\text{NA} = n\sin(\theta)$ is the numerical aperture and is a dimensionless measure of the angular behavior of the light cone, θ is the half angle of the light cone converging to an illuminated spot and n is the refractive index of the optical system [88]. As such, the higher the NA, the better resolution we can get from an optical system. Nevertheless, this exact resolution criterion does not apply to confocal microscopy. Let $p(\rho, \xi)$ be the three-dimensional intensity distribution for an Airy disc, where $\rho = \frac{2\pi \mathbf{r}}{\lambda}\text{NA}$ and $\xi = \frac{2\pi}{n\lambda}\text{NA}^2 z$ describe the three dimensional position, such that along the imaging plane $p(\rho, \xi = 0) = \frac{2J_1^2(\rho)}{\rho^2}$ where J_1 is the Bessel function of the first kind [88]. Since we are illuminating with an Airy disc pattern, the emitted fluorescence from this illuminated region will have the same pattern and after going through the same optics again then the fluorescence intensity distribution on the photodetector will appear like[88]:

$$p_{conf} = p(\rho, \xi) \times p(\rho, \xi) \tag{1.1}$$

The intensity distribution for the regular Airy disc is shown alongside the intensity distribution for p_{conf} on Figure 1-2. As we can see, the first null for p_{conf} does not occur at the same point as for the regular Airy disc intensity pattern and instead occurs at $r_{conf} = \frac{0.44\lambda}{\text{NA}}$, which means that we can resolve smaller objects compared to the regular Rayleigh criterion[88]. Furthermore, p_{conf} offers much better contrast since much of its energy lies within the central peak, therefore dim objects that might appear in our intensity distribution contribute less to background light [88]. In our

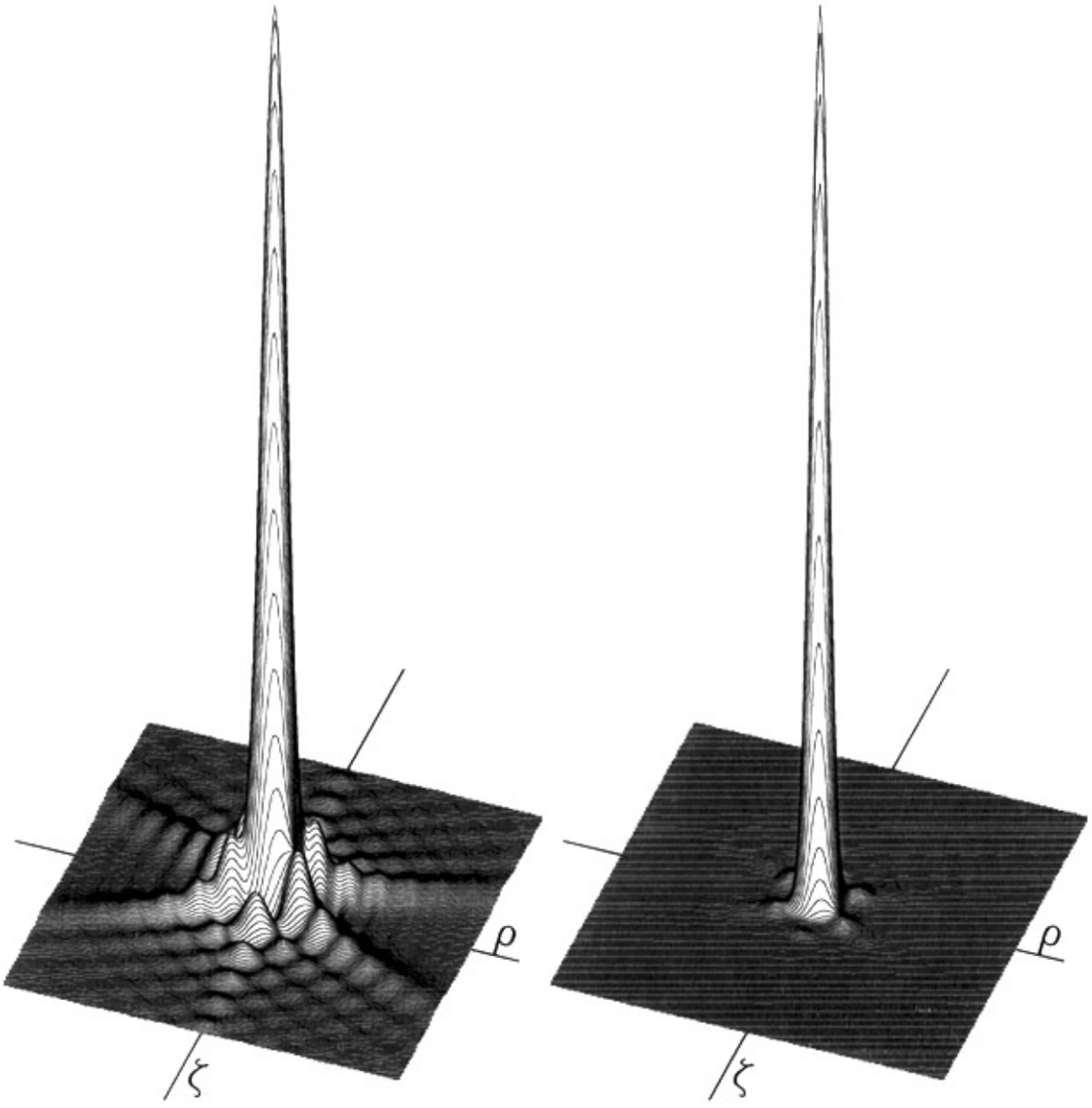

Figure 1-2: Left: Airy Disc intensity distribution. Right: Intensity distribution p_{conf} for a typical confocal setup. Plots from Robert H. Webb[88].

system, we obtain even better resolution through the use of an oil lens, which means that we place the sample on a lens covered by paraffin oil with a high refractive index ($n \sim 1.5$) in order to increase the NA of the optical system. We also filter out any scattered laser light by employing a dichroic filter which only reflects wavelengths of interest towards the detector. This is achieved by utilising a laser that has a spectrum which does not overlap with the emission spectrum from the sample.

Finally, we can use this system to create fluorescence maps by acquiring the signal at a single point and then sequentially scanning through the area of interest of the sample to form an image. Since our system employs an inverted microscope with fixed optical components apart from the microscope objective, we perform sequential scanning by moving the sample itself. High movement accuracy and repeatability are desired, thus we utilize an xyz piezo stage (Physik Instrumente, P-733.3CL) which offers nanometer resolution and repeatability.

1.2 Time-correlated single photon counting

Time-correlated single photon counting (TCSPC) is a method through which we can measure the amount of time that it takes for a photo-excited carrier to radiatively recombine, thus emitting a photon. This can be done by measuring the time interval between a laser pulse and the arrival of a photon on the photodetector, as depicted on figure 1-3[86]. In this way, we can build a histogram of arrival times of photons over time in order to form what is known as a PL lifetime decay. However, photons will go uncounted in the histogram if they arrive before the TCSPC system has had time to re-initialize to detect a new photon after a photon count event has happened, known as the dead time. Typical dead times for these systems are in the tens of nanoseconds [86]. As such, we need to adjust the fluence of the laser to be low enough such that the probability for the sample to emit a single photon between laser pulses is low. This is normally done experimentally by adjusting the photon count rate per second to be below 10% of the laser repetition rate. If not, skewed photon statistics will be collected, where early arrival times will have an artificially high count of photons, an

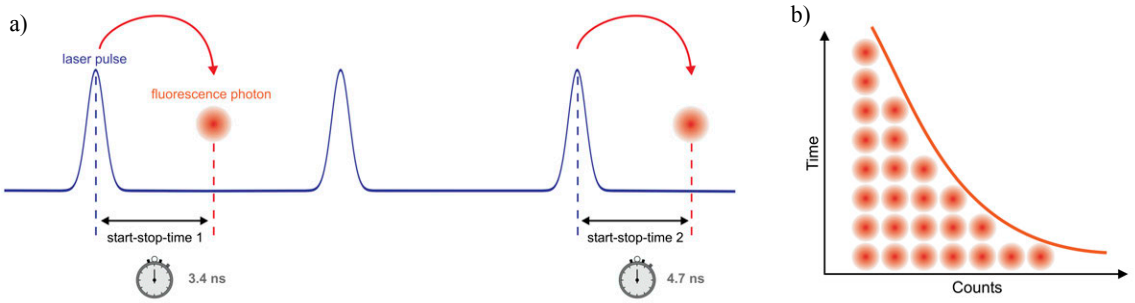

Figure 1-3: a) Scheme for measuring photon arrival times. b) Histogram built from the photon arrival times [86].

effect which is known as pile-up. The setup for a TCSPC system is shown on Figure 1-4[86].

TCSPC is a useful measurement to determine radiative and non-radiative lifetimes for most semiconductors. These lifetimes provide us with an indication of the quality of the material as well as which process (radiative or non-radiative) dominates in the material. By knowing the initial carrier density in the material, which can be determined from the laser flux and the absorptivity of the material, we can fit a set of rate equations to extract radiative and non-radiative rates as well as trap densities

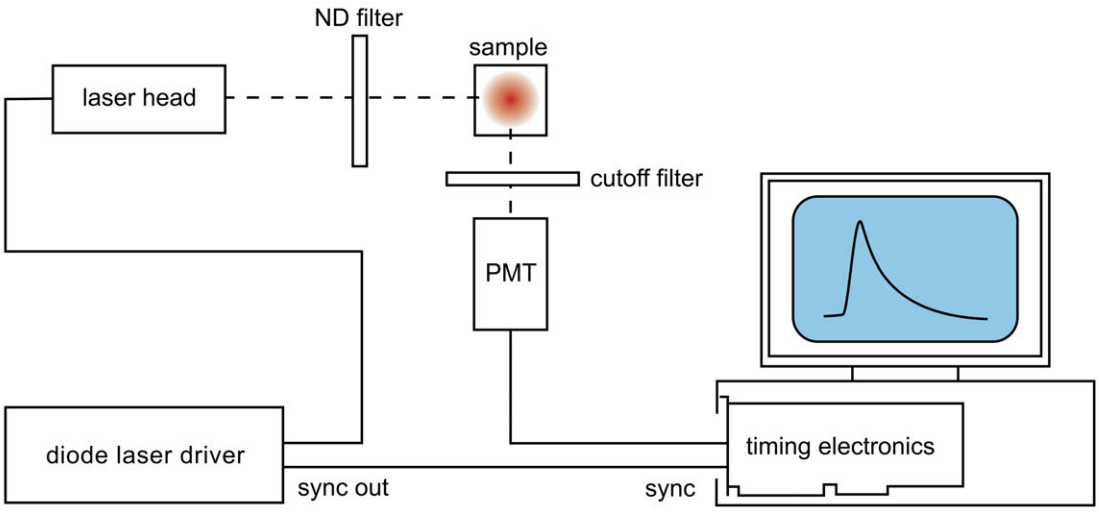

Figure 1-4: Typical TCSPC setup as detailed by Michael Wahl. An ND filter is used to reduce the intensity of the laser and a cutoff filter (normally a dichroic filter) to remove any scattered light from the laser and only collect the wavelengths of interest [86].

in the material. This is further elaborated upon in Appendix A.

1.3 Thesis Outline

This thesis is structured in two main chapters that deal with different atmospheric combinations and their effects on perovskite thin films. Chapter 2 explores the use of air, moisture and light in order to improve the radiative and conduction properties of lead halide perovskites. We show the experimental findings of the improvements and then propose a model that explains the mechanism of photobrightening in the material. Chapter 3 explores the exposure of perovskite thin films to different atmospheric conditions such as nitrogen, oxygen with and without moisture as well as vacuum conditions. We show how these conditions effect the photoluminescent properties of perovskite grains in the microscale and explain the mechanisms through the aid of density functional theory. Appendices A and B provide supplemental information to chapters 2 and 3, respectively.

Chapter 2

Metal Halide Perovskite Polycrystalline Films Exhibiting Properties of Single Crystals

2.1 Introduction

Metal halide perovskites are an exciting class of materials that possess many of the attributes desirable for optoelectronic applications, with certified power-conversion efficiencies of perovskite based photovoltaics reaching 22% [70, 95]. Despite impressive device performance, perovskites are still far from their full potential. For instance, the photoluminescence quantum efficiency (PLQE) of thin films used in highly efficient devices is still far from unity [75]; typical external PLQE values are 1% at excitation intensities equivalent to solar illumination, which corresponds to internal PLQE values of 10% after accounting for losses from photon recycling and poor light out-coupling [68]. These low values are consistent with a sizable density of sub-gap trap states that act as non-radiative recombination centers [76, 46, 89]. In order for a solar cell or light-emitting device to reach its theoretical performance limits, luminescence should

Chapter 2 is adapted with permission from Brenes et al., Metal Halide Perovskite Polycrystalline Films Exhibiting Properties of Single Crystals, Joule (2017), http://dx.doi.org/10.1016/j.joule.2017.08.006

be maximized with all non-radiative recombination eliminated [49].

Perovskite single crystals have been reported to exhibit superior properties to polycrystalline thin films, with 2–4 orders of magnitude lower trap densities [73, 13]. This leads to long charge-carrier lifetimes and diffusion lengths of tens of microseconds and micrometers, respectively[59, 7], and surface recombination velocities as low as 3 cm/s [29]. However, controlled growth of single crystals into devices does not lend itself to the many advantages offered by solution-processing polycrystalline thin films such as roll-to-roll depositions. Recently, the use of surface treatments to passivate deep trap states in polycrystalline films has been reported, yielding reductions in trap density by an order of magnitude [60, 21]. However, it is unclear what impact these surface treatments might have on other properties of the film such as the transport properties, interfacial energies, and grain stability. The illumination of perovskite materials has also been shown to achieve reductions in trap density [22], and these improvements depend on the light dose [22] and can be boosted further in the presence of oxygen [82]. However, these reports have shown only limited local luminescence enhancements with the effects being reversible on a timescale of $\sim$10 hr and not leading to spatially uniform emission over large areas of a high-quality film. In this work, we use a combination of light and atmospheric post-treatments on methylammonium lead iodide ($MAPbI_3$) perovskite thin films that lead to permanent and exceptionally large enhancements, with the resulting optoelectronic properties approaching those of single crystals.

2.2 Results

2.2.1 Macro- and Micro-photoluminescence Enchancements

Thin films (250 nm thickness) of $MAPbI_3$ perovskite were solution processed on glass (see Appendix A) [100]. In Figures 2-1a-c, we show the internal PLQE values (η) of films in different atmospheric conditions while under continuous-wave (CW) illumination with excitation densities close to solar illumination conditions. The internal

values are calculated from the measured external PLQE values (η_{meas}, Figure A-2) following the methods of Richter et al. [68]. (see Appendix A). The film illuminated in dry nitrogen shows a small rise in emission, and the internal PLQE reaches a value of $\eta = 12\%$ (Figure 2-1a). When the film is instead illuminated in dry air, the photoluminescence (PL) rises substantially and the internal PLQE approaches $\eta = 48\%$ and continues to slowly rise (Figure 2-1b). When the film is light soaked in humidified air (45% relative humidity), the internal PLQE plateaus at $\eta = 89\%$ (Figure 2-1c). This is approaching PLQE values in which almost all of the non-radiative decay processes are eliminated, despite starting with internal PLQE values of $\eta \approx 1\%$. We find that the enhancements are retained with only a small drop in PLQE to $\eta = 84\%$ when returning the film to dry air (Figure A-2), with the small drop appearing to correlate with the desorption of water molecules from the film surfaces upon drying [54]. We also find corresponding enhancements in carrier lifetime from time-resolved PL measurements (Figure 2-1c inset), which show radiative bimolecular kinetics (Figure A-3).

In Figures 2-1d-h, we present a progression of confocal PL maps corresponding to the treatment of light soaking under humidified air (see Figures A3 and A4 for other conditions). Under dry air conditions (Figure 2-1d), we clearly see a grain-to-grain heterogeneity in emission intensity. There is an increase in the PL baseline intensity when moving to humidified air (Figure 2-1e), which is consistent with earlier reports of the beneficial effects of humidity on film fabrication [27, 5]. However, there is then a substantial increase in intensity of all grains after light soaking for 10 min under excitation with a 532-nm laser at an excitation equivalent to 10 sun (Figure 2-1f). When comparing the film after the treatment (Figure 2-1g) with that before the treatment (Figure 2-1d), we find that there has been a net increase in the emission intensity, PL lifetime, and spatial homogeneity (Figure A-6). Furthermore, there is a near-instant rise to stabilized emission output for the treated film in dry air (Figure 2-1g inset) compared with the slow rises in the corresponding untreated film under the same conditions (Figure 2-1g inset). In recent work, a strong correlation between the slow transient PL rises and photo-induced ion migration was found [22].

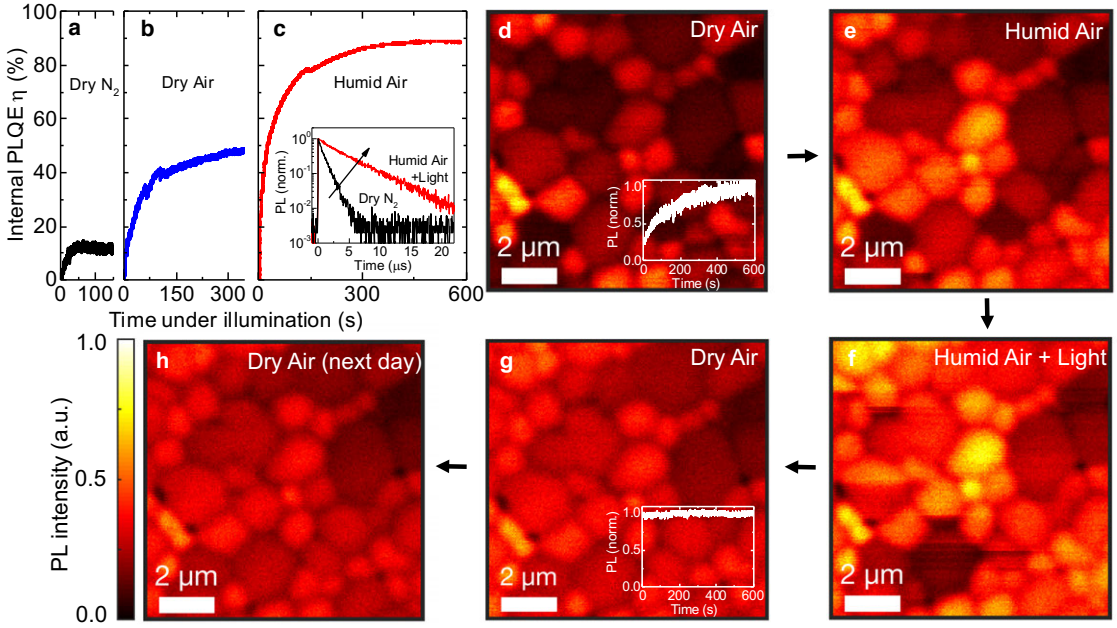

Figure 2-1: *Macro- and Micro-photoluminescence Enhancements of Thin Films under Solar Illumination Conditions* (a–c) Internal PLQE η measurements over time under illumination with a CW 532-nm laser at an excitation intensity equivalent to 2 sun (150 mW/cm^2) in dry N2 (a), dry air (b), and humid air (c). Inset: Time-resolved PL decays of the films after the stated treatment with pulsed excitation at 405 nm (excitation density of 5.4×10^{15}cm^{-3}). (d–h) In situ confocal PL maps with 405-nm excitation measured in (d) dry air, (e) humidified air, (g) after light soaking for 10 min under excitation with a 532-nm laser equivalent to 10 sun under humid air, (g) after returning to dry air, and (h) measured the next day with storage in dry air. Insets to (d) and (g): emission stability of the films in dry air before and after the treatment, respectively, with excitation at 532-nm at intensity equivalent to 10 sun.

Therefore, the elimination of the transient PL rises under illumination suggests that photo-induced ion migration has been inhibited after the treatment [75]. There is a negligible decrease in the enhancements when measured the next day (Figure 2-1h) and even 3 weeks after treatment when the film is encapsulated with a layer of the polymer poly(methylmethacrylate) (PMMA) (Figure A-7). We stress that the combination of light, air, and moisture is essential to exploit all of these beneficial effects (Figures A7 and A8), but longer exposure times to this combination lead to degradation (Figure A-10) [45, 3].

2.2.2 Enhancements in Film Photoconductance and Diffusion Length

In order to assess the impact of the treatments on charge transport, we performed time-resolved microwave conductivity (TRMC) measurements. This technique monitors the photoconductance ΔG on pulsed illumination, giving a direct measure of the charge-carrier yield, lifetimes, and mobilities [40, 66]. Figure 2-2a shows ΔG of the films after storage in dry air (untreated, black curve) and after light soaking for 30 min in humid air (40% relative humidity) under a white light LED source generating a similar photon flux to AM1.5 sunlight (treated, red) (see Figure A-11 for other conditions). Importantly, we see a profound increase in the lifetime of the charge carriers after the treatment, which is retained even after storage of the bare film in a nitrogen glove box for a week (redried, blue curve).

In Figure 2-2b, we show TRMC decays of the treated films with initial photo-excited charge densities varying over three orders of magnitude (see Figure A-12 for other treatments). The resulting half lifetimes of the excitation-dependent decays $\tau_{1/2}$ (time taken to decay to half of the initial value) for different excitation densities are shown in the inset of Figure 2-2a. Most importantly, we see a substantial increase in the lifetimes of the charge carriers at each excitation density in the treated film compared with the untreated film, with the lifetime at the lowest fluences increasing from 6.2 ms to 32.3 ms after treatment. We note that the lifetimes (1–6 ms) and

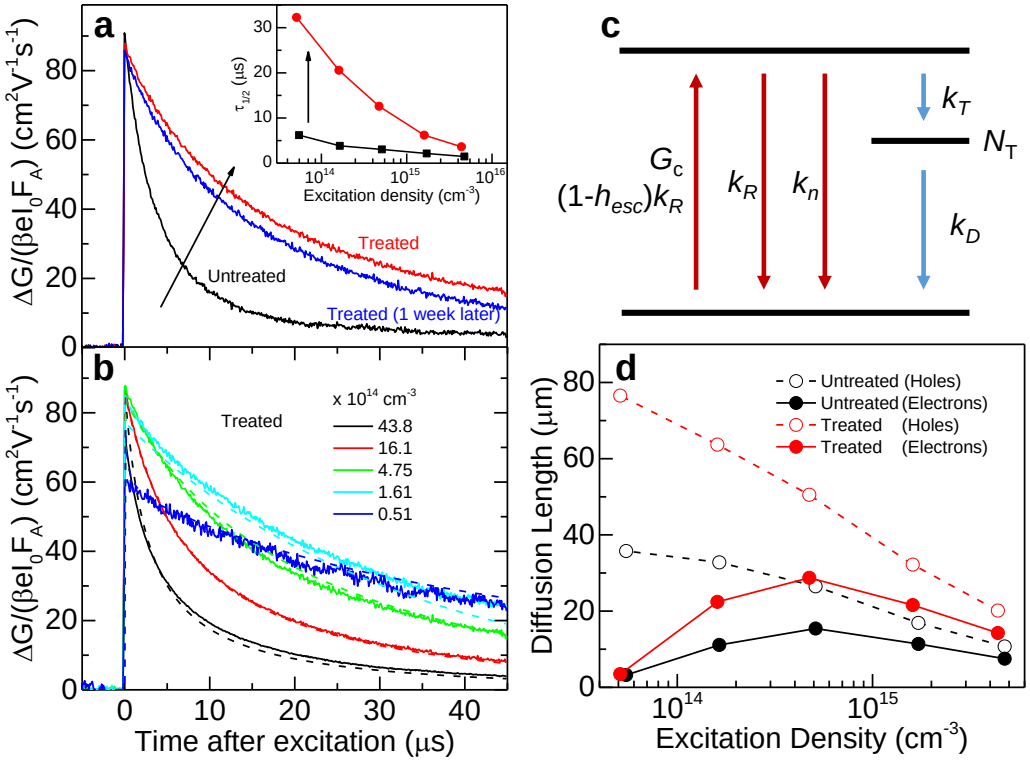

Figure 2-2: *Enhancements in Film Photoconductance Determined from Time-Resolved Microwave Conductivity Measurements* (a) Photoconductance measurements for a $MAPbI_3$ film after storage in dry air and after being subjected to light soaking for 30 min in humid air (40% humidity) under a constant photon flux similar to solar conditions. The TRMC trace taken after storing the same sample in a nitrogen glove box for a week after the treatment is also shown. The TRMC decays were recorded by photo-exciting the samples in dry N_2 with pulsed illumination at 500 nm and an excitation density of $5 \times 10^{14} \mathrm{cm}^{-3}$. (b) TRMC decays (normalized to absorbed flux) of the treated samples with the initial charge excitation density as indicated. (c) Dashed lines are fits to the data using the trap model summarized in (c), where G_c is the generation rate and k_T and k_D are the trapping and trap recombination rates, respectively. (d) Diffusion lengths of the electrons and holes before and after the treatments.

Table 2.1: Summary of Parameters from TRMC Measurements and Fits for Thin Films of $MAPbI_3$ Untreated and Treated

Sample	$\mu_e + \mu_h$ ($cm^2V^{-1}s^{-1}$)	k_2^{eff} ($10^{-11}cm^3s^{-1}$)	$\eta(\%)$	k_2^{int} ($10^{-11}cm^3s^{-1}$)
Untreated	87	26.0	1	26.2
Treated	87	7.60	84	28.5

mobilities ($\mu \approx$70–90$cm^2V^{-1}s^{-1}$) of carriers even in the untreated film are already as large as in the highest-quality perovskite thin films reported [21, 42].

We can describe the observed behavior based on a kinetic model that incorporates the presence of a density N_t of deep electron trap states and is summarized in Figure 2-2c (see Appendix A for details) [76, 39]. If the photo-excitation generation density exceeds the deep trap density N_t, the charge-carrier decay kinetics are dominated by bimolecular recombination of electrons and holes, but at low fluence when many electrons are immobilized into these trap states, the recombination appears pseudo-monomolecular [76]. Richter et al. [68] recently proposed that the bimolecular recombination constant is actually comprised of a radiative (k_R) and non-radiative (k_n) component. This leads to an effective (external) bimolecular recombination rate constant that can be extracted from fits to the TRMC data given by an expression encompassing the effects of photon recycling and light out-coupling:

$$k_2^{eff} = \eta_{esc} k_R + k_n \tag{2.1}$$

where $\eta_{esc} = 12.7\%$ is the escape probability of a photon from a bare perovskite film on glass for the film thickness in this work [68].

We fit this model to the set of excitation-dependent decays and show the fits for the treated films as dashed lines in Figure 2-2b (see Figure A-12 for other treatments, Tables 2.1 and A1 for parameters, and Appendix A for discussion on sensitivity of the analysis). We find a remarkably low deep trap density for these samples, which only changes negligibly for the sample light soaked in humid air ($N_t = 6.0 \times 10^{13} cm^{-3}$ reducing to $5.5 \times 10^{13} cm^{-3}$), suggesting that the treatments are primarily affecting the

radiative and non-radiative components of the bimolecular recombination constant. Furthermore, the mobility values for the electrons and holes remain similar upon the treatment, indicating that the bulk properties have not changed significantly.

We find that the k_2^{eff} decreases from $26.0 \times 10^{-11}\text{cm}^3\text{s}^{-1}$ when untreated to $7.60 \times 10^{11}\text{cm}^3\text{s}^{-1}$ with the treatment. With the measured internal PLQE η values, we extract the internal bimolecular rates k_2^{int}, which we find to be almost unchanged from the untreated ($26.2 \times 10^{-11}\text{cm}^3\text{s}^{-1}$) to treated ($28.5 \times 10^{11}\text{cm}^3\text{s}^{-1}$) samples (see Appendix A for details). This suggests that the rate of recombination collisions between electrons and holes is unchanged on treatment. However, the treatments increase the fraction of these collisions that are radiative compared with the fractions that are non-radiative. This means that each carrier is more likely to be re-generated due to a photon recycling event [63], which is only possible with radiative recombination, prolonging the effective lifetime of the carriers. This leads to the conclusion that the increase in carrier lifetimes with treatment is primarily due to an increased fraction of radiative recombination, in turn leading to enhanced recycling of carriers.

We use the kinetic model to extract the individual carrier lifetimes and use these to calculate the resulting diffusion lengths of each carrier using $L_D = \sqrt{k_B T \mu \tau_{1/2}/e}$, where k_B is the Boltzmann constant, T the temperature, e the electron charge, and μ the carrier mobility extracted from the photoconductance measurements (Figures 2-2d and A12) [7]. We find remarkable hole diffusion lengths of 76.5 μm in the treated film at low excitation fluences at which the electron traps are still not completely saturated, and therefore the majority of the electrons are immobilized in trap states, while we find electron diffusion lengths reaching 28.7 μm at intermediate charge densities in which all of these electron traps are filled. We note that these diffusion lengths are the average cumulative distance that charges diffuse, including recycling through reabsorption events (Figure A-14).

The exceptional diffusion lengths, carrier lifetimes, mobilities, and low deep trap densities show that these polycrystalline thin films possess properties only previously demonstrated in single crystals [7, 16]. In fact, the lifetime ($\tau_{1/2} = 32.3\mu$s) of the treated film already exceeds that seen in single crystals under similar conditions (15

μs), and the deep trap densities are comparably low [7]. The surface recombination velocity (SRV) in unpassivated perovskite polycrystalline films and single crystals has been reported to be 1,000 cm/s [96], which can be reduced to 3 cm/s for passivated single crystals [29]. We calculate SRV $\approx L/2\tau_{1/2} \approx 0.4cm/s$ for the holes at low charge densities in treated films in which $\tau_{1/2} = 32.3\mu$s and $L = 250$ nm is the film thickness (see Appendix A) [29, 92]. This is an order of magnitude lower than passivated perovskite single crystals and comparable with the lowest value ever reported for any semiconductor in <111> crystalline silicon (0.15 cm/s) [92, 10], which is truly remarkable when considering that these are solution-processed polycrystalline films.

2.2.3 Enhancements in Solar Cell Device Performance

To validate the treatments in devices, we constructed planar heterojunction perovskite solar cell devices in the configuration of FTO (fluorinated tin oxide) / SnO_2 / $CH_3NH_3PbI_3$ / 2,2',7,7'-tetrakis(N,N'-di-p-methoxyphenylamine)-9,9'-spirobifluorene (spiro-OMeTAD) / Au, where the perovskite was deposited using an acetonitrile-based solution-processing route [61]. We performed the treatments on the bare perovskite in half-constructed devices before depositing the hole transporter (spiro-OMeTAD) and Au electrodes for testing. We show in Figure 2-3a the current-voltage (J-V) curves and in Figure 2-3b the stabilized power output of champion devices incorporating the untreated films and the treated films that have been exposed to humid air with light soaking (see Figure A-15 for other treatments and Figure A-16 for device statistics). We see an increase in the short-circuit current from 22.6 to 23.4 mA/cm^2 and the open-circuit voltage from 1.04 to 1.13 V, both consistent with the reduction in non-radiative decay and subsequent increase in carrier diffusion length and lifetime after the treatments. This yields champion device efficiencies of 19.2% (treated) and 17.8% (untreated), with stabilized power output of 18.4% and 17.4%, respectively. Although hysteresis is still present (Figure A-15), we find that the extent of the hysteresis is reduced with the treatment and this finding is accompanied by a noticeable increase in the steady-state efficiency of the devices (Figure 2-3b). Importantly, the time to rise to stabilized power output is much faster in the

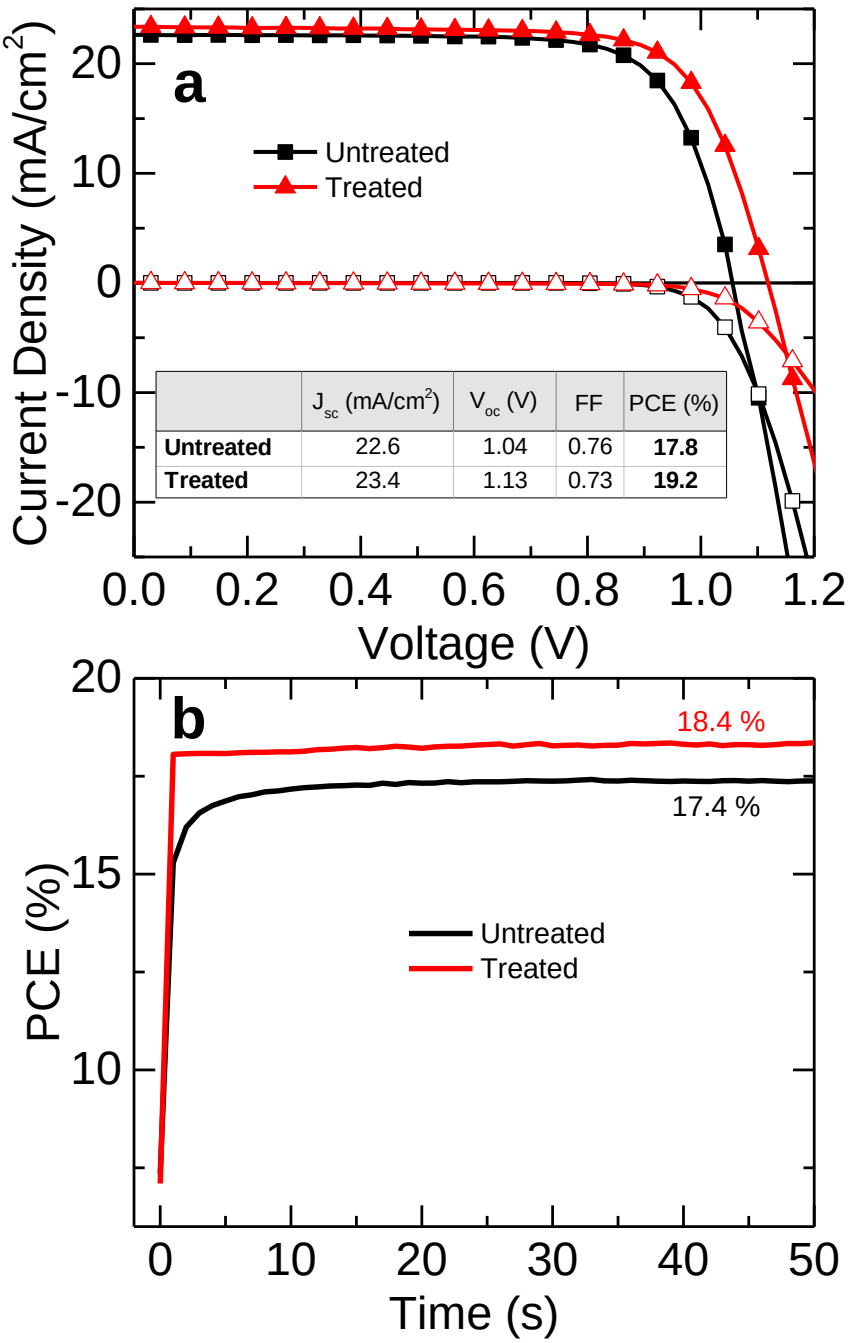

Figure 2-3: *Enhancements in Solar Cell Device Performances* (a) Light and dark J-V curves of champion devices for the devices containing untreated (stored in dry air) and treated (light soaked in humid air) films measured under AM1.5 100 mW/cm^2 simulated sunlight. (b) Stabilized power output of the devices presented in (a) measured by holding the devices at their maximum power point (as determined from J-V curves) for 50 s.

treated film, with near-instant rise to stable output compared with the slower 10–20 s rise in the untreated films with the same device structure (see Figure A-17 for other treatments). These findings are consistent with the PL output in the treated films instantly reaching their maximum value without a slow rise time (cf. Figure 2-1g, inset). They are also consistent with the assertion that ionic migration, the origin of the slow transient rises [26], is impeded in the devices with treated films. The device performance enhancements remain after 3 weeks of storage in a nitrogen glove box and still remain superior to the controls after 8 weeks of storage (Figure A-18). We also find enhancements when using the acetate-based method (Figures A18–A20), suggesting that the post-treatments are capable of improving perovskite films processed in different ways. We note that the optically implied open-circuit voltages [81] from an internal quantum efficiency of 89% should lead to voltage losses of only a few meV, indicating that there are still non-radiative losses introduced from the contacts [28], insufficient light out-coupling from the devices or partial removal of the treatment following deposition of the top layers. We also note that the light-soaking enhancements are not as evident when performed on the full device stack rather than the half stack, and we speculate that this is because the hole transporting layer prevents the crucial interaction of the atmospheric molecules with the perovskite surface.

2.2.4 Mechanism of Photobrightening

In order to explain the observations, we propose that there is a distribution of shallow surface states, and the carriers in the bands can easily transfer into and thermally out of these states (Figure 2-4a). We depict these as shallow electron states just below the conduction band, but these could equally be shallow hole states above the valence band. We propose that the radiative bimolecular recombination (k_R) is band-to-band recombination while the non-radiative bimolecular component (k_n) is electron-hole recombination mitigated through these shallow surface states (Figure 2-4a). If such states remained mostly unoccupied, this non-radiative recombination would be bimolecular because the rate would depend on the concentration of both electrons (and hence the density of trapped electrons) and holes. The treatments then

decrease the density of these shallow states, leading to a greater fraction of electron-hole collision events being radiative k_R than non-radiative k_n and hence significantly increasing the PLQE (Figure 2-4a). We note that we distinguish these shallow states from the deep trap states, which solely mitigate non-radiative recombination through irreversible electron trapping and which are of very low density in the samples studied here ($N_t \approx 10^{13}\text{cm}^{-3}$) and appear to be mostly unaffected by the treatments.

The nature of these shallow states that promote non-radiative recombination but do not affect charge mobility is unclear. Since the mobility and therefore bulk charge transport (including grain-to-grain transport) is mostly unaffected by the surface treatments, we propose that the shallow states primarily reside on the surfaces as opposed to the grain boundaries. However, we note that we cannot exclude the additional presence of deep traps and/or low densities of shallow traps on grain boundaries in the bulk. Here, we explore the case of a density of shallow defects associated with iodide vacancies [97], but we note that other explanations are also possible such as surface traps due to electron-phonon coupling [90] or surface structures with an indirect band gap [40]. Recently, we reported experimental and theoretical evidence that oxygen diffusion into $MAPbI_3$ films is accompanied by photo-induced formation of superoxide species (O_2^-) at iodide vacancies over the timescales relevant to the enhancements we report here [3]. Here, we use density functional theory calculations to show that, as a result of O_2 reduction to O_2^- at surface vacancies occupied by photogenerated electrons, the sub-gap states shift down into the valence band (Figure A-22), removing the shallow states. The passivating effect of oxygen is consistent with an increase in surface oxygen content after the treatments (Figure A-23).

2.3 Discussion

We summarize the proposed mechanism for the treatments in Figures 2-4b–d. First, an untreated $MAPbI_3$ sample containing surface states (Figure 2-4b) is exposed to light and oxygen. This reduces the density of surface states and leads to photobrightening (Figure 2-4c) through the formation of passivating superoxide species. This

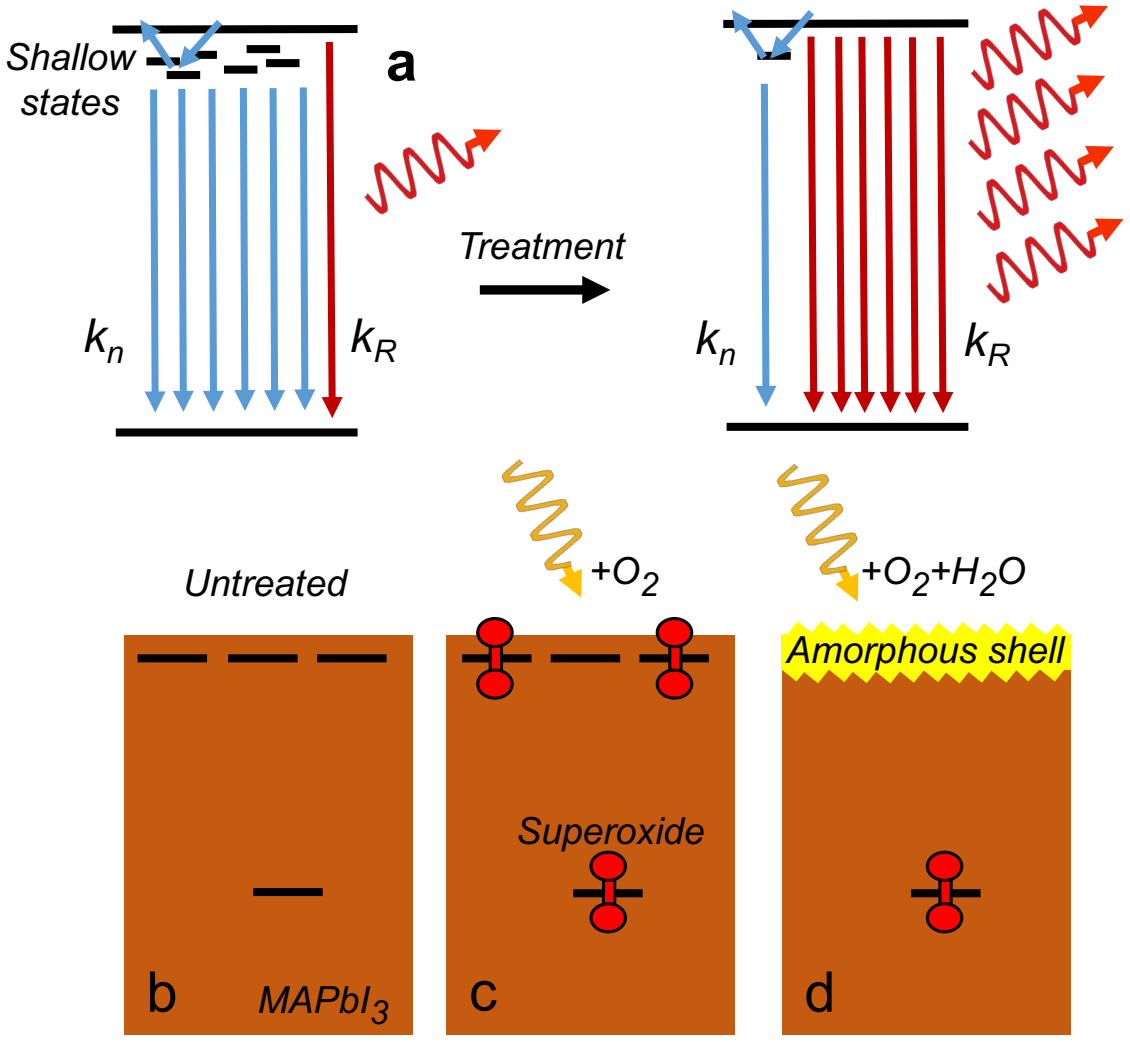

Figure 2-4: *Mechanism of Photobrightening* (a) Schematic showing non-radiative recombination (k_n) dominating owing to shallow surface states, which are removed in the treatment to lead to radiative-dominant (k_R) recombination. (b–d) Untreated $MAPbI_3$ films (b) containing non-radiative trap states that are passivated by exposure of $MAPbI_3$ to (c) light and oxygen and (d) light, oxygen, and water.

process is reversible on a timescale of hours if the sample is then kept in the dark. Second, when an untreated sample is briefly exposed to light, H_2O, and O_2 (Figure 2-4d), the density of shallow states decreases to an even greater extent due to complete removal of the states at the surface by forming a nanometer-thin amorphous shell of inert degradation products [38]; these shells could be indicated by a minor texturing of the surfaces after the treatment (Figure A-24) but no detectable changes in the crystalline properties of the surface (Figure A-25). This process is mostly irreversible; the shell of degraded material acts as a containing barrier through which the oxygen species only slowly de-gas from the film (an encapsulating impermeable polymer such as PMMA is even more effective). The treatments inhibit ion migration, since oxygen occupies iodide vacancy sites involved in the migration process, and the degraded shell introduces a partial barrier to ionic transport in the intergrain regions.

We expect that further optimization of these scalable treatments, along with deeper understanding of the nature of these shallow surface states and resulting recombination pathways, will lead to solar and light-emitting device efficiencies approaching the theoretical limits with minimal ionic migration.

2.4 Experimental Procedures

2.4.1 Sample Preparation

Glass substrates were washed sequentially with soap, de-ionized water, acetone, and isopropanol, and finally treated under oxygen plasma for 10 min. Thin films of $MAPbI_3$ were solution processed by employing a methylammonium iodide (MAI) and lead acetate $Pb(Ac)_2 \cdot 3H_2O$ precursor mixture with a hypophosporous acid (HPA) additive [100]. MAI (Dyesol) and $Pb(Ac)_2 \cdot 3H_2O$ (Sigma-Aldrich) were dissolved in anhydrous N,N-dimethylformamide at a 3:1 molar ratio with final concentration of 37 wt% and HPA added to an HPA:Pb molar ratio of 11%. The precursor solution was spin coated at 2,000 rpm for 45 s in a nitrogen-filled glove box, and the substrates were then dried at room temperature for 10 min before annealing at 100°C for 5 min.

All samples were then stored in a nitrogen-filled glove box until used.

2.4.2 Macro-photoluminescence Measurements

PL measurements were acquired by photo-exciting perovskite films on coverslips enclosed in a custom-built flow chamber capable of flowing ultra-high purity gases in ultra-dry or controllably humidified form (40%–50% relative humidity for all humidified measurements). The samples were photo-excited with a 532-nm CW laser at intensities approximately equivalent to the photon fluxes of 2 sun irradiation (150 mW/cm^2). The PL was collected using fiber-coupled collecting optics and the emission detected using an Ocean Optics USB4000 fiber-coupled spectrometer.

The external PL quantum efficiency (η_{meas}) was measured using an integrating sphere in a nitrogen-filled glove box using a 532-nm excitation laser at an illumination intensity of 150 mW/cm^2. The PLQE was computed using well-established techniques [18]. The internal PLQE η was calculated by accounting for collection losses in the measured values η_{meas} due to photon recycling and poor light out-coupling at the perovskite/air and perovskite/glass interfaces, given by:

$$\eta_{meas} = \eta\left(\frac{\eta_{esc}}{\eta_{meas}} - (\eta_{esc} - 1)\right)^{-1} \tag{2.2}$$

where $\eta_{esc} = 12.7\%$ is the escape probability of a photon from a bare perovskite film on glass for the film thickness in this work [68]. The PLQE measurements in other environments were then determined with respect to the PLQE values measured directly in dry nitrogen.

Macroscopic time-resolved PL measurements were obtained on the treated films in dry nitrogen using an Edinburgh LifeSpec spectrometer equipped with a single-photon counter. The films were excited at 405 nm with a picosecond pulsed diode laser (Hamamatsu, M8903-01) at a repetition rate of 20 kHz.

2.4.3 Micro(Confocal)-photoluminescence Measurements

Confocal PL maps were acquired using a custom-built time-correlated single-photon counting confocal microscope (Nikon Eclipse Ti-E) set up with a 1003 oil objective (Nikon CFI PlanApo Lambda, 1.45 NA). The samples were measured in the custom-built flow chamber with the desired gas and/or humidity level. The coverslip samples were photo-excited through the glass side using a 405 nm laser head (LDH-P-C-405, PicoQuant GmbH) with pulse duration of <90 ps, fluence of 1 mJ/cm^2/pulse, and a repetition rate of 0.5 MHz. The PL from the sample was collected by the same objective, and the resulting collimated beam passes through a long-pass filter with a cutoff at 416 nm (Semrock Inc., BLP01-405R-25) to remove any residual scattered or reflected excitation light. Light soaking was achieved by coupling a green 532-nm laser diode (Thorlabs) into the microscope, yielding a soaking spot size of $\sim$10 μm and a power of $\sim$2 μW. A single-photon detecting avalanche photodiode (APD) (MPD PDM Series 50 mm) was used for the detection. The sample was scanned using a piezoelectric scanning stage. The measurements were acquired using the commercial software SymphoTime 64 (PicoQuant GmbH).

2.4.4 Time-Resolved Microwave Conductivity Measurements

For the TRMC measurements, the treatments to the perovskite films were performed in a glove bag using controlled atmosphere and humidity. For light soaking, we applied an LED white light source (LuxSpot LS17-002D55) generating a similar number of photons in the visible as simulated sunlight (100 mW/cm^2, AM1.5). The treatment was performed in a glove bag with a humidity meter. The bag has two gas purges: one introduces dry gas and the other introduces a water bubbler that is connected to the gas source. The relative humidity was controlled to be $\sim$40%–50% for any treatments involving humidity. The treatment time was fixed at 30 min for all. After the treatment, the samples were immediately transferred into a N_2 glove box and then mounted in a sealed microwave resonance cavity for TRMC measurements.

The TRMC technique monitors the change in reflected microwave power by the

loaded microwave cavity upon pulsed laser excitation. The photoconductance (ΔG) of the samples was deduced from the measured laser-induced change in normalized microwave power ($\Delta P/P$) by

$$-K\Delta G(t) = \frac{\Delta P}{P} \tag{2.3}$$

where K is the sensitivity factor. The yield of generated free charges ϕ and mobility $\sum \mu = (\mu_e + \mu_h)$ were obtained by:

$$-\phi \sum \mu = \frac{\Delta G}{I_0 \beta e F_A} \tag{2.4}$$

where I_0 is the number of photons per pulse per unit area, β is a geometry constant of the microwave cell, e is the elementary charge, and F_A is the fraction of light absorbed by the sample at the excitation wavelength of 500 nm (0.73).

2.4.5 Device Fabrication and Characterization

FTO-coated glass sheets (7 Ωcm^{-1}; Hartford Glass) were etched with zinc powder and HCl (3 M) to obtain the required electrode pattern. The sheets were then washed with soap (2% Hellmanex in water), deionized water, acetone, and isopropanol, and finally treated under oxygen plasma for 10 min to remove the last traces of organic residues. All chemicals were purchased from Sigma-Aldrich and used as received unless otherwise stated. A compact layer of SnO_2 was then deposited using a slight modification of the process reported by Anaraki et al. [2]. A first layer of SnO_2 was deposited onto the cleaned FTO substrate by spin coating a layer of $SnCl_4 \cdot 5H_2O$ (17.5 mg/mL) diluted in anhydrous isopropanol (3,000 rpm), followed by annealing at 180°C for 60 min. The substrates were then immersed in an acidic chemical bath of $SnCl_2 \cdot 2H_2O$ for 180 min at 70°C. The substrates were then briefly sonicated in deionized water before being transferred to a hotplate and annealed at 180°C for a further 60 min, after which they were allowed to cool down naturally to room temperature. After cooling, a 0.5 M solution of 1:1.06 MAI (Dyesol) to PbI_2 (TCI

Chemicals, 99% purity) in the ACN/MA solvent was prepared as described by Noel et al. [61]. The solution was then spin coated onto the substrate at 2,000 rpm for 45 s in dry air, resulting in the formation of a smooth, dense, perovskite layer. The substrate was then heated at 100°C for 60 min. After annealing, the substrates were allowed to cool to room temperature. For lead-acetate-based devices, lead acetate trihydrate and methylammonium iodide were dissolved in dimethylformamide at a 1:3 molar ratio, such that the resulting solution was 30 wt% with respect to perovskite salts. Hypophosphorous acid was added according to the method described by Zhang et al. [100]. The precursor solution was then spin coated onto the substrates at 2,000 rpm for 45 s in an inert atmosphere. The substrates were then dried at room temperature for 10 min before being annealed at 100°C for 5 min. After annealing, the substrates were allowed to cool down naturally to room temperature.

The light- and atmosphere-soaking treatments were performed on these half-constructed devices under the stated atmospheric conditions by illuminating with a white light LED array with an intensity similar to simulated sunlight for 20 min. The hole transporting material spiro-OMeTAD was then dissolved in chlorobenzene with additives at a concentration of 30 mM lithium bis(trifluoromethanesulfonyl)imide and 80 mM tert-butylpyridine and spin coated at 2,000 rpm (45 s) on top of the samples in a nitrogen glove box. The devices were then stored in a dry air desiccator overnight before the deposition of the electrodes. Lastly, 80-nm-thick gold electrodes were evaporated onto the devices through a shadow mask, using a thermal evaporator. Devices were stored in nitrogen-filled glove box between measurements.

The current density-voltage (J-V) curves were measured (2400 Series SourceMeter, Keithley Instruments) under simulated AM 1.5 sunlight at 100 $mWcm^{-2}$ irradiance generated by an Abet Class AAB sun 2000 simulator, with the intensity calibrated with an NREL calibrated KG5 filtered Si reference cell. The mismatch factor was calculated to be less than 1%. The solar cells were masked with a metal aperture to define the active area to be 0.0925 cm^2. The devices were held at 1.4 V under illumination for 5 s before the current-voltage scans were taken. The sweeps were taken from 1.4 V to 0 V, then from 0 V to 1.4 V. The scan rate was 0.15 V per

second. All devices were tested under ambient conditions.

Chapter 3

The Impact of Atmosphere on the Local Luminescence Properties of Metal Halide Perovskite Grains

3.1 Introduction

Metal halide perovskites have ushered in a paradigm shift for optoelectronics, with the potential to fabricate solar photovoltaics (PV) and light-emission devices which are both high performance and inexpensive [79]. One unique feature is their remarkable tolerance to defects, allowing thin films to be fabricated by relatively crude solution-processing methods whilst still achieving high crystallinity [78], strong absorption [20] and long charge carrier diffusion lengths[77, 37]. Although recent mixed-cation, mixed-halide alloyed configurations have shown enhanced stability and performance, methylammonium lead iodide ($MAPbI_3$) represents the archetypical perovskite system for understanding material and optoelectronic behaviour [70]. Perovskite-based PV devices on small laboratory prototype scales have demonstrated power conversion efficiencies (PCE) exceeding 22% [95], which is approaching those of established

Chapter 3 is adapted with permission from Brenes et al., The Impact of Atmosphere on the Local Luminescence Properties of Metal Halide Perovskite Grains, Adv. Mater. 2018, 30, 1706208. https://doi.org/10.1002/adma.201706208

thin-film technologies. Light-emitting diodes (LEDs) have shown external quantum efficiencies between 8-12 % over several emission colours [91, 87, 17], and lasing properties have also been demonstrated [80].

Nevertheless, despite impressive progress, the performance of these perovskite films are still limited. For instance, the photoluminescence quantum efficiency (PLQE) of thin films corresponding to high device performances are still far from unity, with typical measured values on the order of ∼1-10% at excitation intensities equivalent to solar illumination [75]. This is consistent with a sizeable density of sub-gap trap states that act as non-radiative recombination centers but can be filled with charge carriers at higher intensities [23, 6, 1, 76, 56]. These trap states are heterogeneously distributed on the microscale [24] leading to a grain-to-grain heterogeneity in optoelectronic properties such as photoluminescence [19], photocurrent and photovoltage [44, 101, 31]. In order for a PV or LED to reach its theoretical performance limits, recombination should be entirely radiative with all non-radiative recombination eliminated [49].

A thorough understanding of what factors influence the non-radiative decay pathways (i.e. what makes a 'dark' grain poorly luminescent), as well as elucidating ways to remove these unwanted phenomena, will be critical in taking this technology towards commercialisation. Previous work has demonstrated that light-soaking films could lead to reductions in trap density and enhancements in luminescence properties [76, 22, 82, 93]. These enhancements correlated with a photo-induced migration of iodide species away from the illuminated region, suggesting that the traps are related to halide species and/or their corresponding vacancies [52].

Tian et al. [82] and Galisteo-Lopez et al. [30] recently reported that the photobrightening effects were further enhanced in the presence of oxygen. Other groups reported that exposure of the films to moisture during preparation or through a post-treatment was crucial in obtaining reasonable luminescence and device performance [65, 54, 98, 27]. In Chapter 2, we showed that particular combinations of wide-area light soaking with atmospheric exposure could lead to remarkably high macroscopic internal PLQE values which approach 100%. These results are consistent with recent

reports on perovskite single crystals in which the surface photoluminescence properties were shown to be modulated by the adsorption of oxygen and water molecules [29, 34]. In other work, oxygen has been reported to be detrimental to the photoluminescence properties and also the device and material stability, particularly with exposure over hours to days in the presence of light [3, 4]. Likewise, moisture is known to be detrimental to perovskite stability by acting on the highly hygroscopic organic cation (e.g. methylammonium)[47]. Finally, some reports have found that light exposure actually decreases the PL of the film [33, 58]. Many of these results are conflicting and the community has not yet reached a consensus on the impact that light, in conjunction with each specific environment, has on the optoelectronic properties. It will be particularly crucial to understand these phenomena on the microscale level, a length scale in which we see substantial local luminescence losses that must be eliminated.

In this chapter, we explore the impact of light-soaking individual $MAPbI_3$ grains in polycrystalline films while immersing them with different atmospheric treatments. We use in situ micro-photoluminescence (PL) measurements to show that the response of each grain to continuous illumination depends sensitively on both the atmospheric environment and the nature of the specific grain, i.e. whether it shows good (bright grain) or poor (dark grain) luminescence properties. We find that both bright and dark grains show a small decrease in emission intensity under illumination over time in dry nitrogen. If they are instead illuminated in the presence of oxygen or moisture, the emission from the more defect-rich dark grain rises substantially while the emission from the less-defective bright grain is constant. For the synergistic combination of illumination during exposure to both air and humidity, the properties of the dark grains approach those of the bright grains, leading to extremely stable and highly luminescent grains. We explain our results using density functional theory calculations to compute the adsorption energies of each molecule on the perovskite surfaces. We find that oxygen molecules bind particularly strongly to iodide vacancies which, in the presence of photo-excited electrons, leads to passivation of the carrier trap states that arise from these vacancies. Our work resolves the seemingly conflicting literature

to date and reveals the strong influence of atmospheric molecules on the perovskite emission properties.

3.2 Results

3.2.1 Local Grain Luminescence Under N_2

High quality thin films (∼250 nm thickness) of $MAPbI_3$ perovskite were deposited on cover slip glass by spin-coating a lead-acetate-based precursor solution containing a hypophosporous acid additive, followed by annealing of the films (see Methods) [100]. A confocal PL map of the resulting film measured under dry nitrogen is shown in Figure 3-1a, clearly showing the grain-to-grain heterogeneity in emission. In a nitrogen atmosphere, we light-soak the grains highlighted with the circles in Figure 3-1a over 5 minutes (total photon dose of ∼150 J/cm^2 for all measurements herein), and we show the PL count rate over time under illumination in Figure 3-1b for a bright grain (blue circle in a) and in Figure 3-1c for a dark grain (pink circle in a). Under dry nitrogen, both bright and dark grains show an initial drop in emission over several minutes that eventually stabilises at a lower PL level and slowly rises over longer periods. There is a negligible change in local lifetime for these grains light-soaked in dry nitrogen (see Appendix B, Figure B-1). When the sample is now exposed in-situ to humidified nitrogen (45% relative humidity), we see strikingly different behavior. The bright grain now shows a rise over time under illumination, while the baseline level of the dark grain increases in the presence of moisture (∼ 2× the initial value) and also continues to rise over time under illumination. We show the local PL decays of the same grains in Figure 3-1d and e. The lifetime of the bright grain (Figure 3-1d) increases after exposure to humidified nitrogen but does not substantially change after additional light soaking. The dark grain (Figure 3-1e) has a very short initial lifetime, which is increased upon exposure to humidity and further increased with light soaking, with the final lifetime approaching that of the bright grain. The net effect of light soaking in humidity is that the dark and

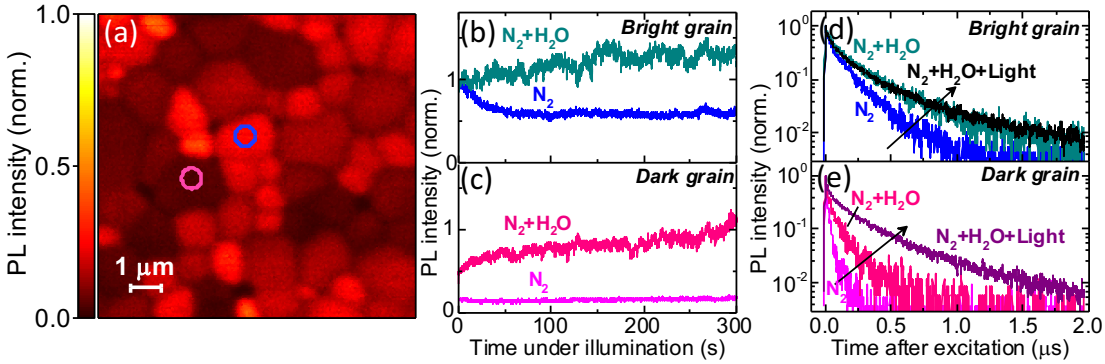

Figure 3-1: *Microscale photoluminescence properties in dry and humid nitrogen.* (a) Confocal PL map of a $MAPbI_3$ perovskite film in dry nitrogen normalised to the maximum intensity. (b, c) Monitoring the PL intensity (emission count rate) over time under illumination from (b) a bright grain (blue circle in a) and (c) a dark grain (pink circle in a) under dry nitrogen and under humidified (45% relative humidity) nitrogen. The PL intensity for each trace over time is given relative to the starting value for the bright grain in nitrogen, which is normalised to 1. (d, e) PL decays from the same (d) bright and (e) dark grains under dry nitrogen, and before and after light soaking in humidified nitrogen. Samples were photoexcited with a 405 nm laser with a repetition rate of 0.5 MHz and a fluence of $\sim 1\ \mu J/cm^2$/pulse ($\sim$500 mW/cm^2), and this same laser was used for local light-soaking (total photon dose of $\sim$150 J/cm^2).

bright grains reach similar intensities and lifetimes. We note that the increase in both local PL lifetime and local PL intensity is consistent with reduced non-radiative recombination in that local area [94].

3.2.2 Local Grain Luminescence Under O_2

In Figure 3-2, we show the same measurements but now performed in the presence of oxygen molecules (compressed air) instead of pure nitrogen. In the case of dry air, we now find that bright grain exhibits stable PL over time (Figure 3-2b), while the dark grain, which likely has a higher defect density than the bright grain, shows significant PL enhancement under illumination and eventually reaches the same intensity as the bright grain (Figure 3-2c). This is also reflected in the larger increase in the PL lifetime following the illumination dose for the dark grain (Figure 3-2e) than for the bright grain (Figure 3-2d). Upon introducing water molecules to the system ($\sim$45% relative humidity), we see an initial baseline increase (i.e. before any light-soaking)

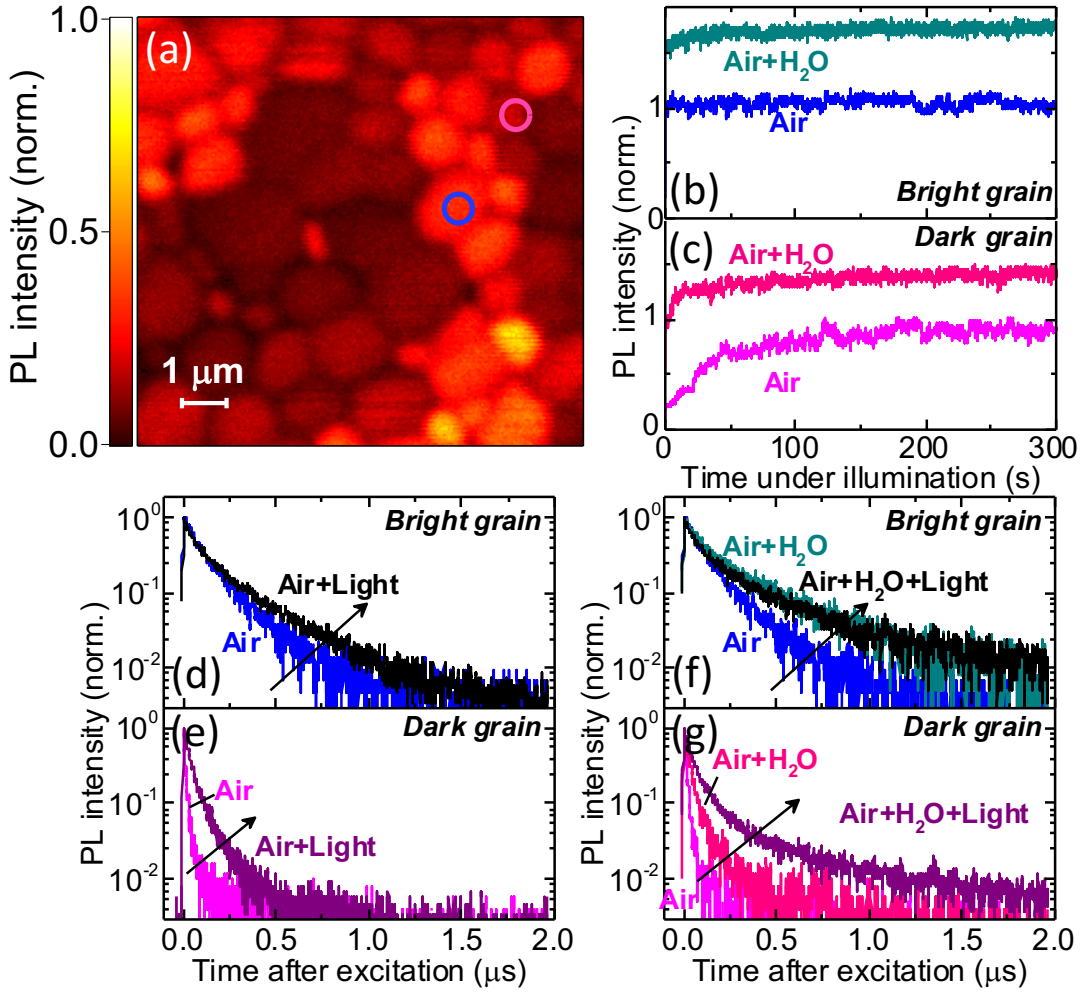

Figure 3-2: *Microscale photoluminescence properties in dry and humid air.* (a) Confocal PL map of a $MAPbI_3$ perovskite film in dry air normalised to the maximum intensity. (b, c) Monitoring the emission (PL count rate) over time under illumination from (b) a bright grain (blue circle in a) and (c) dark grain (pink circle in a) under dry air and under humidified (45% relative humidity) air. The PL intensity for each trace over time is given relative to the starting value for the bright grain in air, which is normalised to 1. (d, e) PL decays from the same (d) bright and (e) dark grains under dry air before and after the light-soaking. (f, g) PL decays from the same (f) bright and (g) dark grains under dry air, humidified air, and after the light-soaking in humidified air. Samples were photoexcited with a 405 nm laser with a repetition rate of 0.5 MHz and a fluence of $\sim$1 μJ/ cm^2/pulse ($\sim$500 mW/cm^2), and this same laser was used for local light-soaking (total photon dose of $\sim$150 J/cm^2).

in the emission intensity for both bright (Figure 3-2b) and dark (Figure 3-2c) grains. By contrast, we note that a baseline increase in the dark in dry air conditions is only observed when the samples are stored in compressed air for periods of hours (Figure B-2), suggesting that the impact of oxygen molecules in the dark is much more slowly acting than water molecules in the dark. The emission from both bright and dark grains in humid air then slowly rises over time under illumination, again with a greater relative increase for the dark grain than the bright grain. The local PL lifetimes for the bright grain (Figure 3-2f) increase upon humidity exposure but then do not substantially increase further under illumination, while the dark grain (Figure 3-2g) shows an additional increase after illumination. These collective observations highlight that the presence of molecules such as oxygen or moisture is vital for substantial net PL enhancement of grains under illumination, and that the presence of both oxygen and moisture under light are synergistic. In contrast, illumination in a nitrogen environment without any other atmospheric (oxygen or humidity) exposure during processing or as a post-treatment leads to net decreases in emission (cf. Figure 3-1). We note that the PL intensity drops even more substantially and continually under light in vacuo (i.e. in the absence of any atmospheric molecules, Figure B-3). We also note here that these enhancements are seen after just brief exposure to oxygen, humidity and light (on order 10 minutes), but longer term exposure to oxygen, humidity and light (on order of hours to days) leads to degradation [3, 4]. We also reiterate that such significant enhancements require illumination of either local grains or many grains, highlighting the key role of light in these brightening processes [22].

3.2.3 Local Grain Luminescence After Humidity Exposure

In Figure 3-3a, we show the confocal PL map of the same sample as in Figure 3-2a but now after exposure to humid air (45 % relative humidity) for 60 minutes and then returning to dry air, revealing an increase in the baseline PL intensity and more uniform emission distribution compared to before the humidity exposure [27]. Remarkably, we find that individual grains now show exceptional PL stability after this exposure, regardless of whether they were dark or bright or previously illuminated

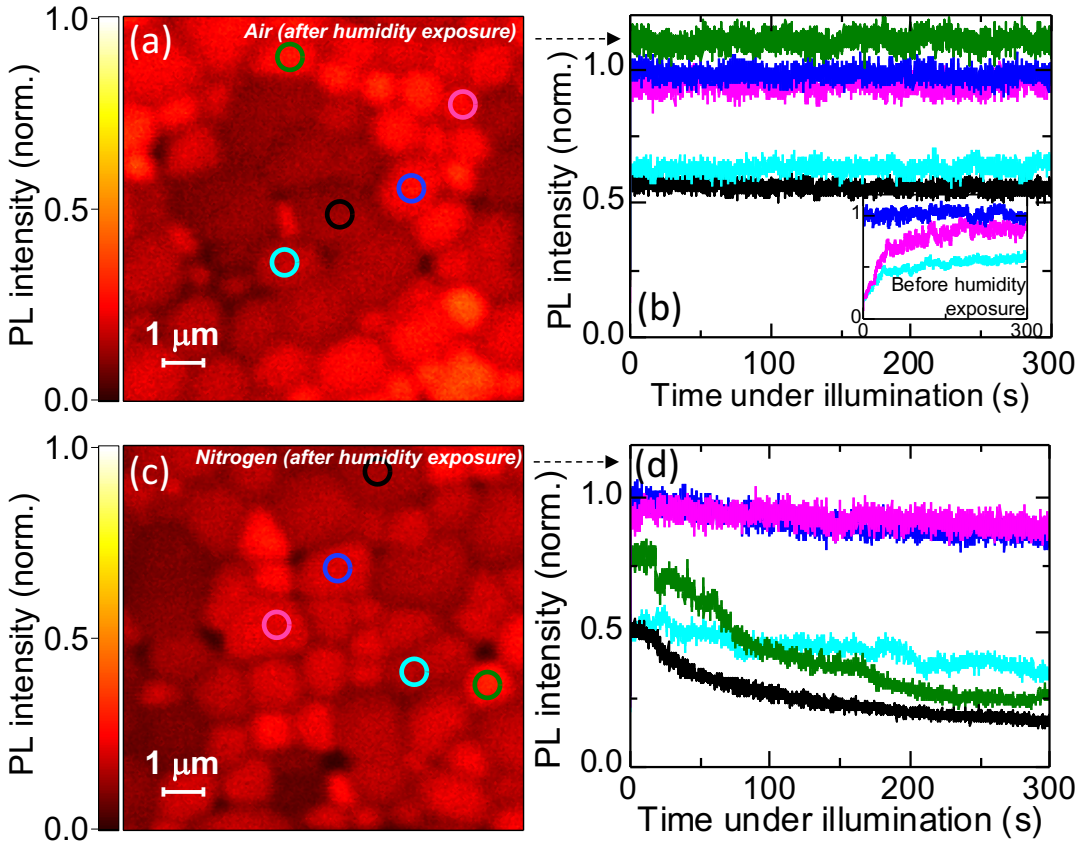

Figure 3-3: *Local grain emission stability after humidity exposure.* (a) Confocal PL map of a $MAPbI_3$ perovskite film in dry air following exposure to humid air for 60 minutes, normalised to the same intensity value as Fig. 3-2A to allow direct comparison. (b) Monitoring the emission intensity (count rate) from various bright and dark grains denoted in (a) over time under illumination, normalised to the intensity of the same grain as in Fig. 3-2b. Inset: emission from the same grains under continuous illumination before the exposure to humidity. (c) Confocal PL map of a $MAPbI_3$ perovskite film in dry nitrogen following exposure to humid nitrogen for 60 minutes, normalised to the same intensity value as Fig. 3-1a. (d) Monitoring the emission intensity (count rate) from various bright and dark grains denoted in (c) over time under illumination, normalised to the intensity of the same grain as in Fig. 3-1b. Samples were photoexcited with a 405 nm laser with a repetition rate of 0.5 MHz and a fluence of $\sim$1 μJ/cm^2/pulse ($\sim$500 mW/cm^2), and this same laser was used for local lightsoaking (total photon dose of $\sim$150 J/cm^2).

or not (Figure 3-3b; grain highlighted by green circle was not previously light-soaked). This can be compared to the PL of the same grains before the humidity exposure in which the darker grains in particular exhibit slow transient rises under illumination (Figure 3-3b inset and Figure B-4). By contrast, this same PL stability is not observed when the humidity exposure is performed in nitrogen rather than air (Fig. 3-3c and d). This suggests that the combination of both air and humidity is essential for attaining exceptional grain luminescence stability, where the introduction of humidity in general leads to less reversible effects. We note that the absolute emission intensity is also increased if exposed to light during the humidity exposure (cf. Fig. 3-1 and 3-2). We also note that the grains are not always stable while light-soaking in humid air conditions, though after drying the system even these grains retain excellent stability (Figure B-5).

3.2.4 Density Functional Theory Calculations

In order to understand these PL observations at the atomic scale we performed density functional theory (DFT) calculations involving the adsorption of N_2, O_2 and H_2O molecules onto the (110) and (001) surfaces of $MAPbI_3$. Previous studies on $MAPbI_3$ surfaces have examined the (001) and (110) surface structures [36, 72] with recent atomic-scale structural and simulation studies on molecular interactions at perovskite halide surfaces [57, 35, 51, 32, 43]. Ab initio simulation work of Zhang and Sit [99] considered the role of excess electrons and oxygen in the degradation of $MAPbI_3$ with the creation of superoxide species which react with the (110) surface to form Pb-O bonds. However, there is currently no report of a systematic comparison of the adsorption energetics and surface electronic structures for N_2, O_2 and H_2O on $MAPbI_3$ surfaces.

To simulate the effect of illuminated and dark conditions we allowed each surface to have three charge states: positively charged, negatively charged and neutral (dark conditions, no photoexcitation). Since it is well known that the surface regions of $MAPbI_3$ can contain high numbers of iodine vacancies [36], we have considered both defect-free (PbI_2-terminated) and iodine-vacancy-rich surface terminations. We note

that the absolute halide vacancy concentration will be higher in the illuminated case due to photo-induced halide migration away from the illuminated surface [22].

We summarise the molecular adsorption energies for N_2, O_2 and H_2O onto an iodine vacancy on a PbI_2-terminated (110) surface of $MAPbI_3$ (see Table B.1 for adsorption energies for binding to Pb^{2+} on the PbI_2-terminated surface and Table B.2 for the (001) configuration). The adsorption energy is relative to the reference situation of infinite separation between the surface and molecule; a negative value indicates a favourable interaction. Three general features are readily apparent from this data. First, the adsorption energies for nitrogen are around –0.15eV and suggest physisorption, in which the interaction with the surface is relatively weak (absolute value typically less than 0.3 eV) [48]; here we find that there is no significant bond formation between the N_2 molecule and perovskite surface. Second, adsorption of H_2O is slightly more favourable, with adsorption energies in the range of –0.46eV to –0.66eV, in good agreement with other computational work [43] and suggesting weak chemisorption including hydrogen bonding. Finally, we find strong adsorption energies (absolute value $>$ 1.3 eV) for O_2 on surfaces where excess electrons are available, such as negatively charged surfaces or those with neutral iodine vacancies. O_2 adsorption onto iodine vacancies where electrons are available is the most favourable (- 3.94 eV). This suggests strong chemisorption of O_2 at $MAPbI_3$ surfaces in which O_2 acts as an electron scavenger; this is associated with a favourable electron transfer process at the perovskite surface to form superoxide (O_2^-) species. Indeed, a lengthening of the O_2 bond is found, which is indicative of superoxide (O_2^-) formation. Although there are currently no experimental energies for direct comparison, the magnitude of our values are highly consistent with data found for the physisorption and chemisorption of simple molecules on solid surfaces [11, 9].

Given these adsorption energy results, we then calculated the surface band structure to examine the effect of adsorption on the electronic structure, and these results are summarised for the (110) configuration in Figure 3-4 (see Figures B-6 to B-9 for all (110) results and Figures B-10 to B-15 for the (001) results). We define trap states as electronic states with energies greater than kT ($\sim$25 meV) below the Fermi

Table 3.1: Adsorption energies of N_2, H_2O, and O_2 molecules onto iodine vacancies on a PbI_2-terminated (110) surface of $MAPbI_3$, with the vacancy in three possible charge states due to photoexcitation. See Table B.1 for adsorption energies for binding to Pb^{2+} on the PbI_2-terminated surface and Table B.2 for the (001) configuration

Adsorbate	Surface site	Charge state	Adsorbtion energy (eV)
N_2	$V_I^{'}$	-1	-0.12
	$V_I^{\times}$	0	-0.14
	$V_I^{\bullet}$	+1	-0.15
H_2O	$V_I^{'}$	-1	-0.66
	$V_I^{\times}$	0	-0.46
	$V_I^{\bullet}$	+1	-0.54
O_2	$V_I^{'}$	-1	-3.94
	$V_I^{\times}$	0	-2.48
	$V_I^{\bullet}$	+1	-0.72

level, which can act to effectively localize charge [84] and trap the carriers, leading to non-radiative decay pathways [75, 56]. Previous computational work on defects in $MAPbI_3$ [36, 25, 14] have found that the iodine vacancy induces electron and hole trapping levels inside the bandgap region.

For the defect-free surface in the dark there are few trap states near the bottom of the conduction band (Fig. 3-4a). For a surface containing a high concentration of iodide vacancies and with excess electrons (Fig. 3-4b) our calculations indicate trap states at the bottom of the conduction band, evidenced by their occupancy in the presence of excess electrons and the shift of the Fermi level (red line) into the conduction band. When N_2 or H_2O is adsorbed there is very little change in the surface band structure (Figs. 3-4c,d). In contrast, when O_2 is adsorbed there is a large reduction in the number of trap states, which shift down to the top of the valence band (Fig. 3-4e), indicative of chemisorption. Recent work [3] has shown that this is due to the O_2 becoming reduced to a superoxide ion (O_2^-), which is of a similar size to the iodide ion; this species effectively replaces the vacant site, thus restoring the full octahedral coordination of Pb.

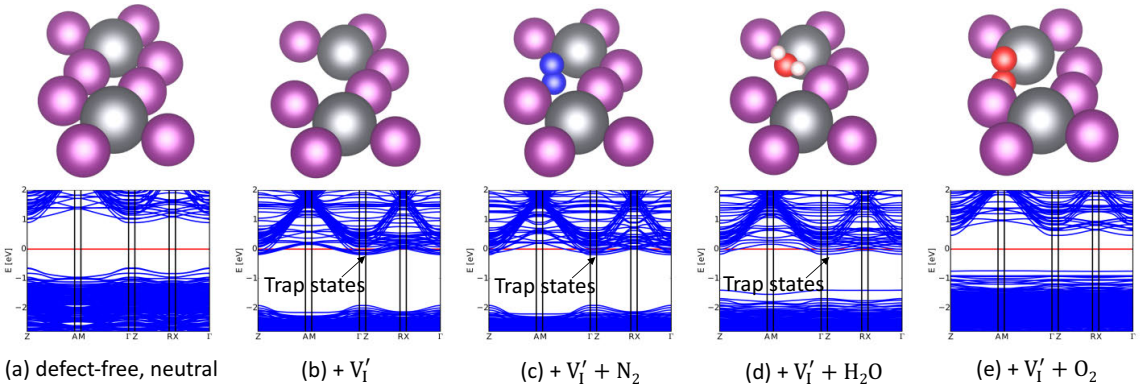

Figure 3-4: *Surface atomic and electronic structures.* Schematic of the local atomic-scale configurations of the surface termination layer (top row) and calculated band structures (bottom row) for the (110) surface of $MAPbI_3$. (a) Pristine uncharged surface, (b) negatively-charged iodine vacancy into which the following molecules are adsorbed; (c) N_2, (d) H_2O and (e) O_2. Key: purple - iodine, grey - lead, blue - nitrogen, red - oxygen, white - hydrogen. We note that our calculations explicitly included excess electrons; hence the Fermi level (red line) is above any trap states because those states are filled. See Figures B-6 to B-9 for other configurations.

3.3 Discussion

These results suggest that adsorption and reduction of O_2 can effectively remove the trap states introduced by excess electrons and vacancies on the surface and in the bulk. The process will be rate-limited by two general factors: (i) illumination that causes photo-induced migration of iodide ions down the illumination profile [22] leading to a gradient of additional iodide vacancies decreasing in density from the surface into the bulk, and (ii) diffusion of O_2 onto these surface and bulk iodide vacancies and the capture of an electron on these sites. Both of these factors may be responsible for the relatively slow PL rises observed in O_2 environments even in very low oxygen concentrations [53]. In particular, the dark grains are expected to have a larger starting density of vacancies than the bright grains, and are perhaps more susceptible to photo-induced vacancy generation; this would lead to lower initial PL levels but larger relative enhancements for the dark grains than the bright grains.

By contrast, the calculations suggest that H_2O adsorption does not cause any significant change in the surface electronic structure and unlikely to be responsible for

the rapid baseline PL rise seen in the experiments in humid conditions. We conclude that the rapid baseline PL increases upon H_2O exposure for grains in both dark and light conditions is not due to an adsorption "defect-healing" process similar to that seen for O_2 . Instead, we suggest that H_2O converts the surface region into a hydrate phase. Leguy et al. [45] have shown that this process of hydrate formation occurs very rapidly. The surface trap states would then be removed by such a conversion reaction, in which a very thin layer of the surface converts to an amorphous shell (of PbI_2 or PbO)[15]. This shell eliminates the surface vacancies and explains the less reversible nature of the effects after exposure to humidity, particular humid air (cf. Fig. 3-3) as in Chapter 2. We note that there is a very slow rise on top of the rapid baseline rise in humid conditions (Fig 3-1.b,c), which may be due to residual trace oxygen in the humidity source or the action of hydroxide ions in filling positively-charged iodine vacancies.

For the case of N_2, the calculations suggest that it has little effect upon the surface electronic structure and the photoluminescence, due to it being unable to undergo either redox activity (like O_2) or promote conversion reactions (like H_2O). Nevertheless, the presence of adsorbed nitrogen molecules still gives more favourable conditions for luminescence than *in vacuo* in which the PL drops continually over time under illumination (cf. Fig. B-3).

Finally, we note that the adsorption energies and density of states data for the (110) surface are very similar to the (001) surface (Figures B-10 to B-15 and Table B.2). It has been reported that the crystal facets of $MAPbI_3$ can display different photovoltaic properties [44]. The data presented here suggest that the effectiveness of the treatment by atmospheric molecules will depend upon the intrinsic concentration of trap states present at a given facet. Finally, we note that here we are comparing in-situ the luminescence of local grains in different environmental conditions under identical excitation conditions (e.g. pulse fluence, wavelength, repetition rate). Future work will be required to explore the potentially large impact of these excitation parameters on the relative luminescence rise or decay in each atmosphere, as well as to investigate whether the enhancements in the presence of atmospheric

molecules and light can be maximised if selectively light-soaking defective grains or when light-soaking the entire film.

In conclusion, we have used confocal photoluminescence measurements to show that the PL properties of $MAPbI_3$ perovskite grains under continual illumination depend sensitively on the type of grain (bright or dark) and type of adsorbed molecules. We find that dark grains show substantial enhancements under illumination in the presence of oxygen and/or water molecules, while bright grains show less of an effect. In nitrogen conditions, illumination leads to a net drop in PL over time, and this is further exaggerated in the absence of any molecules (*in vacuo*). We perform DFT calculations to show that oxygen, in the presence of photo-excited carriers, binds very strongly to iodide vacancies and reduces to superoxide. This removes the sub-gap electron trap states associated with the iodide vacancies, regenerating a band structure similar to the pristine case. We propose that moisture forms a thin passivating shell on the surfaces of the grains, in turn also eliminating the vacancies by converting the surfaces to benign amorphous species. In the absence of passivating molecules, continual illumination generates defects unabatedly. Our work provides a microscale view to resolve the seemingly conflicting literature in the field relating to the beneficial [22, 82, 30, 29] and detrimental [33, 58] effects of light-soaking on the optoelectronic properties of perovskite films, and also provides crucial insights into the elimination of non-radiative decay in these exciting semiconductors. The work also suggests that future work should include searching for other molecules that could have similar passivating effects to O_2 and H_2O but do not lead to longer-term degradation of the films.

3.4 Experimental Section

3.4.1 Photoluminescence Measurements

Confocal photoluminescence (PL) maps were acquired using a custom-built time-correlated single photon counting (TCSPC) confocal microscope (Nikon Eclipse Ti-E)

setup with a 100X oil objective (Nikon CFI PlanApo Lambda, 1.45 NA). The samples were measured in the custom-built flow chamber with the desired gas and/or humidity level, where ultra-high-purity dry gases (Airgas) were used and then controllably humidified. The cover slip samples were photo-excited through the glass-side using a 405 nm laser head (LDH-P-C-405, PicoQuant GmbH) with pulse duration of <90 ps, fluence of $\sim$1 μJ/cm^2/pulse, and a repetition rate of 0.5 MHz. The PL from the sample was collected by the same objective and the resulting collimated beam passes through a long-pass filter with a cut-off at 416 nm (Semrock Inc., BLP01-405R-25) to remove any residual scattered or reflected excitation light. A single photon detecting avalanche photodiode (APD) (MPD PDM Series 50 mm) was used for the detection. Light soaking was achieved by directing the diffraction-limited pulsed laser spot onto a grain and collecting the emission for a period of time. The sample was scanned using a piezoelectric scanning stage. The measurements were acquired using the commercial software SymphoTime 64 (PicoQuant GmbH).

In-vacuo measurements were acquired with the sample in a cryostat (Janis ST-100) at a pressure of $< 10^{-4}$ mbar. The samples was photo-excited with a 532 nm CW laser at intensities approximately equivalent to the photon fluxes of $\sim$2 sun irradiation ($\sim$150 mW/cm^2). The PL was collected using fiber-coupled collecting optics and the emission detected using an Ocean Optics USB4000 fiber-coupled spectrometer.

3.4.2 Ab-initio Calculations

Density functional theory calculations were performed using the numeric atom-centred basis set all-electron code FHI-AIMS [8, 67]. Light basis sets were used with tier 2 basis functions for C, N, H and O. Electronic exchange and correlation were modelled with the semi-local PBE exchange-correlation functional [64]. A gamma point offset grid at a density of 0.04 Å^{-1} was used for k-point sampling. For the treatment of spin orbit coupling we used an atomic zeroth-order regular approximation (ZORA) [8]. Van der Waals forces were accounted for by applying a Tkatchenko-Sheffler electrodynamic screening scheme [83]. Molecules were adsorbed onto an 8 layer surface slab of tetragonal $MAPbI_3$ containing 96 atoms with a vacuum gap of 20Å. Charged

surfaces were compensated using the virtual crystal approximation [69]. Structures were relaxed with convergence criteria of 10^{-4} eV/Å for forces, 10^{-5} electrons for the electron density and 10^{-7} eV for the total energy.

Chapter 4

Conclusion

In this thesis, we demonstrated that the combination of air, moisture and light could lead to surface passivation of perovskite thin films which led to internal PLQEs approaching unity. Remarkably, this represents the first report, to the best of our knowledge, of internal PLQEs for perovskites above 90% and with surface recombination velocities comparable to the best passivated silicon wafers, approaching the properties of single crystal perovskites. As such, we have shown that perovskite thin films have the potential to join gallium arsenide as one of the best optoelectronic semiconductors in terms of absorption and emission.

Furthermore, we showed how nitrogen, oxygen and moisture interact with perovskite films in order to affect their luminescent properties. We resolved conflicting results in literature regarding PL rises and falls for perovskite thin films by revealing the strong atmospheric dependence of PL emission and stability. Further studies are required to determine their interaction with these atmospheres at different illumination intensities, especially at higher powers where bimolecular recombination processes dominate over mono-molecular recombination.

Appendix A

Supplementary Information to Chapter 2

A.1 Kinetic Model

In our model, we assume electron traps, in line with the consensus in the field [89], though we note that the analysis holds for either electron or hole traps. Scheme A-1 shows the recombination and generation pathways (and associated rate equations) affecting the populations of free photo-generated electrons n_e and holes n_h and trapped photo-excited electrons n_t. Upon photo-excitation, electrons are generated in the conduction band with generation rate G_c and rapidly immobilize into these traps. The corresponding valence band holes contribute to the photoconductance until these free holes recombine with the trapped electrons. In the case of photon recycling (Scheme A-1a), the additional generation from photon recycling leads to an effective measured rate constant $k_2^{eff} = \eta_{esc} k_R + k_n$. When photon recycling is excluded (Scheme A-1b), the additional generation term is effectively removed and recombination is governed by the internal rate $k_2^{int} = k_R + k_n$.

We note that all recombination constants as defined here are second order. However, at low fluence in which many electrons are trapped the recombination is limited by the untrapped electrons and appears effectively pseudo-monomolecular [76]. At higher fluences in which many of the traps are filled, bimolecular recombination domi-

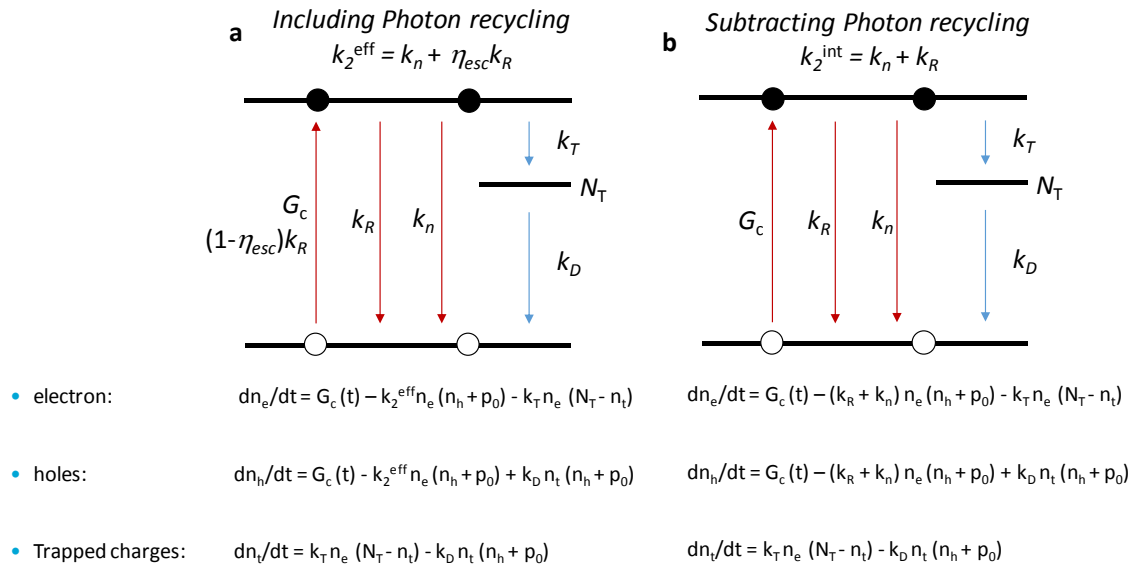

Figure A-1: Schematic of the recombination and generation pathways in the kinetic model (a) with photon recycling and (b) when excluding the effects of photon recycling. G_c is the generation rate, k_R is the radiative bimolecular rate, k_n is the non-radiative bimolecular rate, k_T is the trapping rate, k_D is the trap depopulation rate, N_t is the deep trap density, p_0 is the background hole density [39], η_{esc} is the escape probability of photons [68].

nates. We report the extracted parameters in Table A.1. We note that there is a small change in the emptying rate of these traps k_D, which decreases from $8.0 \times 10^{-10}\text{cm}^3\text{s}^{-1}$ before the treatment to $3.2 \times 10^{-10}\text{cm}^3\text{s}^{-1}$ after the treatment. Although the slower trap emptying would effectively lead to more traps remaining filled for a given excitation density, these changes cannot explain the large increase in emission quantum efficiency observed for the treated samples.

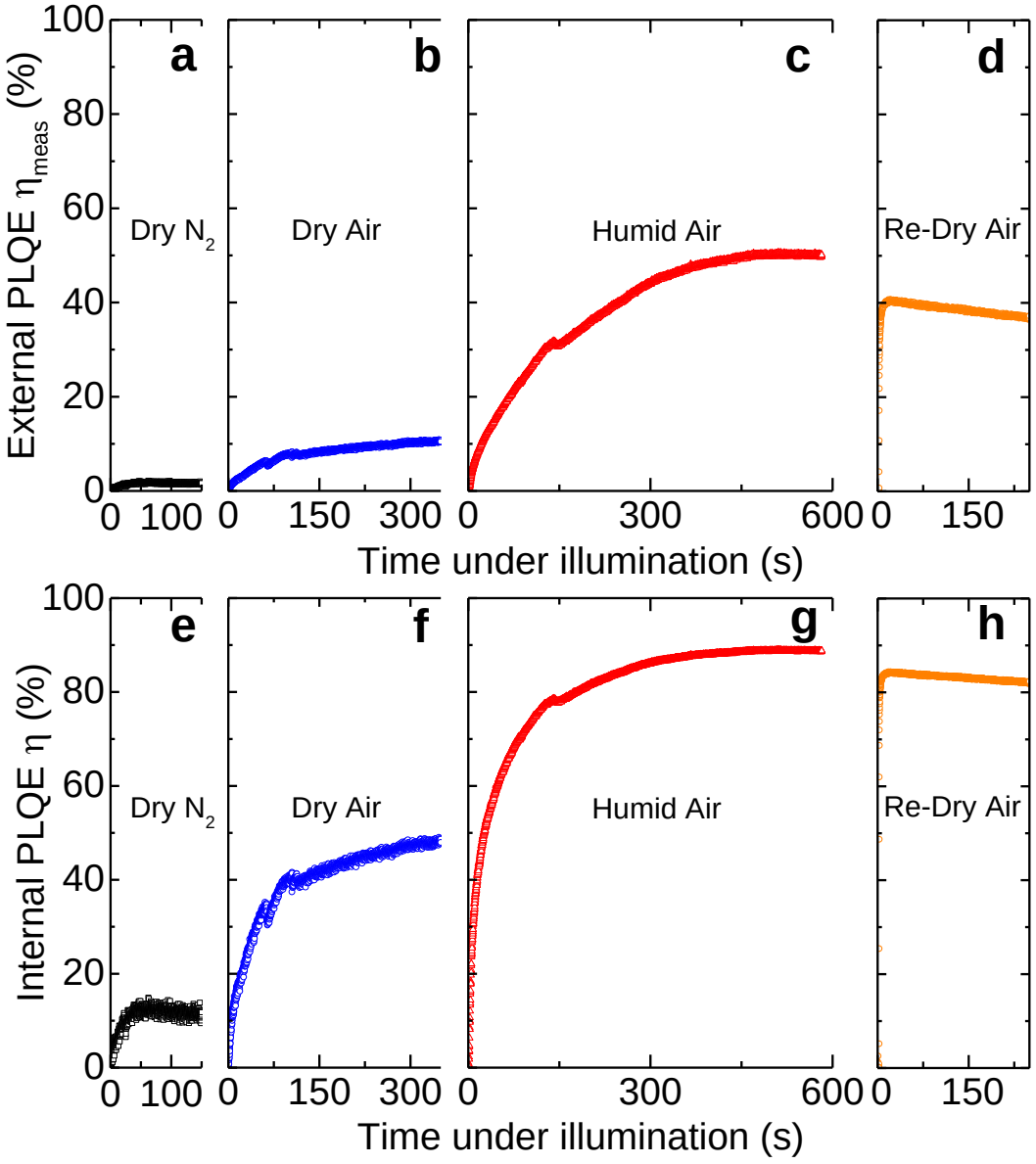

Figure A-2: (a-d) External PLQE η_{meas} measurements over time under illumination with a 532-nm laser at an excitation intensity equivalent to ∼2 sun (∼150 mW/cm^2) in (a) dry nitrogen, (b) dry compressed air, (c) humidified compressed air, and (d) after returning to dry compressed air. (e-h) show the same plots but after converting the external values to internal PLQE η.

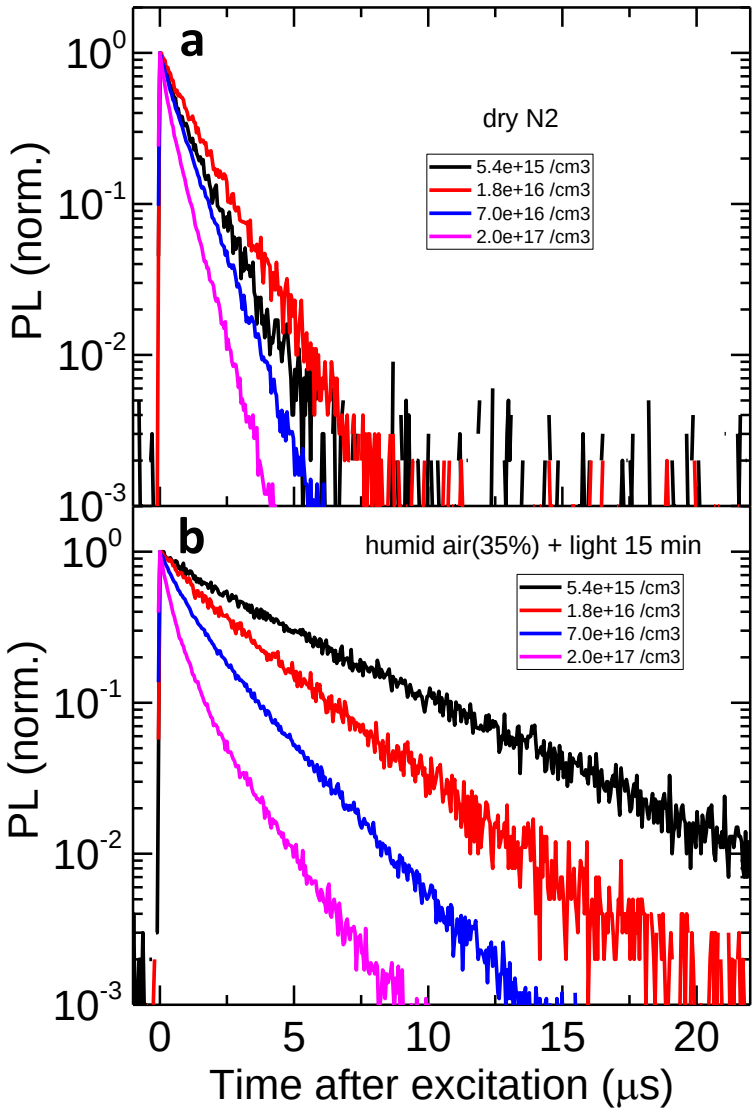

Figure A-3: Time-resolved PL decays of the (a) untreated (dry N_2) and (b) treated (humid air + light, where light is equivalent to 1 sun illumination intensities) samples. Samples were excited with a 405-nm pulsed laser with the stated excitation densities (realized through use of optical filters) and a repetition rate of 20 kHz.

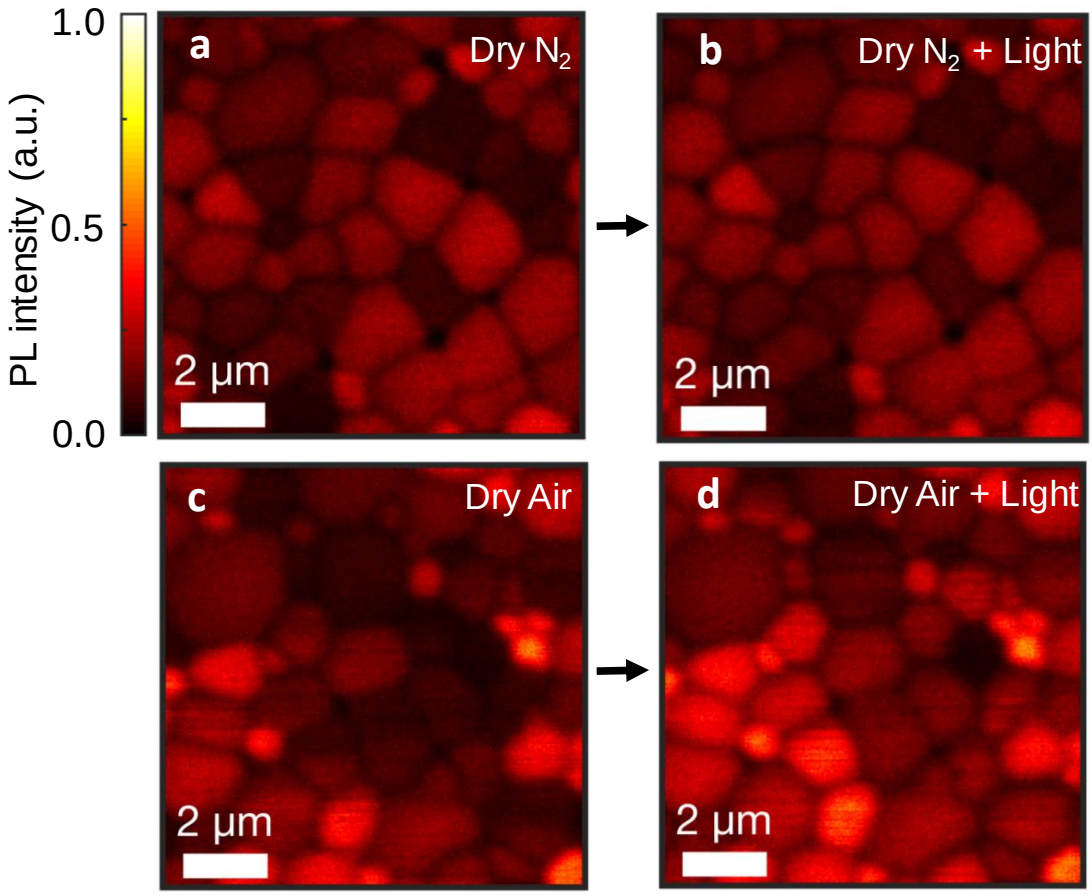

Figure A-4: In-situ confocal PL maps measured in (a) dry N_2, and (b) after light soaking for 10 minutes under excitation with a 532-nm laser equivalent to ∼10 sun under dry N_2. (c-d) Show the same measurements under dry air. PL maps were collected by photo-exciting with a 405-nm laser with a repetition rate of 0.5 MHz and a fluence of ∼1 $\mu J/cm^2$/pulse.

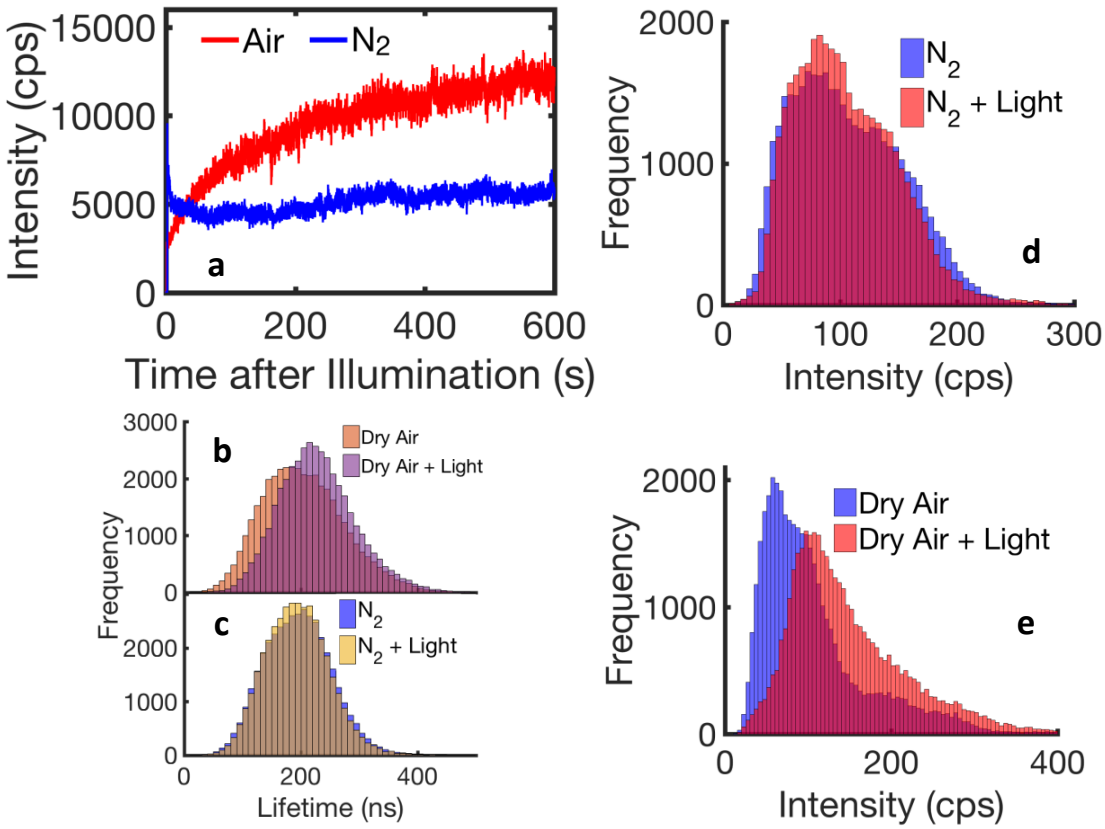

Figure A-5: (a) Emission of the films in Figure A-4a and c in dry air and dry nitrogen during the light-soaking with excitation at 532-nm and intensity equivalent to ∼10 sun. (b, c) Histograms showing the distribution of average lifetimes corresponding to the respective maps in Figure A-4. (d, e) Histograms showing the distribution of emission intensities corresponding to the respective maps in Figure A-4.

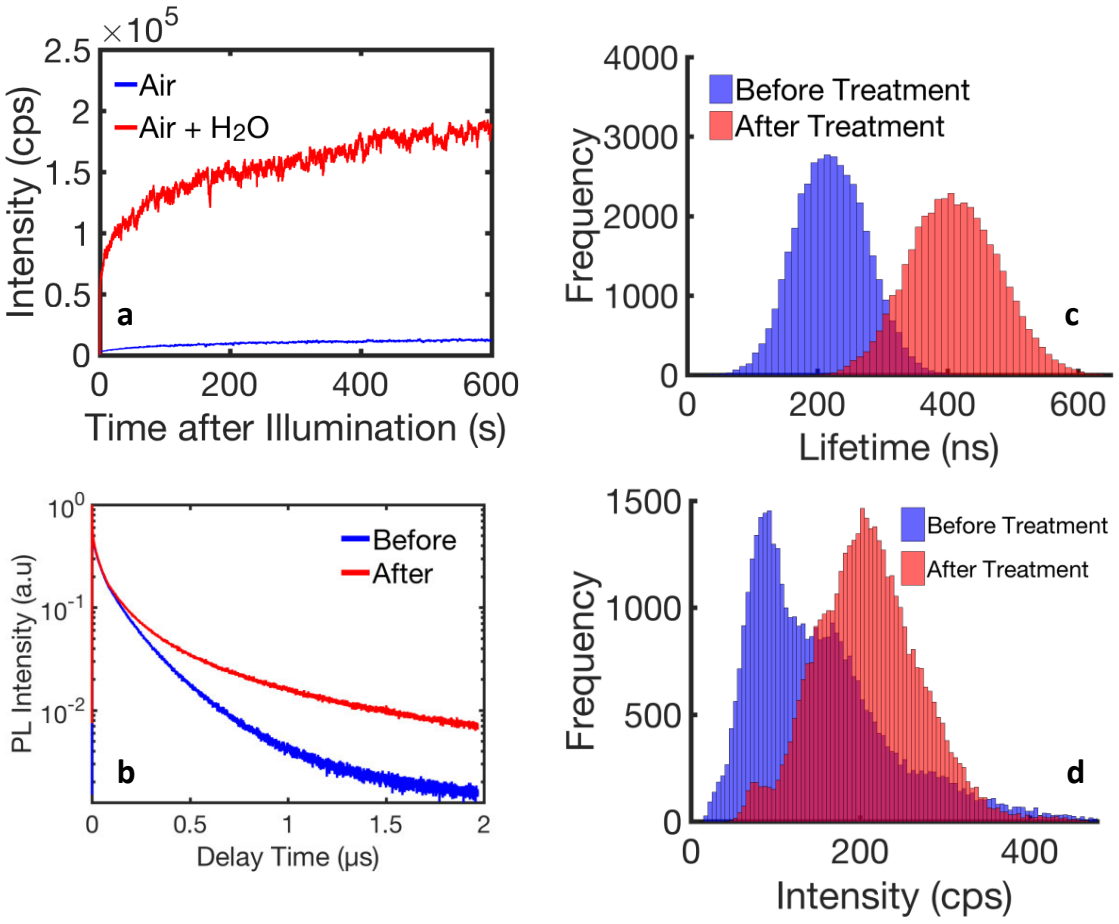

Figure A-6: (a) Emission of the films in Fig. 2-1d-h during the light-soaking with excitation at 532-nm and intensity equivalent to ∼10 sun under the stated atmospheric conditions. (b) The PL decays summed across the map before the treatment (cf. Fig. 2-1d) and after the treatment with light, air and humidity (cf. Fig. 2-1g). The corresponding distributions of the average lifetime and intensity are shown in (c) and (d), respectively.

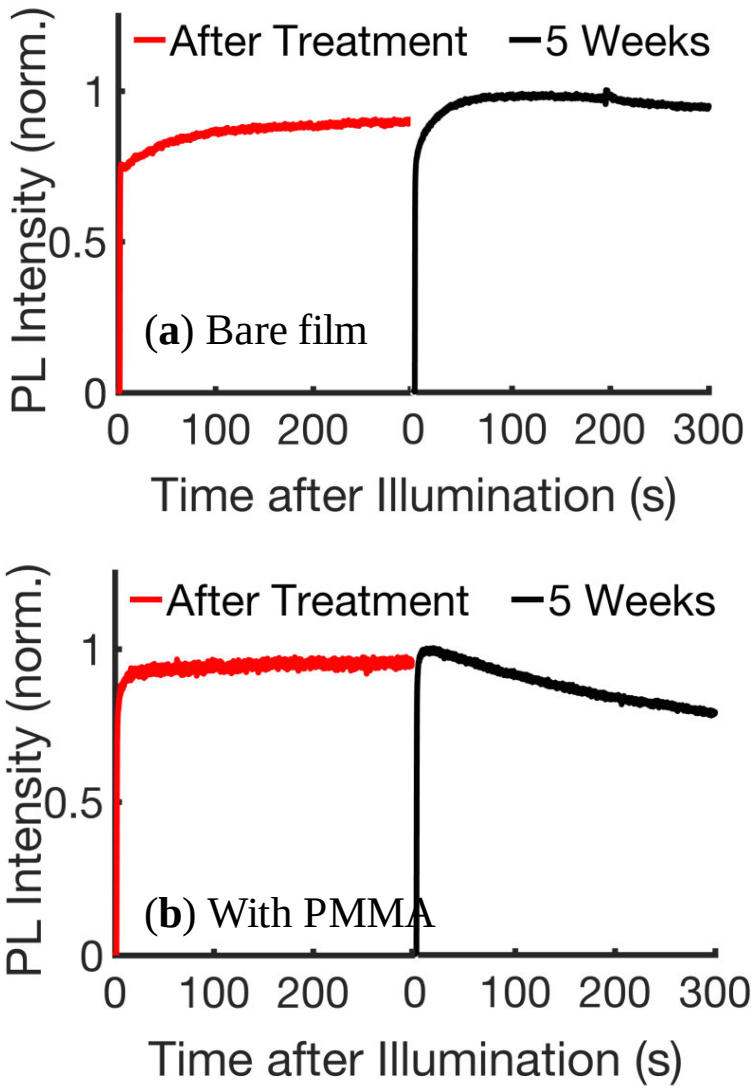

Figure A-7: PL stability immediately after the treatment (red) and after 3 weeks of storage in a nitrogen-filled glove box for a (a) bare film and (b) film coated with a spin-coated layer of PMMA.

A.2 Importance of combination of light, oxygen and humidity

Although there is a baseline increase in emission when introducing air and particularly humidity [27, 98], active illumination under the gas is essential for the large increases in emission intensity and spatial redistribution of emission (Figure A-8). The effect of

light soaking in dry atmosphere is generally reversible over a time scale of hours [22] but the presence of humidity leads to the longer-term retention of the enhancements, with the absolute emission level, stability and retention optimal if exposed to both air and humidity (Figure A-9).

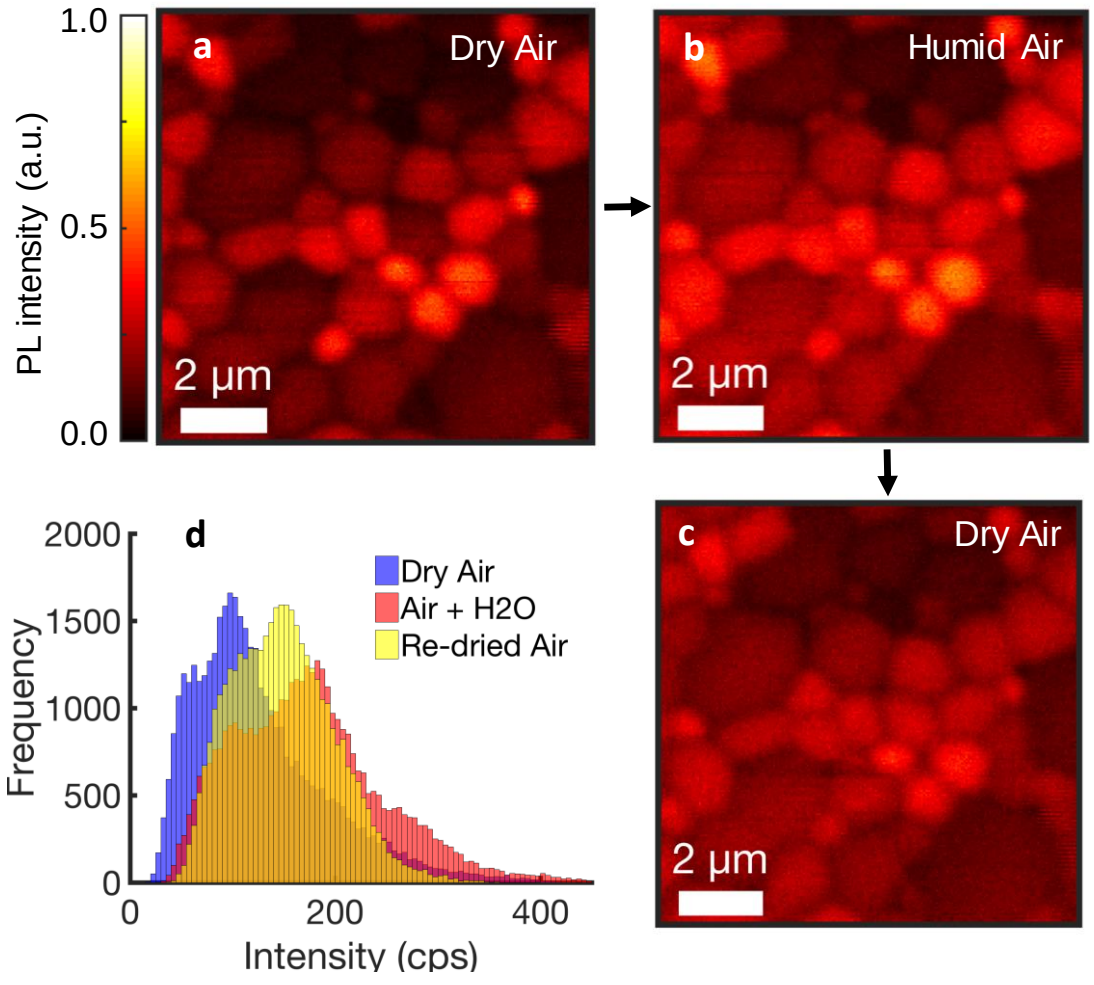

Figure A-8: In-situ confocal PL maps measured in (a) dry air, (b) humidified air, (c) after returning to dry air (i.e. without any light soaking). PL maps were collected by photo-exciting with a 405-nm laser with a repetition rate of 0.5 MHz and a fluence of $\sim$1 μJ/cm^2/pulse. (d) Histograms of the intensity distribution of each map. These distributions should be compared to those in Figure A-6, where illumination under humidity leads to substantial increases in the intensity.

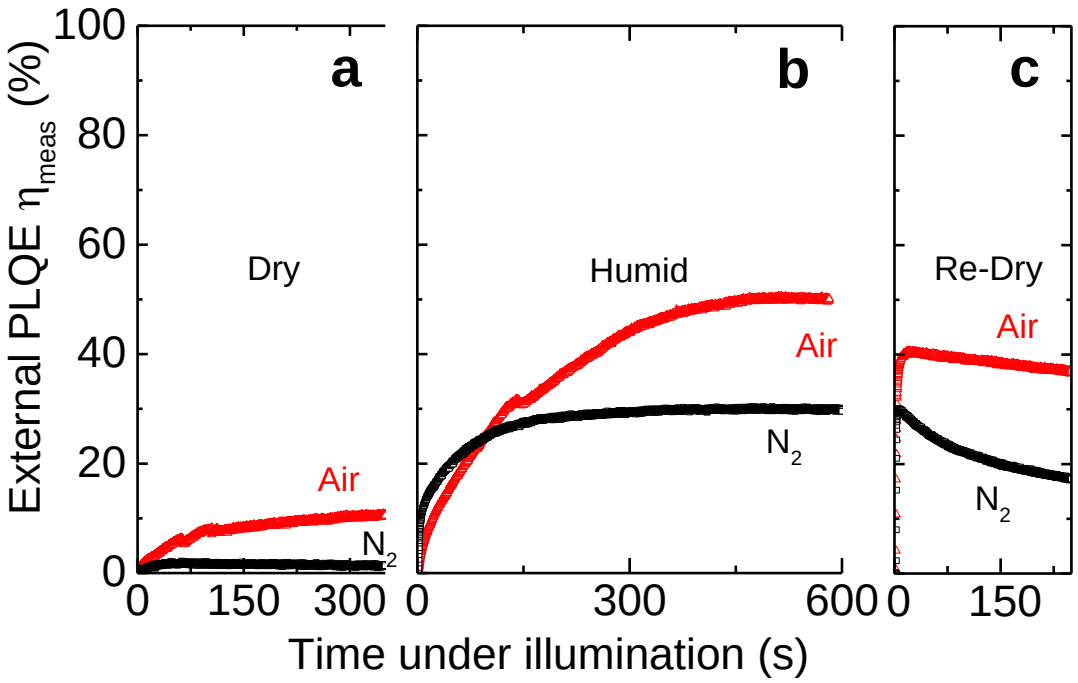

Figure A-9: External PLQE η_{meas} measurements over time under illumination with a 532-nm laser at an excitation intensity equivalent to ∼2 sun (∼150 mW/cm^2) in nitrogen (black) and compressed air (red) under (a) dry conditions, (b) humid conditions, and (c) after returning to dry conditions. The effects are far better retained for the sample light-soaked in air and humidity.

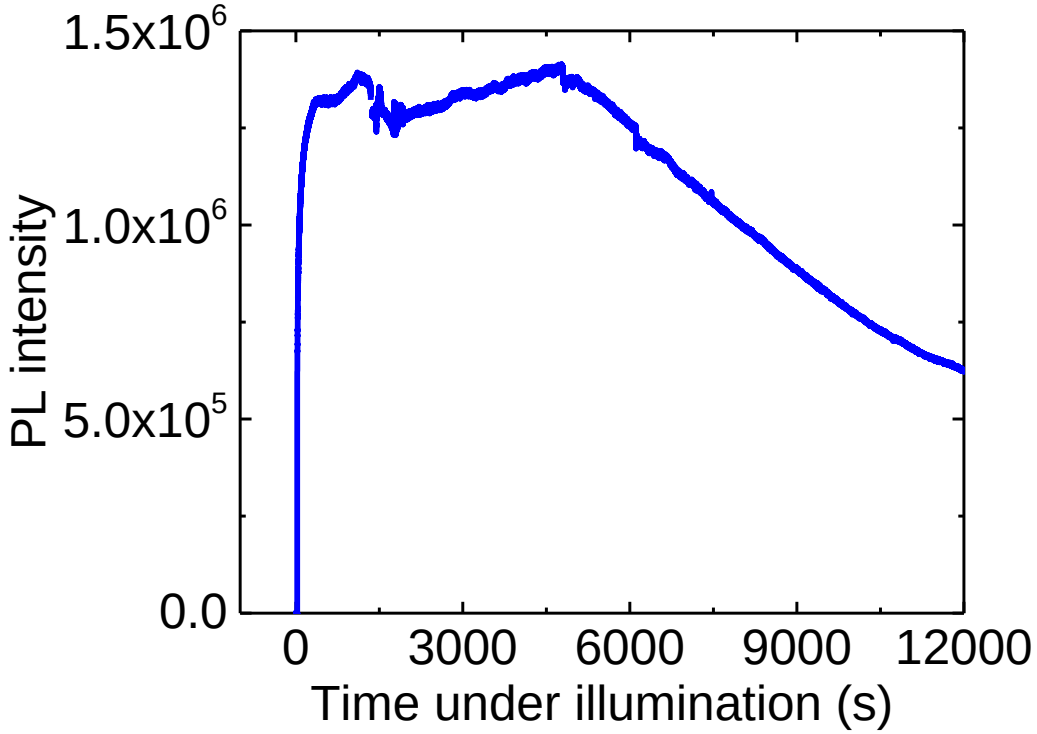

Figure A-10: PL measurements over time under illumination with a 532-nm laser at an excitation intensity equivalent to ∼2 sun (∼150 mW/cm^2) in humidified air (45% RH) showing a decrease in emission at longer times.

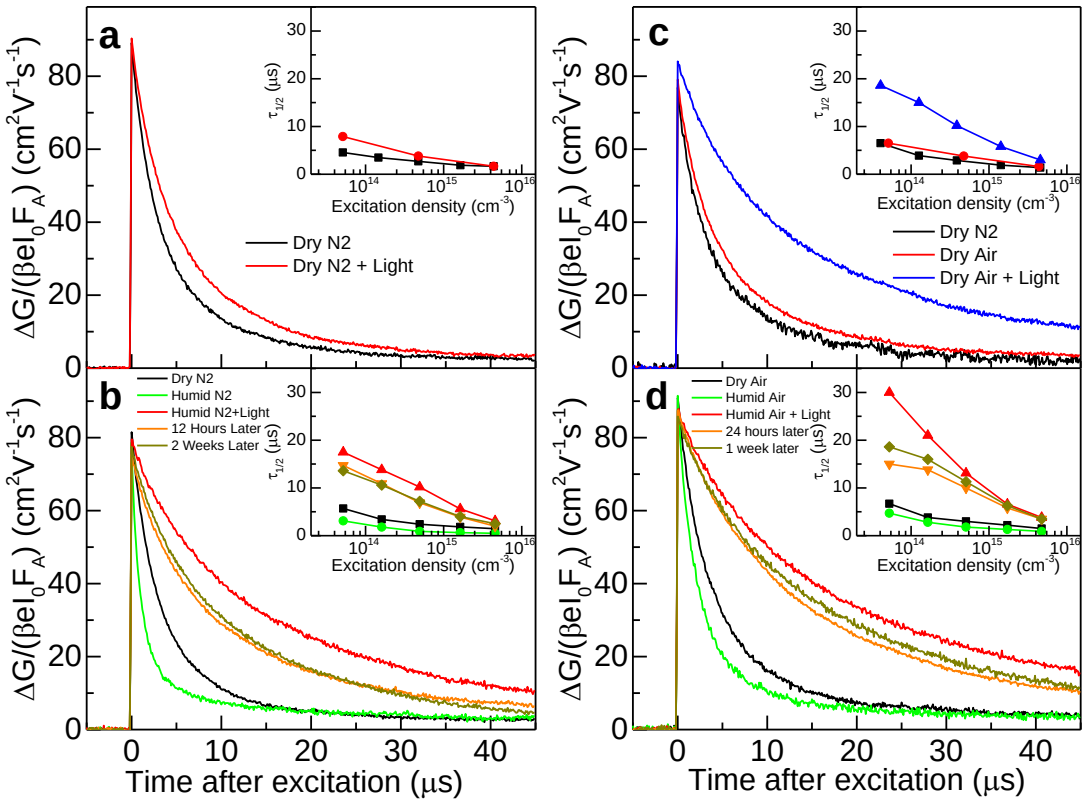

Figure A-11: (a) Photoconductance measurements for a $MAPbI_3$ film after storage in dry nitrogen and then after being subjected to light-soaking for 30 minutes in dry nitrogen under a white light LED source generating a similar photon flux to AM1.5 sunlight. The TRMC decays were taken by photo-exciting the samples in dry N_2 with pulsed illumination at 500 nm and an excitation density of $4.75 \times 10^{14} \mathrm{cm}^{-3}$. The inset shows the half lifetimes of the corresponding decays at different excitation densities (other decays not shown here). The other panels show similar measurements but under the stated atmosphere and conditions, i.e. (b) humid nitrogen (40% relative humidity) (excitation density of $4.93 \times 10^{14} \mathrm{cm}^{-3}$), (c) dry air (excitation density of $3.87 \times 10^{14} \mathrm{cm}^{-3}$) and (d) humid air (40% relative humidity) (excitation density of $5.07 \times 10^{14} \mathrm{cm}^{-3}$). Panels b and d also show the decays taken after storing the same sample in a nitrogen-filled glove box for various times after treatment.

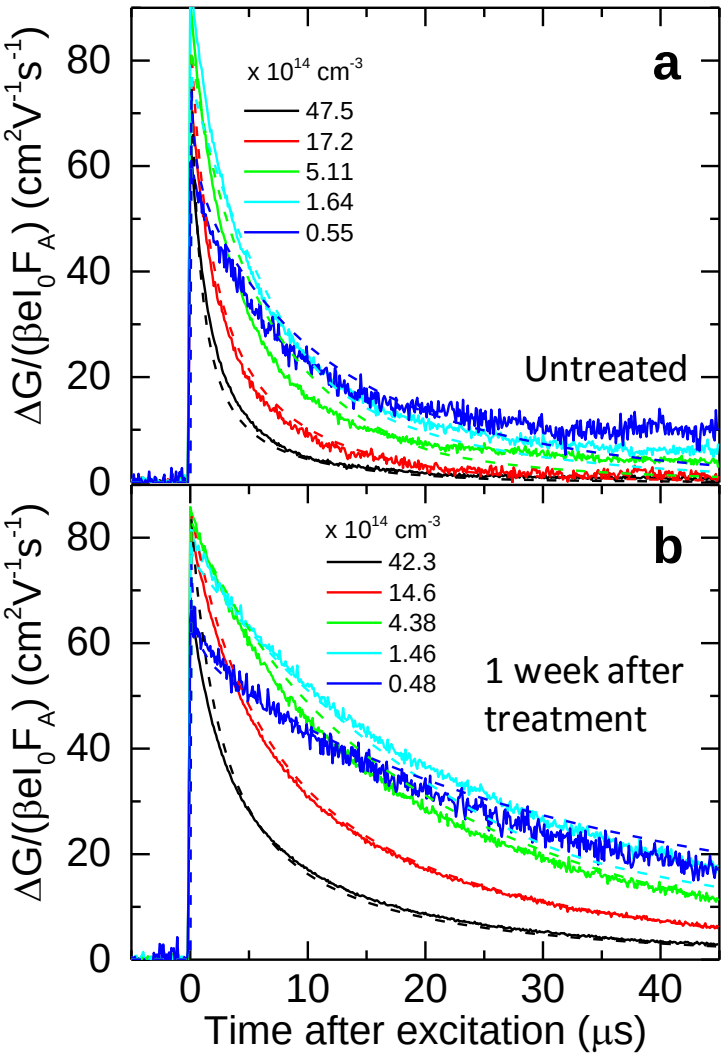

Figure A-12: Excitation-dependent TRMC decays of the (a) untreated samples and (b) samples 1 week after treatment (with storage in a nitrogen-glove box in between), with the initial charge excitation density (pulsed illumination at 500 nm) as shown in the legends. Dashed lines are fits to the data using the trap model described in Chapter 2. The corresponding data for the freshly-treated sample are shown in Figure 2-2b

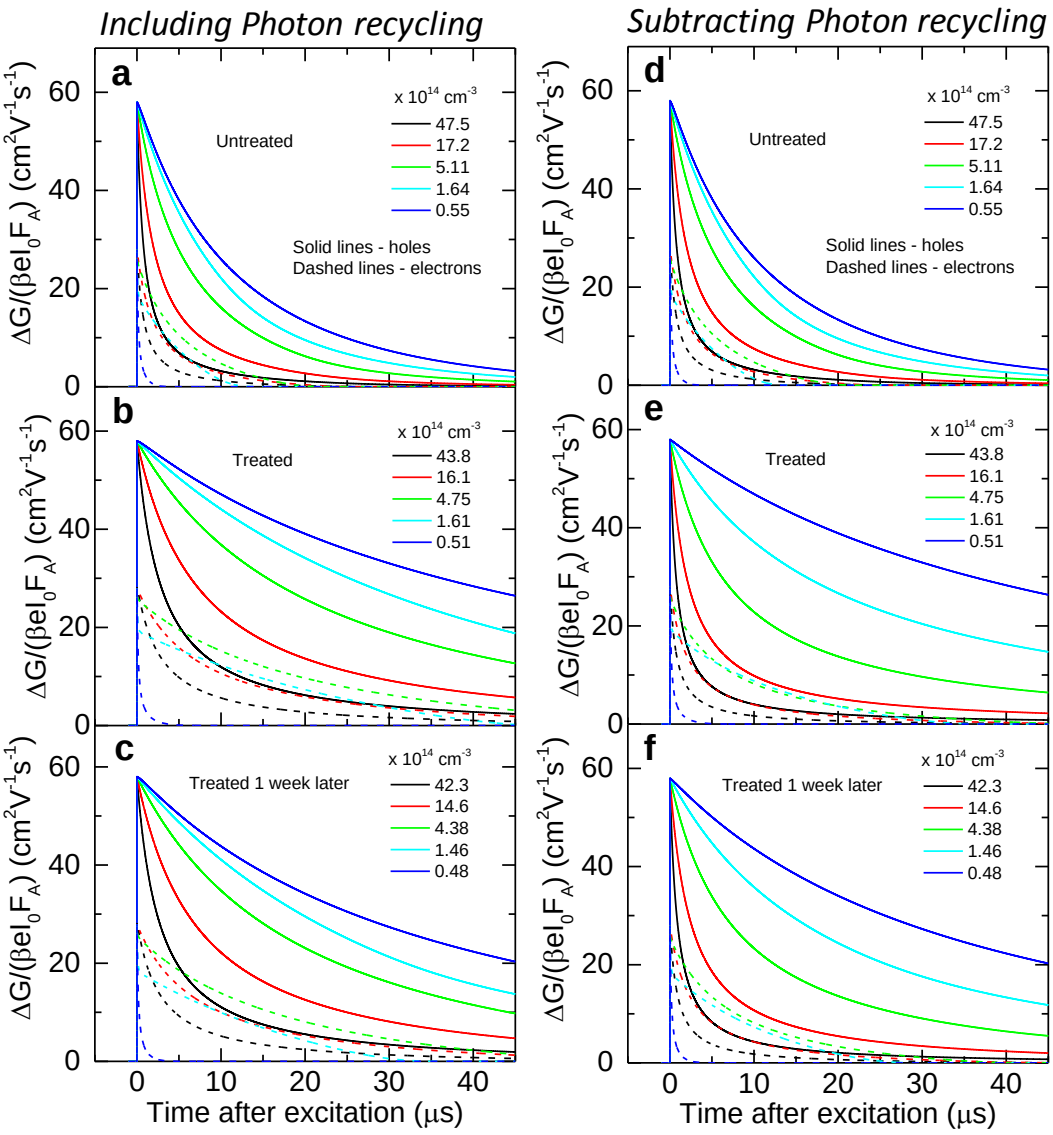

Figure A-13: The effective TRMC decay curves for each stated treatment for electrons (dashed lines) and holes (solid lines) decoupled using the rate equations in the trapping model incorporating electron traps N_t [7] (Scheme A-1) when including photon recycling ($k_2^{eff} = \eta_{esc} k_R + k_n$) (a-c) and when subtracting off the effects of photon recycling ($k_2^{int} = k_R + k_n$) (d-f).

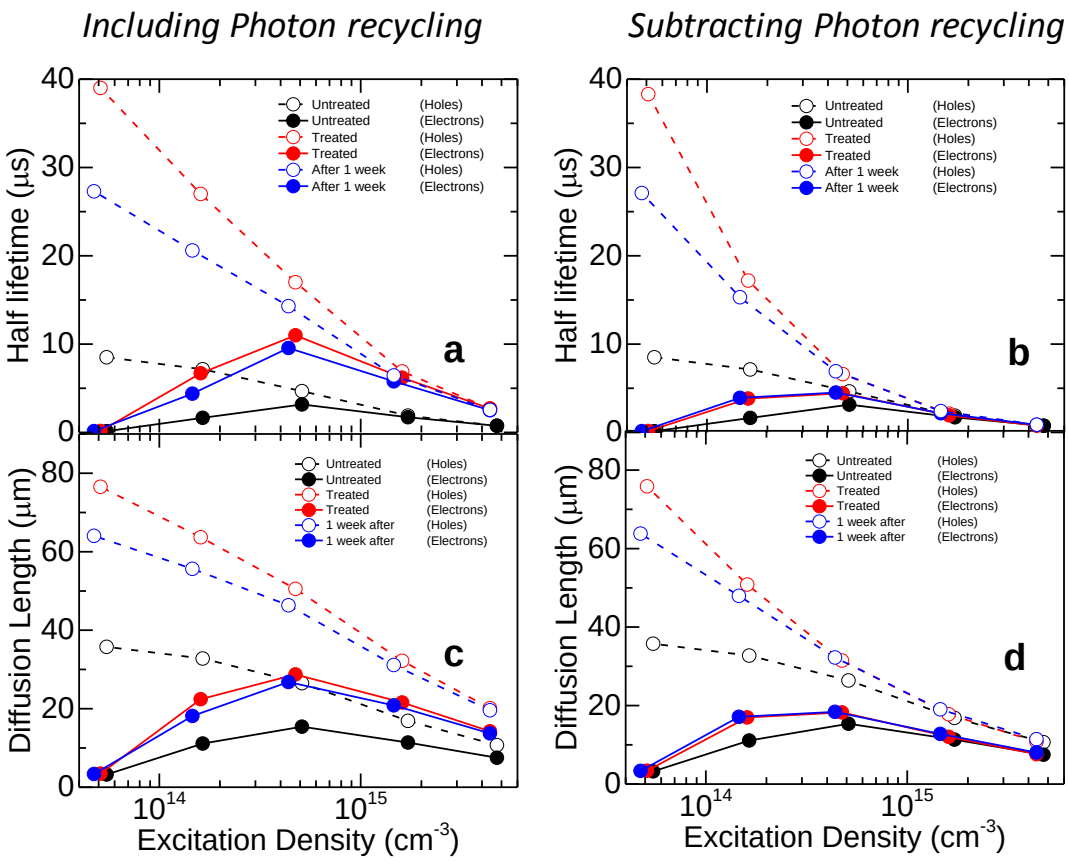

Figure A-14: Half lifetime of the electron and holes extracted from the decays in Figure A-13a-c with photon recycling (a) and Figure A-13d-f without photon recycling (b). We use these lifetimes to calculate the resulting diffusion length of each carrier using $L_D = \sqrt{k_B T \mu \tau_{1/2}/e}$, where k_B is the Boltzmann constant, T the temperature, e the electron charge and μ the mobility extracted from the photo-conductance measurements. The diffusion lengths are shown with (c) and without photon recycling (d). The diffusion lengths in the former case are interpreted as the cumulative diffusion length of a charge carrier including photon recycling events (but not including distance travelled by photons until reabsorption), while the latter is interpreted as the diffusion length of a charge carrier from initial excitation to first recombination event.

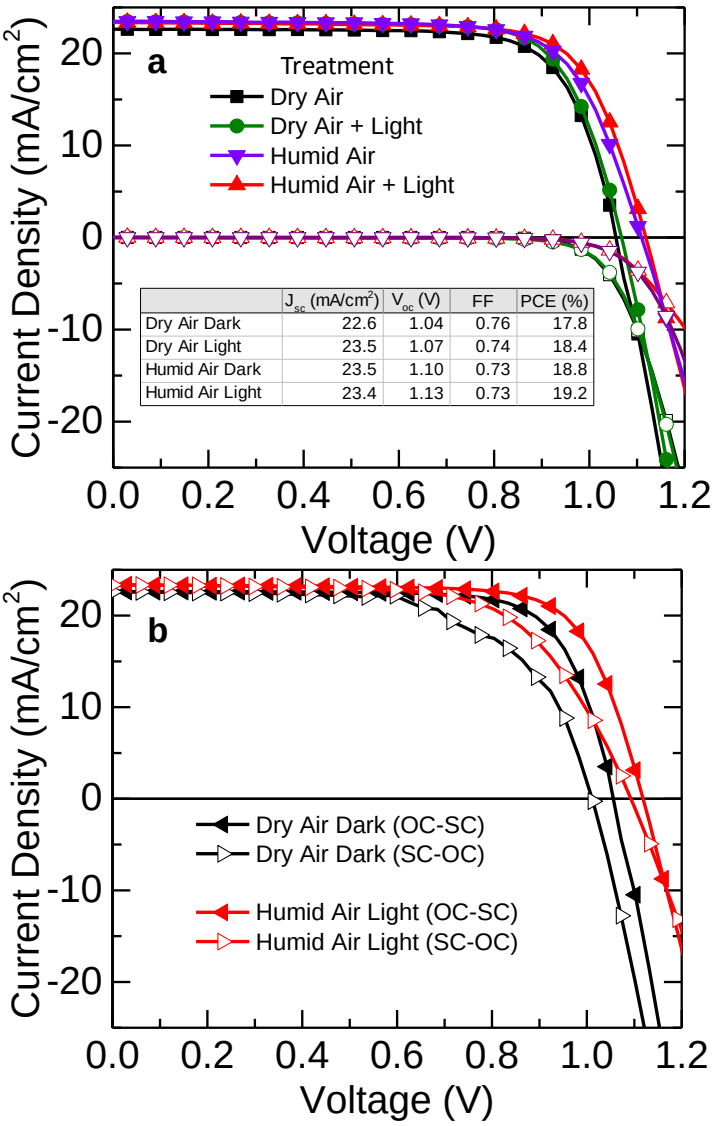

	J_{sc} (mA/cm^2)	V_{oc} (V)	FF	PCE (%)
Dry Air Dark	22.6	1.04	0.76	17.8
Dry Air Light	23.5	1.07	0.74	18.4
Humid Air Dark	23.5	1.10	0.73	18.8
Humid Air Light	23.4	1.13	0.73	19.2

Figure A-15: (a) Light and dark J-V curves of champion devices for the devices containing acetonitrile-based films stored in dry air, humid air (45% relative humidity), and light-soaked under dry air and humid air for 20 minutes with a white light LED array with an intensity similar to simulated sunlight. Device measurements were taken under AM1.5 100mW/cm^2 simulated sunlight and the presented scans were measured scanning from 1.4 V to 0 V (open-circuit to short-circuit, OC-SC). The comparison of the curves scanning from OC-SC and then from SC-OC are presented in (b), showing that there is some hysteresis in the devices under these scan conditions but this effect is reduced for the treated sample.

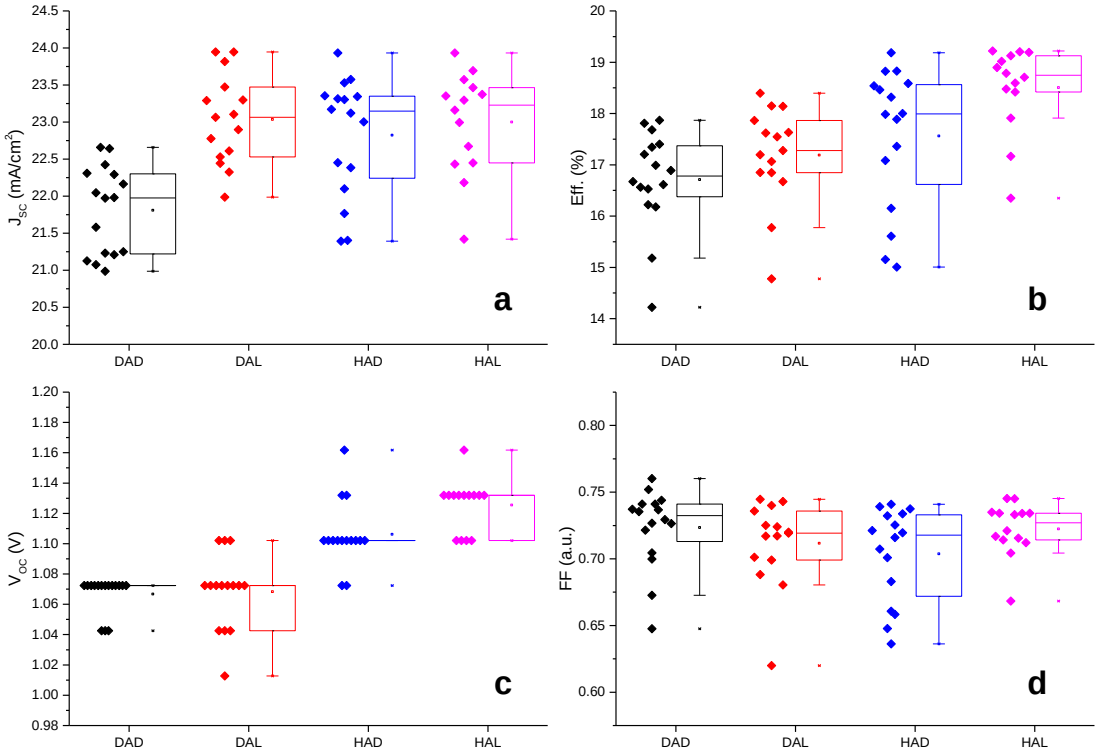

Figure A-16: (a-d) Device performance statistics for devices containing acetonitrile-based films stored in dry air in the dark (DAD), light-soaked in dry air (DAL), stored in humid air (45% relative humidity) in the dark (HAD) and light-soaked under humid air (45% relative humidity) (HAL). The light-soaking treatments were performed in the stated conditions by illuminating with a white-light LED array with an intensity similar to simulated sunlight for 20 minutes. Device measurements were taken under AM1.5 100mW/cm^2 simulated sunlight.

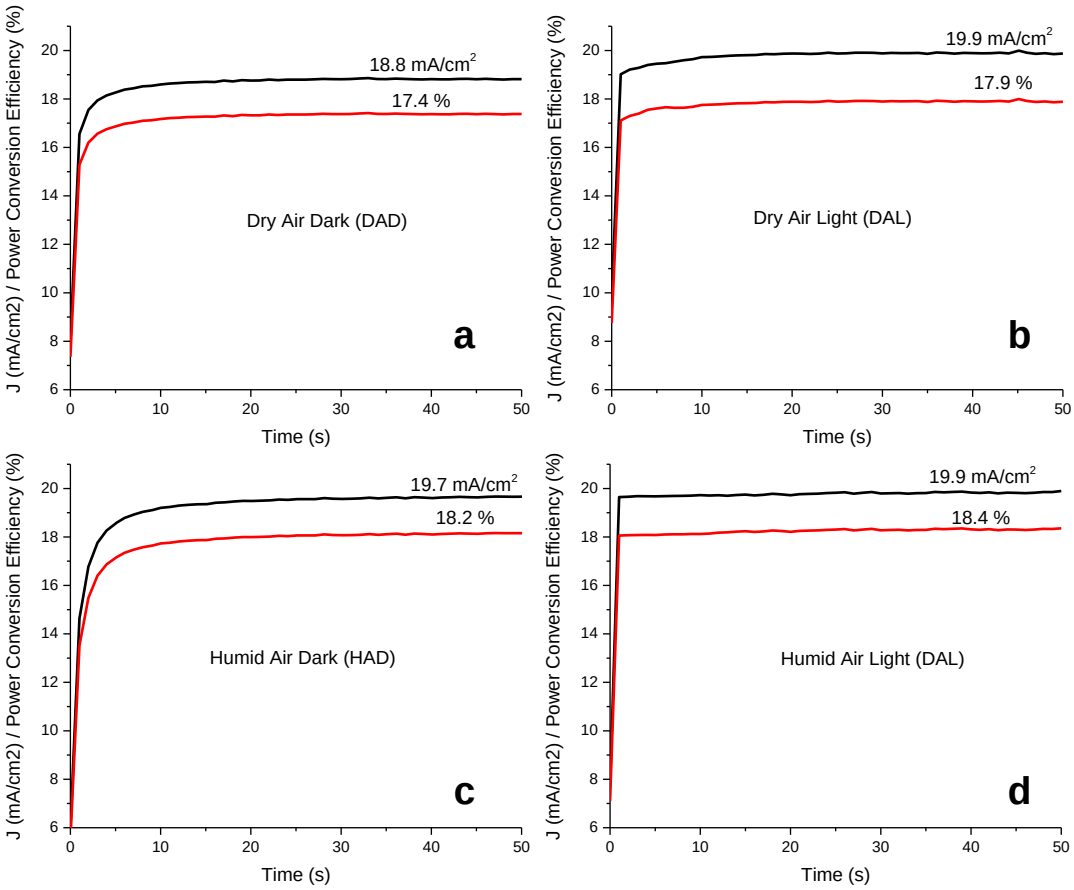

Figure A-17: Stabilized maximum power output for devices containing acetonitrile-based films stored in (a) dry air in the dark (DAD), (b) light-soaked in dry air (DAL), (c) stored in humid air (45% relative humidity) in the dark (HAD) and (d) light-soaked under humid air (45% relative humidity). The light soaking treatments were performed in the stated conditions by illuminating the half-constructed devices with a white light LED array with an intensity similar to simulated sunlight for 20 minutes. The measurements were taken by holding at the maximum power point voltage and measuring current under AM1.5 100mW/cm^2 simulated sunlight.

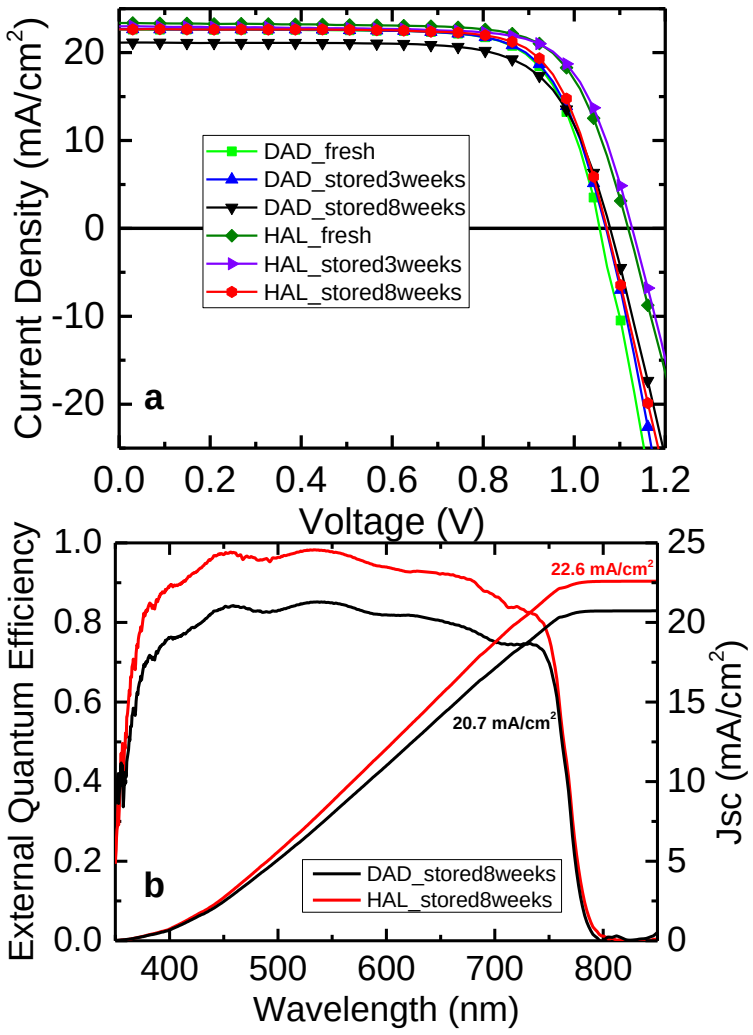

Figure A-18: (a) Light and dark J-V curves of champion devices for the devices containing acetonitrile-based films stored in dry air in the dark (DAD) and light-soaked in humid air (45% relative humidity) for 20 minutes with a white light LED array with an intensity similar to simulated sunlight (HAL). The measurements were taken fresh after the treatments and then after storage in a nitrogen-filled glove box for 3 weeks and 8 weeks. Device measurements were taken under AM1.5 100mW/cm^2 simulated sunlight. (b) External quantum efficiency (EQE) measurements on the devices stored for 8 weeks showing the integrated currents match those obtained from the current-voltage curves.

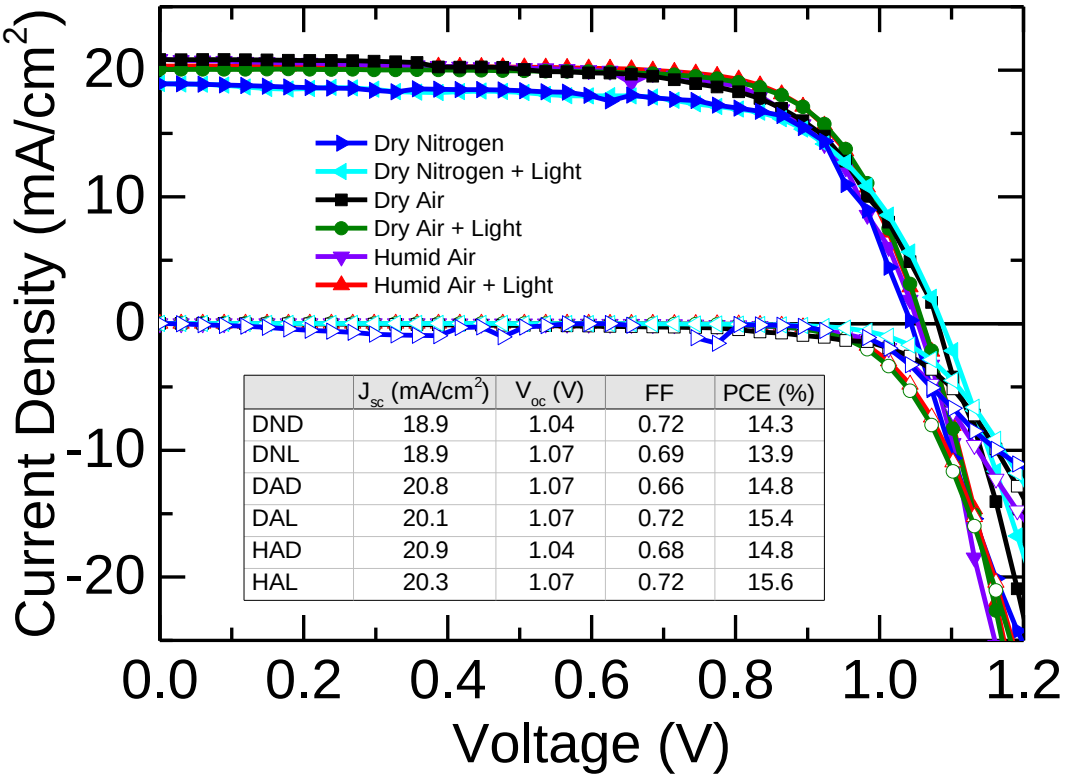

	J_{sc} (mA/cm^2)	V_{oc} (V)	FF	PCE (%)
DND	18.9	1.04	0.72	14.3
DNL	18.9	1.07	0.69	13.9
DAD	20.8	1.07	0.66	14.8
DAL	20.1	1.07	0.72	15.4
HAD	20.9	1.04	0.68	14.8
HAL	20.3	1.07	0.72	15.6

Figure A-19: Light and dark J-V curves of champion devices for the devices containing acetate/HPA-based films stored in dry nitrogen (DND), dry air (DAD), humid air (45% relative humidity, HAD), and light-soaked under dry nitrogen (DNL), dry air (DAL) and humid air (HAL) for 20 minutes with a white light LED array with an intensity similar to simulated sunlight. Device measurements were taken under AM1.5 100mW/cm^2 simulated sunlight.

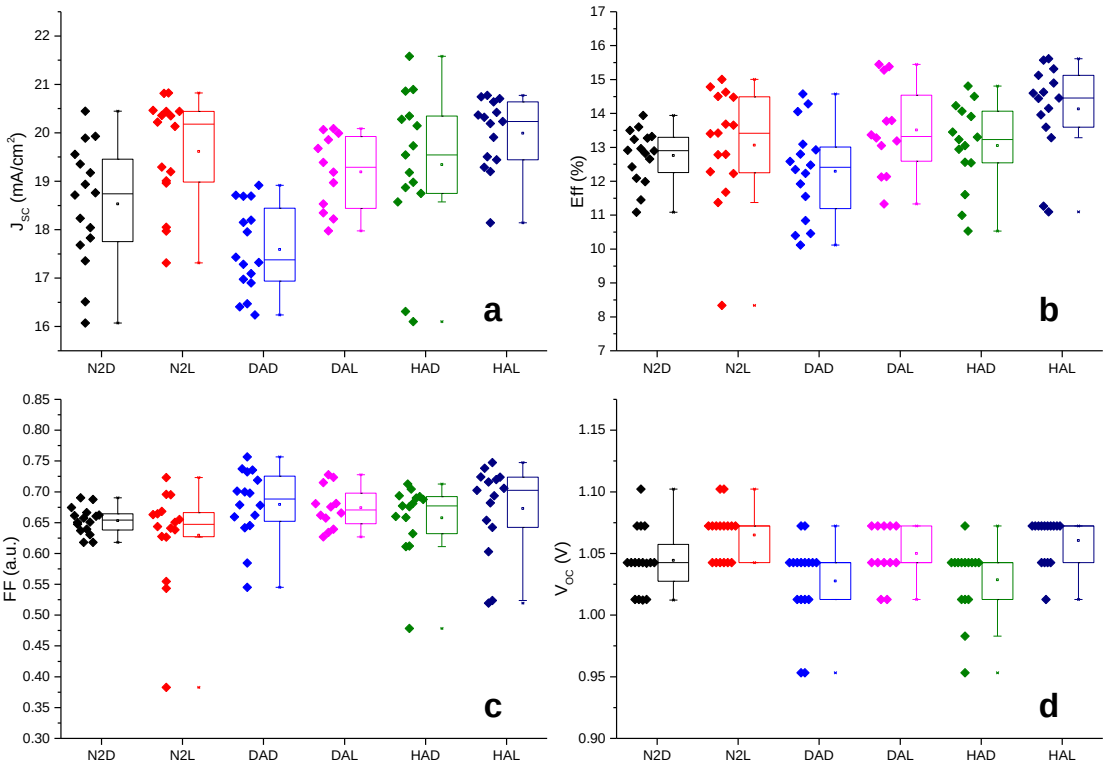

Figure A-20: L(a-d) Device performance statistics for devices containing acetate-based films stored in dry nitrogen in the dark (N2D), light-soaked in dry nitrogen (N2L), dry air in the dark (DAD), light-soaked in dry air (DAL), stored in humid air (45% relative humidity) in the dark (HAD) and light-soaked under humid air (45% relative humidity) (HAL). The light soaking treatments were performed in the stated conditions by illuminating with a white light LED array with an intensity similar to simulated sunlight for 20 minutes. Device measurements were taken under AM1.5 100mW/cm^2 simulated sunlight.

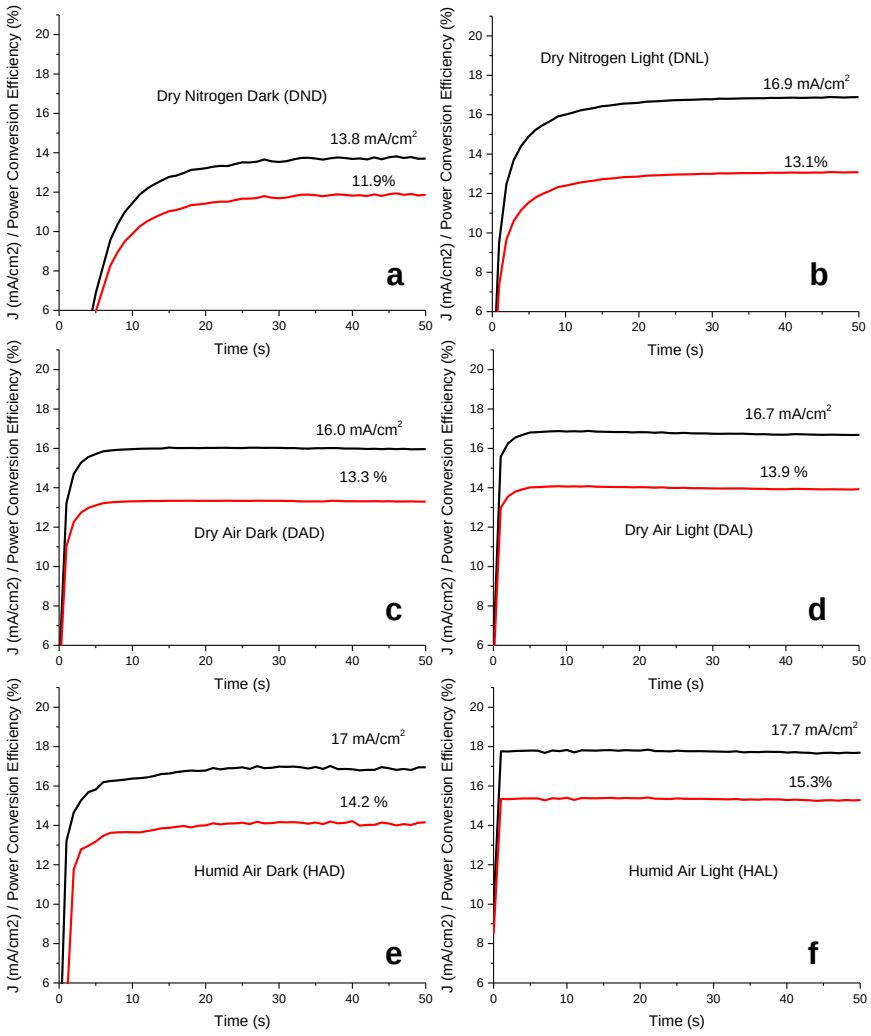

Figure A-21: Stabilized maximum power output for devices containing acetate/HPA-based films stored in (a) dry nitrogen in the dark (DND), (b) light-soaked in dry nitrogen (DNL), (c) dry air in the dark (DAD), (d) light-soaked in dry air (DAL), (e) stored in humid air (45% relative humidity) in the dark (HAD) and (f) light-soaked under humid air (45% relative humidity). The light soaking treatments were performed in the stated conditions by illuminating the half-constructed devices with a white light LED array with an intensity similar to simulated sunlight for 20 minutes. These measurements were taken by holding the full devices at the maximum power point voltage and measuring current under AM1.5 100mW/cm^2 simulated sunlight.

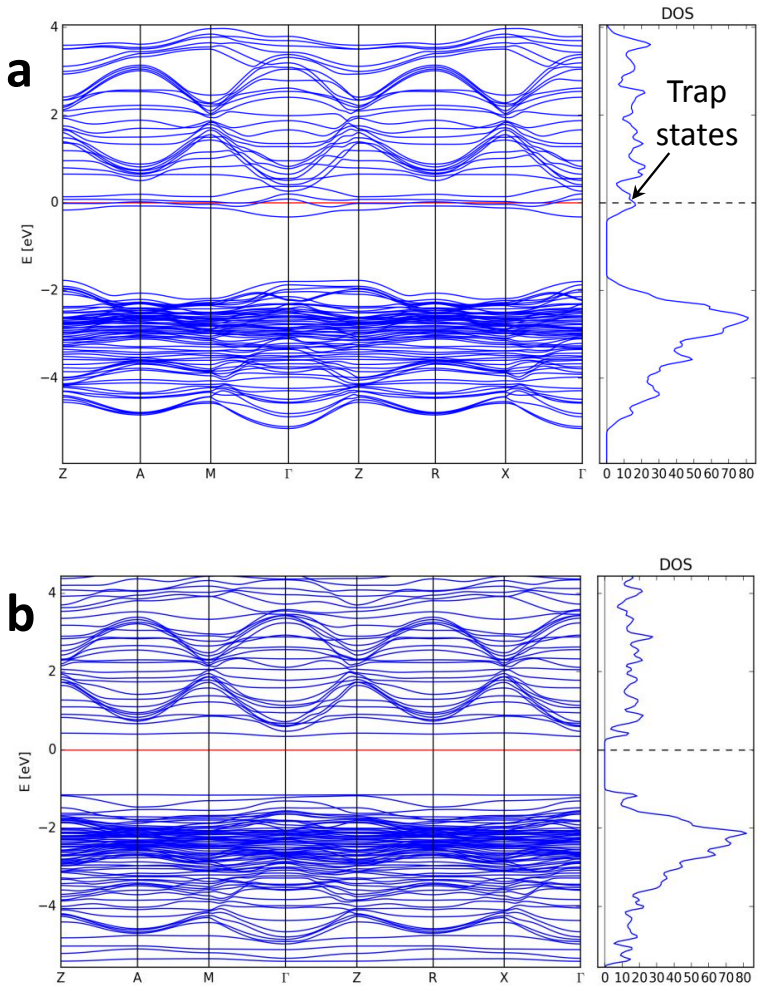

Figure A-22: Electronic structure of $MAPbI_3$ (001) surface calculated by density functional theory. (a) band structure and D.O.S. for (001) surface containing an iodine vacancy occupied by a photogenerated electron showing shallow trap states below the conduction band. (b) band structure and D.O.S. for (001) surface containing an iodine vacancy occupied by a photogenerated electron into which an O_2 molecule is chemisorbed and reduced to form a superoxide species O_2^-. The sub gap shallow trap states indicated in (a) are now significantly reduced in density.

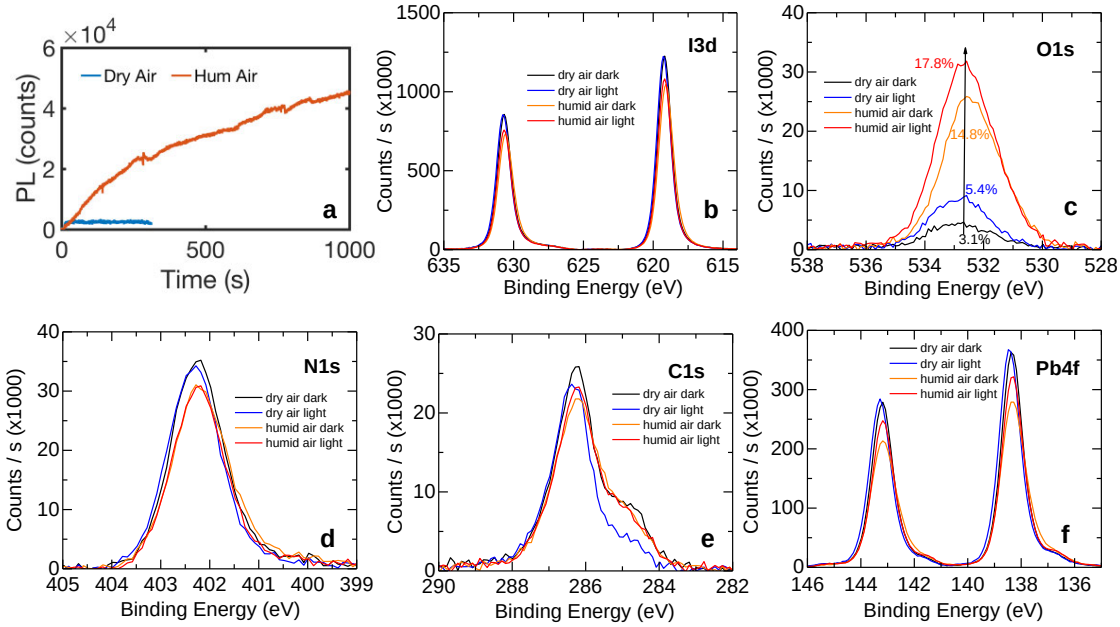

Figure A-23: (a) PL measurements over time under illumination with a 532-nm laser at an excitation intensity equivalent to ∼2 sun (∼150 mW/cm^2) in dry air (blue) and humidified air (red). (b) X-Ray Photoemission Spectroscopy (XPS) measurements of the (b) I3d, (b) O1s, (d) N1s, (e) C1s, (f) Pb4f signatures in the regions of the sample light-soaked (light) and regions of the same films without light-soaking (dark). The atomic percent of oxygen species is labelled for each treatment. We find an increase in the O content after light-soaking in dry air, a substantial further increase in O when bringing into humid air, and a further increase again after light-soaking in humid air for 1000 seconds. We note that these O1s peaks are broad and likely consist of a range of species including, among others, superoxides and hydroxides. We do not observe dramatic changes in the other species, nor in the peak positions of each species.

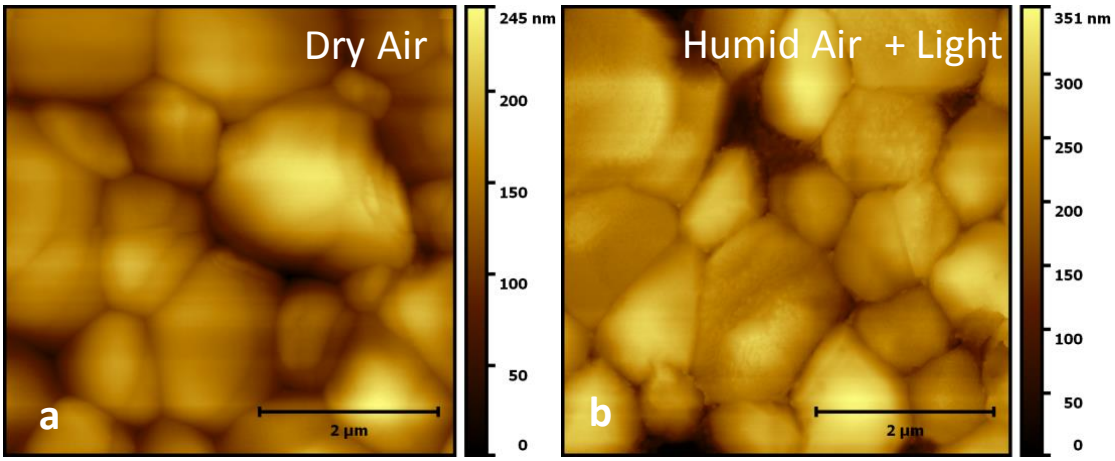

Figure A-24: Atomic force microscopy (AFM) images of the films for (a) a film stored in dry air without any light and (b) a region illuminated in humid air for 10 minutes with a 532-nm laser at an excitation intensity equivalent to ∼2 sun (∼150 mW/cm^2). The root-mean-square (RMS) variations of the surface over larger scan areas excluding pin-holes is 40.2 ± 4.0 nm (dry air) and 44.5 ± 4.5 nm (humid air + light). This represents a negligible change in roughness though potentially a very slight texturing after exposure to humidity and light. We note that this increase could not explain the increased external PLQE measurements we observe.

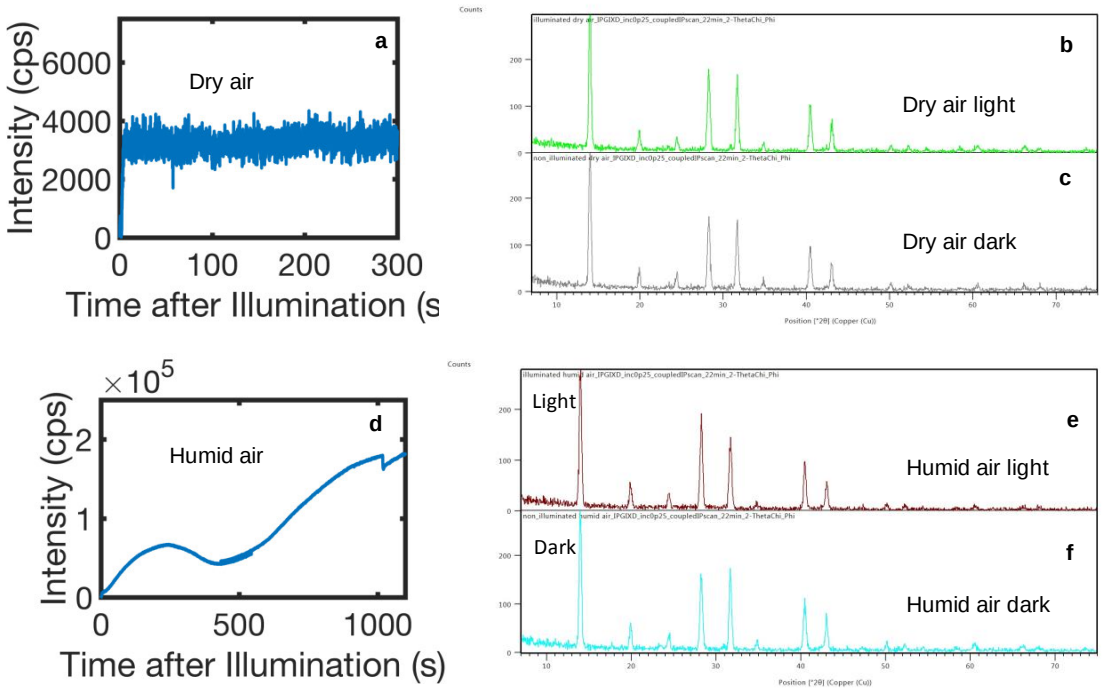

Figure A-25: (a) PL measurements over time under illumination with a 532-nm laser at an excitation intensity equivalent to ∼2 sun (∼150 mW/cm^2) in dry air. (b-c) In-plane grazing incidence X-Ray Diffraction (IP-GIXD) for the (b) light-soaked region of a and (c) another region of the same sample without light-soaking (dark). (d-f) The same series but with humid air conditions. We do not find any significant changes after treatment in atmosphere or light for the short soaking periods in which we see the PL enhancements, suggesting we are not substantially perturbing the surface crystallinity or creating crystalline surface material. Significantly, no PbI2 is detected (expected ∼ 12.5°).

A.3 Sensitivity of reported values

The internal PLQE peak value of 89% (Fig. 2-1c) is calculated from the measured external PLQE value by assuming a (conservatively high) estimate for the escape probability of $\eta_{esc} = 12.7\%$. This is assuming the same properties of the films used by Richter et al., which is a fair assumption given that the material composition, interfaces and film thickness are similar [68]. However, if we allowed the escape probability to even reach 20% (extremely conservative estimate), we find the internal PLQE still plateaus at ∼ 84%.

Table A.1: Relevant parameters extracted from the fits to the data with the kinetic model for the untreated (Figure A-12a) and treated (Fig. 2-2b) films, and 1 week after treatment (Figure A-12b).

Parameter	Untreated (dry air)	Treated (humid air + light)	Treated (1 week later)
k_T (cm^3s^{-1})	1.2×10^{-7}	1.2×10^{-7}	1.2×10^{-7}
k_2^{eff} (cm^3s^{-1})	26.0×10^{-11}	7.60×10^{-11}	8.50×10^{-11}
k_D (cm^3s^{-1})	8.00×10^{-10}	3.20×10^{-10}	4.00×10^{-10}
N_t (cm^{-3})	6.00×10^{13}	5.50×10^{13}	5.50×10^{13}
p_0 (cm^{-3})	6.50×10^{13}	2.00×10^{13}	3.00×10^{13}
Internal PLQE $\eta(\%)$	1	84	78
Effective k_R (cm^3s^{-1})	0.26×10^{-11}	23.9×10^{-11}	20.8×10^{-11}
Effective k_n (cm^3s^{-1})	26.0×10^{-11}	4.56×10^{-11}	5.86×10^{-11}
$k_2^{int} = k_n + k_R$ (cm^3s^{-1})	26.2×10^{-11}	28.5×10^{-11}	26.6×10^{-11}

The kinetic parameters (listed in Table A.1) are extracted from global fits to the data with the model shown in Scheme A-1 and described above. To keep the five fitting traces overlapping the corresponding experimental traces, there is not a large amount of freedom and the rate constants (e.g. k_2^{eff}) and N_t values can only be changed by $\pm 3\%$. We have further constraints on the parameters in global fits when considering that N_t corresponds approximately to the excitation density at which recombination changes from mono- to bi-molecular, and the resulting long-lived recombination of the untrapped holes at low fluence gives an approximation for the trap recombination rate k_D.

We also note that TRMC gives a measure of the intra-grain charge transport properties and will therefore yield values on the higher end of mobility and lifetime distributions in a polycrystalline sample. The main structural error in the magnitude of the mobility values originate from the uncertainty in the K factor shown in Equation 2.3. The sample-to-sample variation in measured mobility is $\sim 5\%$ and we did not find differences in mobility in our films before or after treatments within this error. The values of the mobility extracted from TRMC are consistent with values extracted from THz measurements [39, 40, 42].

A.4 Extracting relative fractions of k_R and k_n

For the intensity regime in which the deep traps states are predominantly filled, η is determined only from the relative fractions of recombination occurring through k_R and k_n given by:

$$\eta = \frac{k_R}{k_R + k_n} \tag{A.1}$$

We can therefore use Eq. 2.1 and Eq. A.1 and the measured PLQE with intensities at which deep traps are filled (Figure A-2) to extract effective rates of k_R and k_n owing to the changing fraction of recombination occurring through each pathway (see Table A.1). We find that the treatments increase the effective radiative component k_R by two orders of magnitude from 0.26×10^{-11} $\mathrm{cm^3 s^{-1}}$ to 23.9×10^{-11} $\mathrm{cm^3 s^{-1}}$, while the effective non-radiative component kn decreases by an order of magnitude from 26.0×10^{-11} $\mathrm{cm^3 s^{-1}}$ to 4.56×10^{-11} $\mathrm{cm^3 s^{-1}}$. The internal recombination rate, given by $k_2^{int} = k_R + k_n$, is almost unchanged from the untreated (26.2×10^{-11} $\mathrm{cm^3 s^{-1}}$) to treated (28.5×10^{-11} $\mathrm{cm^3 s^{-1}}$) samples.

We consider these extracted rate constants k_R and k_n as effective rate constants given by $k_R = f_R k_R^{intrinsic}$ and $k_n = (1 - f_R) k_n^{intrinsic}$, where $k_R^{intrinsic}$ and $k_n^{intrinsic}$ are the intrinsic rate constants for the material that do not change with treatment, and f_R is the fraction recombining through the radiative pathway, which does change with treatment. In the case that the radiative fractions fR are given by the internal PLQE, we can approximate the intrinsic recombination rates as $k_R^{intrinsic} \approx k_n^{intrinsic} \approx 2 \times 10^{-11}$ $\mathrm{cm^3 s^{-1}}$. These comparable rates are consistent with the shallow state model in which charge carriers in shallow states (non-radiative) or in the conduction band (radiative) have equal rates of their respective recombination pathways, but the fraction of each pathway is dictated by the number of shallow states. We note that further work would be required to confirm whether $k_n^{intrinsic}$ is indeed an intrinsic material property or also changing with treatment.

A.5 Surface recombination velocity

For the samples in the work, the diffusion length (microns) is sufficiently long compared to the sample thickness $L \sim 250$nm. Thus, the decay of carrier density is simply the sum of a bulk and a surface term such that:

$$\frac{1}{\tau} = \frac{1}{\tau_B} + \frac{2S}{L} \tag{A.2}$$

where τ is the lifetime, τ_B is the bulk carrier lifetime and S is the surface recombination velocity (SRV)[92]. We expect the surface term (second term in Eq. A.2) will dominate recombination with such thin films in which the defect densities are likely largest at the surfaces, thus giving the approximation:

$$S \approx \frac{L}{2\tau} \tag{A.3}$$

At low fluence in which many electrons are trapped, the carrier density decay is dominated by holes ($\tau_{1/2} = 32\mu s$) and we find the resulting SRV for holes is $S \approx 0.4$ cm/s. We note that we obtain very similar values when using other approximations for SRV in thin polycrystalline films[29, 96]. At this fluence, the corresponding electron lifetime (i.e. trapping time) is ∼150 ns (Figure A-14), which leads to SRV for electrons of $S \approx 80$ cm/s. This value is still an order of magnitude lower than other reports for polycrystalline perovskite films [96]. Further work would be required to decouple the SRV values at higher fluence in the presence of the shallow states.

A.6 Ab-initio calculations

DFT calculations were performed using the numeric atom-centred basis set all-electron code FHI-AIMS [8, 67]. Light basis sets were used with tier 2 basis functions for C, N, H and O. Electronic exchange and correlation were modelled with the semi-local PBE exchange-correlation functional [64]. A gamma point offset grid at a density

of 0.04 Å^{-1} was used for k-point sampling. For the treatment of spin orbit coupling we used an atomic zeroth-order regular approximation (ZORA) [8]. Van der Waals forces were accounted for by applying a Tkatchenko-Sheffler electrodynamic screening scheme [83].

Molecules were adsorbed onto an 8 layer (010) surface slab of tetragonal MAPbI3 containing 96 atoms with a vacuum gap of 30 Å. Charged surfaces were compensated using the virtual crystal approximation [69]. We tested MAI and PbI_2 terminated surfaces in both defect free and iodine vacancy containing configurations. In line with our previous work in the bulk we found that O_2 adsorption and reduction was most favourable on iodide vacancies. The overall reaction for this adsorption onto iodine vacancies can be represented by the following equation:

$$\text{MAPbI}_3\ (010) + \text{V}_\text{I}' + \text{O}_2 \rightarrow \text{MAPbI}_3\ (010) + \text{O}_2'$$

where, in Kroger-Vink notation, the term V_I' on the left represents a vacancy on an iodine site with a negative charge and the term O_2' on the right represents an oxygen molecule with a negative charge on an iodine site i.e. an adsorbed superoxide molecule. Structures were relaxed with convergence criteria of 10^{-4} eV/Å for forces, 10^{-5} electrons for the electron density and 10^{-7} eV for the total energy.

A.7 Surface characterization

X-ray photoelectron spectroscopy (XPS) measurements were collected using a Thermo Scientific K-Alpha X-Ray spectrophotometer. Peaks were fitted and analyzed using Thermo Avantage software. The baseline was calculated using Shirley's method and the data were corrected assuming atmosphere carbon contamination at 285 eV. A Gaussian mixture was used for peak fitting and surface composition and concentrations were calculated from the appropriate peak area. In-plane X-ray diffraction spectra of treated and untreated samples were collected in ambient air using Rigaku Smartlab with Cu Kα X-ray source (λ = 0.1542nm) in GIXRD geometry with a

grazing incidence angle of 0.25°.

Atomic force microscope (AFM) images of treated and untreated samples were collected using an Agilent 5500 microscope equipped with a high-resolution scanner. High-resolution images were obtained collecting 1024 pixel images at a rate ≤ 0.5 Hz in ambient environmental conditions. An uncoated Bruker AFM Antimony (n) doped Si probe ($k = 40$N/m, $f = 300$kHz) was used. Leveling of topographical images was performed using the Gwyddion software.

A.8 Device external quantum efficiency (EQE) measurements

The External Quantum Efficiency (EQE) was measured via Fourier-transform photocurrent spectroscopy[85]. This was carried out using the modulated beam of a Bruker Vertex 80v Fourier Transform Interferometer with a tungsten lamp source and a Stanford Research SR570 current preamplifier. Samples were calibrated to a Newport-calibrated reference silicon solar cell with a known external quantum efficiency. The perovskite solar cells were held at forward bias (1.4 V) for 5 seconds before measuring[74]. The solar cells were masked with a metal aperture to define an active area of 0.0925 cm^2.

Appendix B

Supplementary Information to Chapter 3

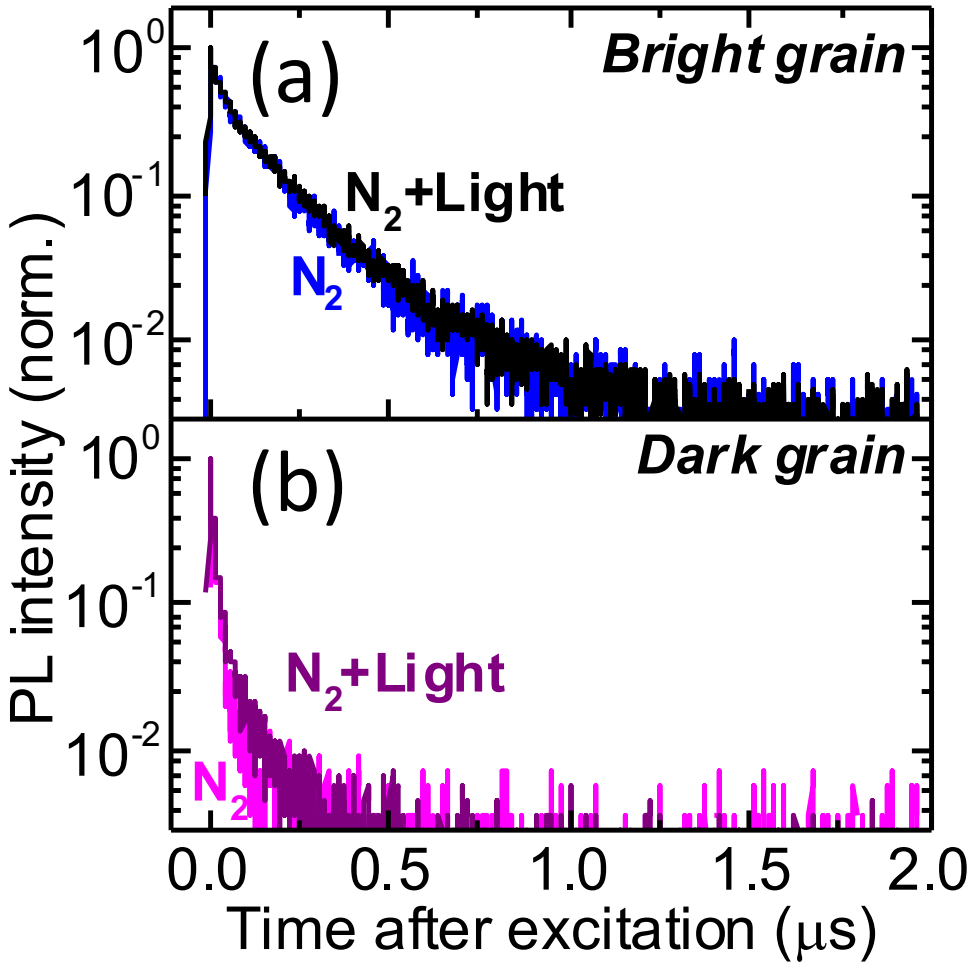

Figure B-1: PL decays from the same bright and dark grains shown in Figure 3-1a, before and after light soaking in dry nitrogen. Samples were photoexcited with a 405 nm laser with a repetition rate of 0.5 MHz and a fluence of $\sim$1 μJ/cm^2/pulse ($\sim$500 mW/cm^2), and this same laser was used for local light-soaking (total photon dose of $\sim$150 J/cm^2).

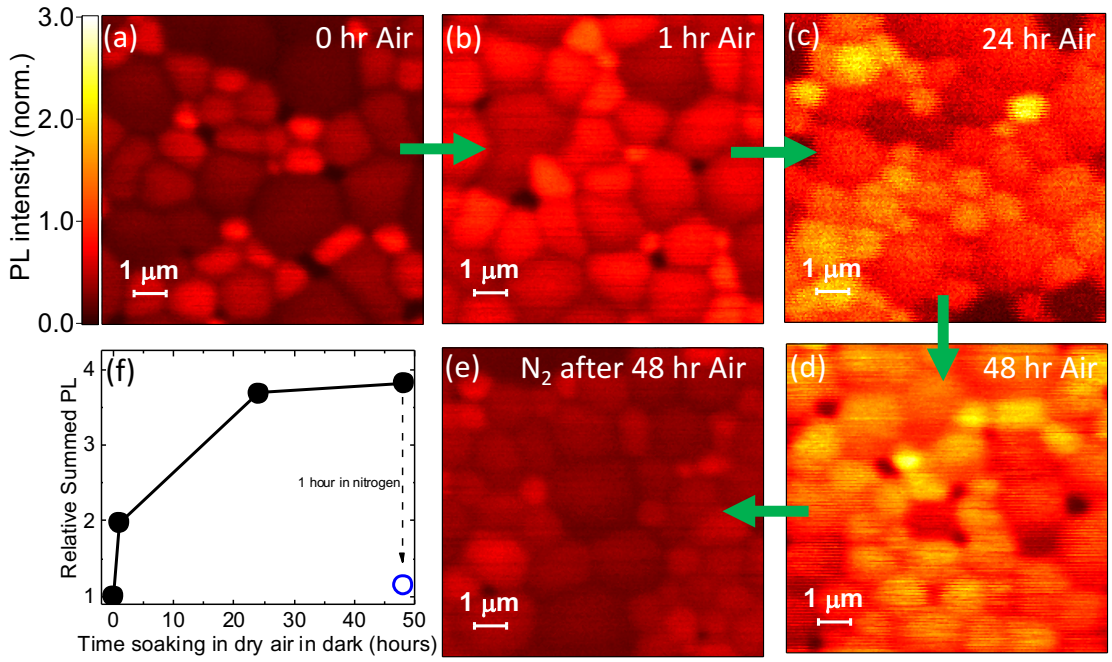

Figure B-2: Compressed air storage over time in the dark. Confocal PL map of $MAPbI_3$ films prepared in a nitrogen glove box and maps acquired (a) in dry nitrogen, and in dry air after (b) 1 hour, (c) 24 hours and (d) 48 hours in dry compressed air. (e) A film stored for 48 hours in dry air but then measured in dry nitrogen after 1 hour storage in dry nitrogen, suggesting the oxygen pre-soaking (loading) effects can be removed. The map intensities are given relative to the maximum value in (a), which is normalised to 1. Samples were photoexcited with a 405 nm laser with a repetition rate of 0.5 MHz and a fluence of $\sim$1 μJ/cm^2/pulse ($\sim$500 mW/cm^2). (f) Total summed intensity of each map relative to the summed intensity of (a), which is normalised to 1. The blue symbol corresponds to the map in (e).

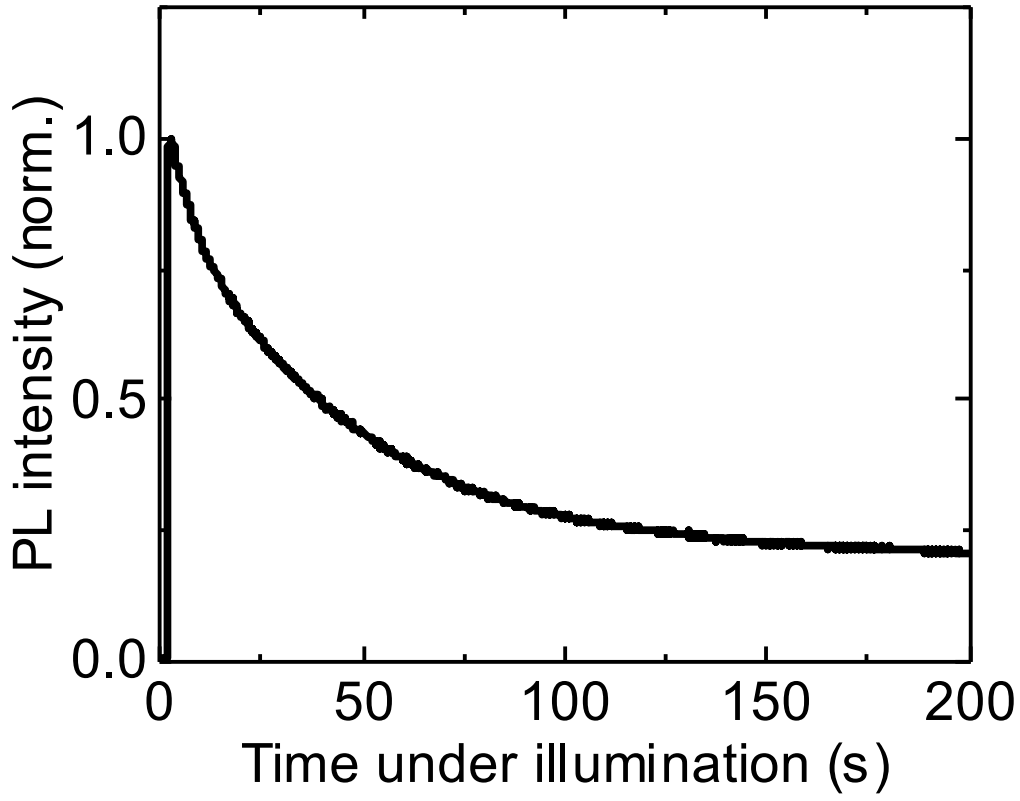

Figure B-3: PL from a $MAPbI_3$ film measured *in-vacuo* (pressure $< 10^{-4}$ mbar) under continuous illumination with a 532-nm laser with excitation density similar to solar illumination conditions ($\sim$2 sun, 150 mW/cm^2).

Table B.1: Adsorption energies of N_2, H_2O, and O_2 molecules on the (110) surface of $MAPbI_3$ in three possible charge states due to photoexcitation. Favourable surface sites are on the Pb^{2+} on the PbI_2-terminated surface and in an iodine vacancy on defect-rich PbI_2 surface terminations.

Adsorbate	Surface site	Charge state	Adsorbtion energy (eV)
N_2	Pb^{2+}	-1	-0.14
	Pb^{2+}	0	-0.15
	Pb^{2+}	+1	-0.13
	$V_I^{'}$	-1	-0.12
	$V_I^{\times}$	0	-0.14
	$V_I^{\bullet}$	+1	-0.15
H_2O	Pb^{2+}	-1	-0.47
	Pb^{2+}	0	-0.47
	Pb^{2+}	+1	-0.47
	$V_I^{'}$	-1	-0.66
	$V_I^{\times}$	0	-0.46
	$V_I^{\bullet}$	+1	-0.54
O_2	Pb^{2+}	-1	-1.32
	Pb^{2+}	0	-0.28
	Pb^{2+}	0	-0.61
	$V_I^{'}$	-1	-3.94
	$V_I^{\times}$	0	-2.48
	$V_I^{\bullet}$	+1	-0.72

Table B.2: Adsorption energies of N_2, H_2O, and O_2 molecules on the (001) surface of $MAPbI_3$ in three possible charge states due to photoexcitation. Favourable surface sites are on the Pb^{2+} on the PbI_2-terminated surface and in an iodine vacancy on defect-rich PbI_2 surface terminations.

Adsorbate	Surface site	Charge state	Adsorbtion energy (eV)
N_2	Pb^{2+}	-1	-0.12
	Pb^{2+}	0	-0.12
	Pb^{2+}	+1	-0.11
	$V_I^{'}$	-1	-0.16
	$V_I^{\times}$	0	-0.18
	$V_I^{\bullet}$	+1	-0.16
H_2O	Pb^{2+}	-1	-0.48
	Pb^{2+}	0	-0.47
	Pb^{2+}	+1	-0.44
	$V_I^{'}$	-1	-0.52
	$V_I^{\times}$	0	-0.52
	$V_I^{\bullet}$	+1	-0.52
O_2	Pb^{2+}	-1	-1.09
	Pb^{2+}	0	-0.27
	Pb^{2+}	0	-0.57
	$V_I^{'}$	-1	-3.79
	$V_I^{\times}$	0	-2.21
	$V_I^{\bullet}$	+1	-0.57

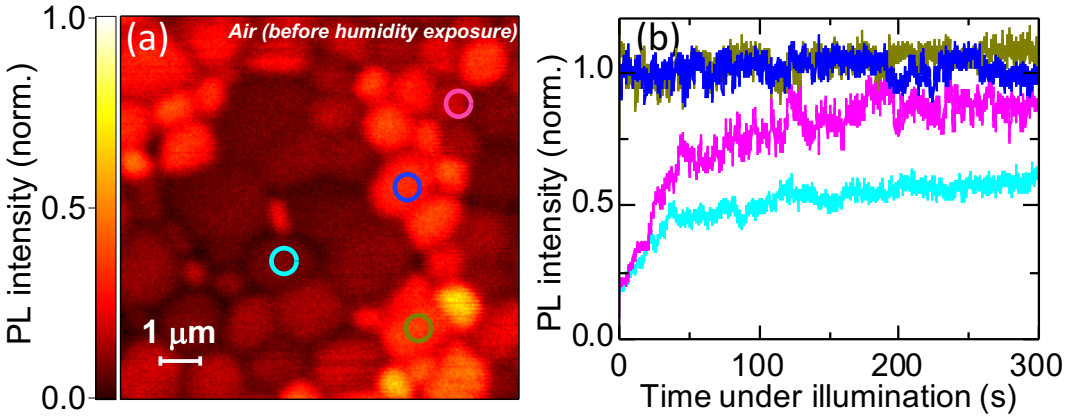

Figure B-4: (a) Confocal PL map of a $MAPbI_3$ perovskite film in dry air normalised to the maximum intensity. (b) Monitoring the emission intensity (count rate) from various bright and dark grains denoted in (a) over time under illumination in dry air. The PL intensity for each trace over time is given relative to the starting value for the highest initial intensity (blue grain), which is normalised to 1. These correspond to the same grains as shown in Figure 3-3a and b but before the exposure to humidity (cf. Figure 3-2). Samples were photoexcited with a 405 nm laser with a repetition rate of 0.5 MHz and a fluence of $\sim$1 μJ/cm^2/pulse ($\sim$500 mW/cm^2), and this same laser was used for local light-soaking (total photon dose of $\sim$150 J/cm^2).

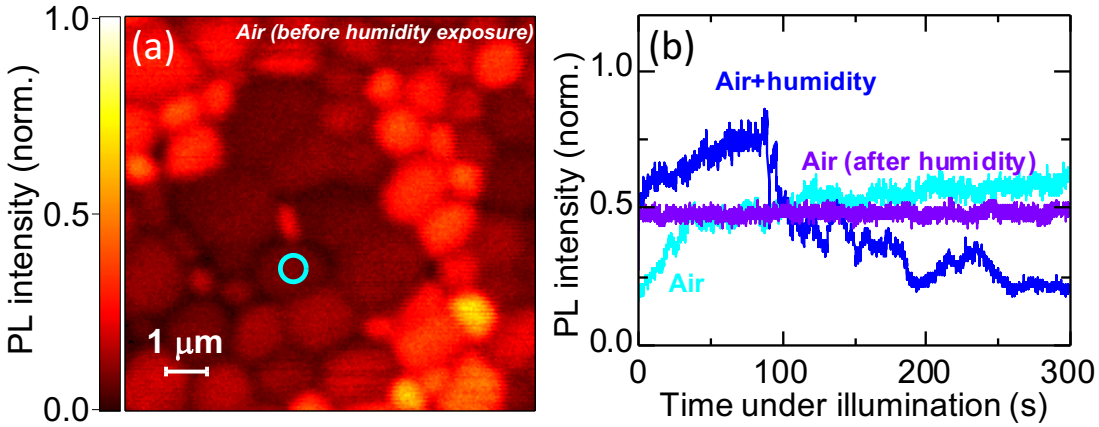

Figure B-5: (a) Confocal PL map of a $MAPbI_3$ perovskite film in dry air normalised to the maximum intensity. (b) Monitoring the emission intensity (count rate) from the same grain while light-soaking in dry air (cyan), humid air (blue) and after returning the sample to dry air (purple). This grain is unstable while light-soaking in humid air but retains its emission stability after returning to dry air. The emission intensities were normalised to the same initial value as the dry air measurement in Fig. 3-3c. Samples were photoexcited with a 405 nm laser with a repetition rate of 0.5 MHz and a fluence of $\sim$1 μJ/cm^2/pulse ($\sim$500 mW/cm^2), and this same laser was used for local light-soaking (total photon dose of $\sim$150 J/cm^2).

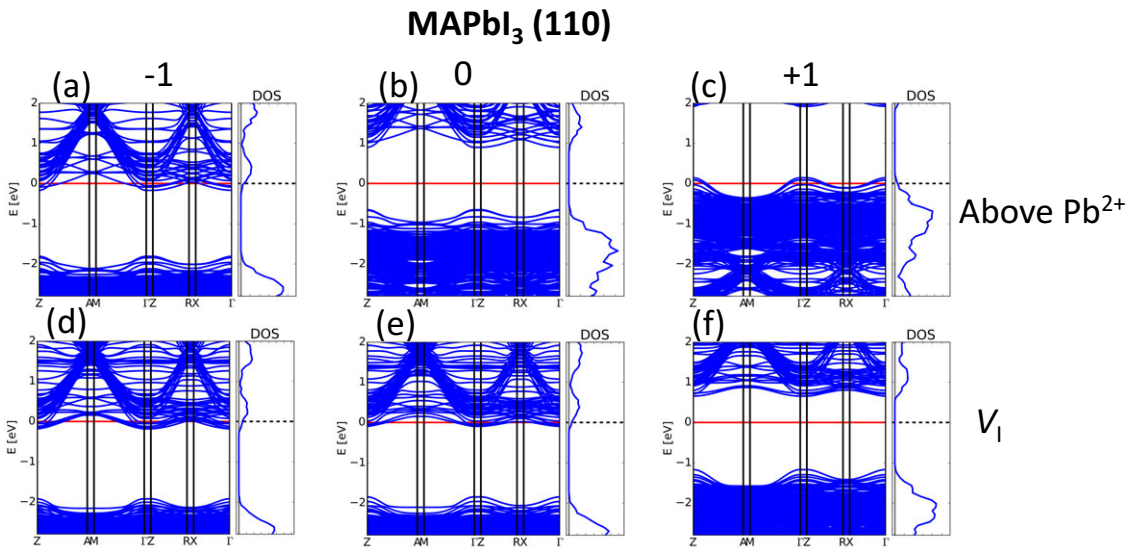

Figure B-6: Electronic structures and density of states (DOS) for the (110) surface of $MAPbI_3$ in the absence of any molecules. Columns 1, 2 and 3 correspond to the vacancies being negatively, neutral, and positively charged, respectively. (a)-(c) (row 1) corresponds to surface sites above Pb^{2+} on the PbI_2-terminated surface and (d)-(f) (row 2) in an iodine vacancy on defect-rich PbI_2 surface terminations. In the band structures the Fermi level is indicated by a red line.

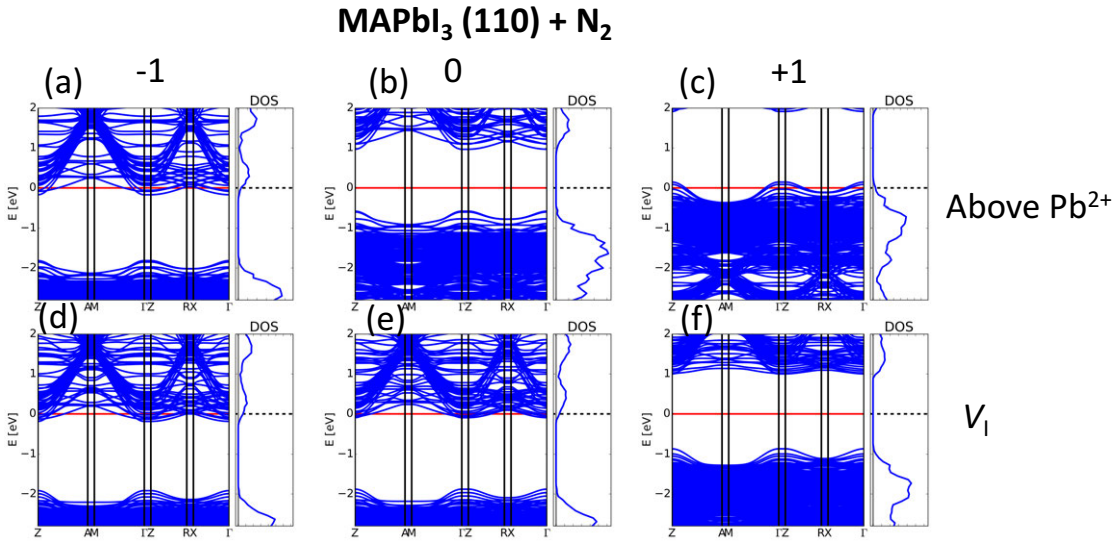

Figure B-7: Electronic structures and density of states (DOS) for the (110) surface of $MAPbI_3$ with adsorption of N_2. Columns 1, 2 and 3 correspond to the vacancies being negatively, neutral, and positively charged, respectively. (a)-(c) (row 1) corresponds to surface sites above Pb^{2+} on the PbI_2-terminated surface and (d)-(f) (row 2) in an iodine vacancy on defect-rich PbI_2 surface terminations. In the band structures the Fermi level is indicated by a red line.

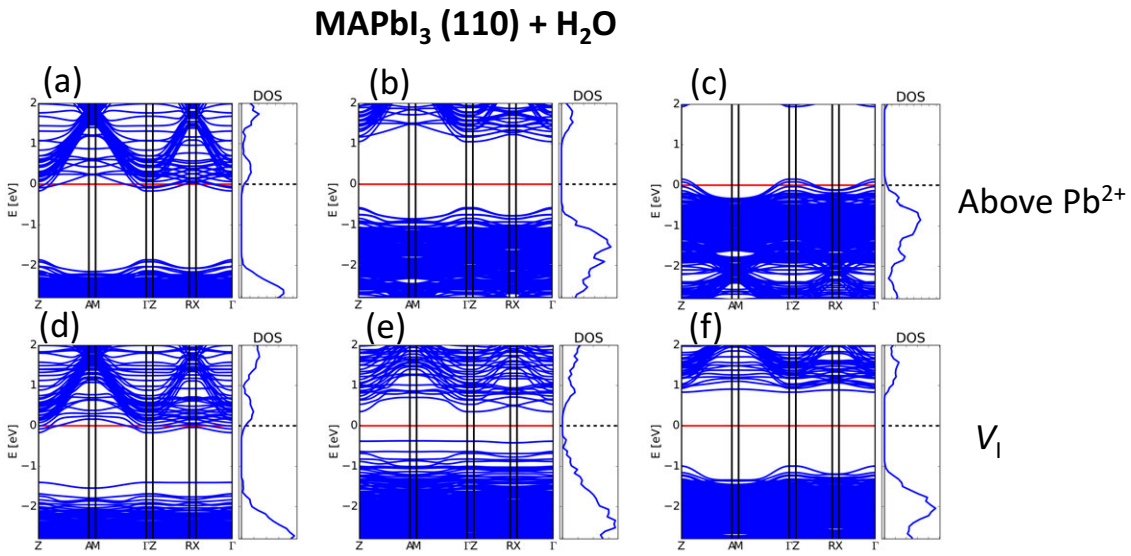

Figure B-8: Electronic structures and density of states (DOS) for the (110) surface of $MAPbI_3$ with adsorption of H_2O. Columns 1, 2 and 3 correspond to the vacancies being negatively, neutral, and positively charged, respectively. (a)-(c) (row 1) corresponds to surface sites above Pb^{2+} on the PbI_2-terminated surface and (d)-(f) (row 2) in an iodine vacancy on defect-rich PbI_2 surface terminations. In the band structures the Fermi level is indicated by a red line.

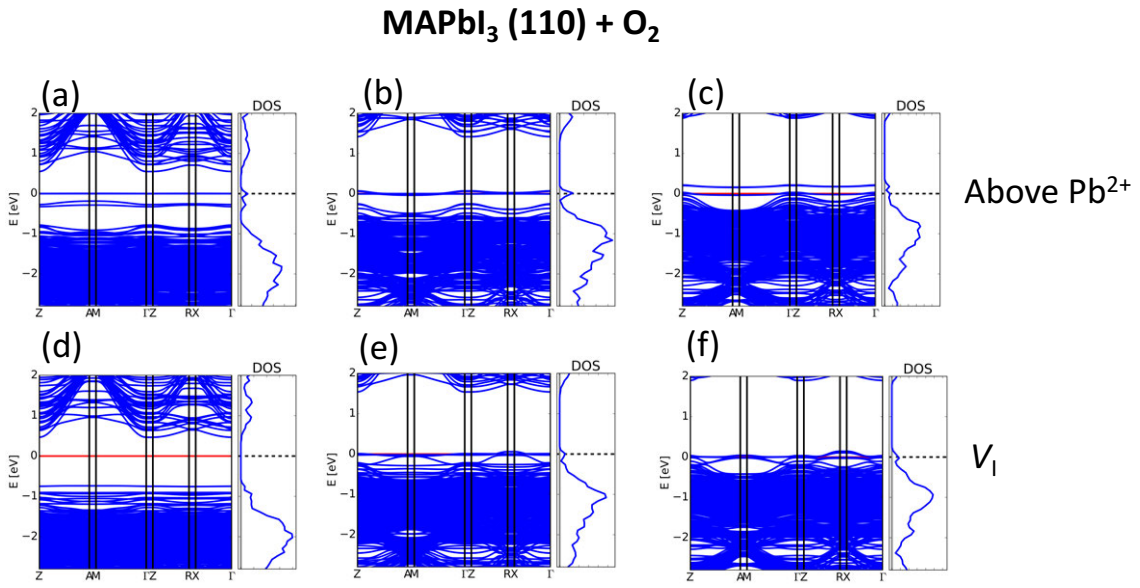

Figure B-9: Electronic structures and density of states (DOS) for the (110) surface of $MAPbI_3$ with adsorption of O_2. Columns 1, 2 and 3 correspond to the vacancies being negatively, neutral, and positively charged, respectively. (a)-(c) (row 1) corresponds to surface sites above Pb^{2+} on the PbI_2-terminated surface and (d)-(f) (row 2) in an iodine vacancy on defect-rich PbI_2 surface terminations. In the band structures the Fermi level is indicated by a red line.

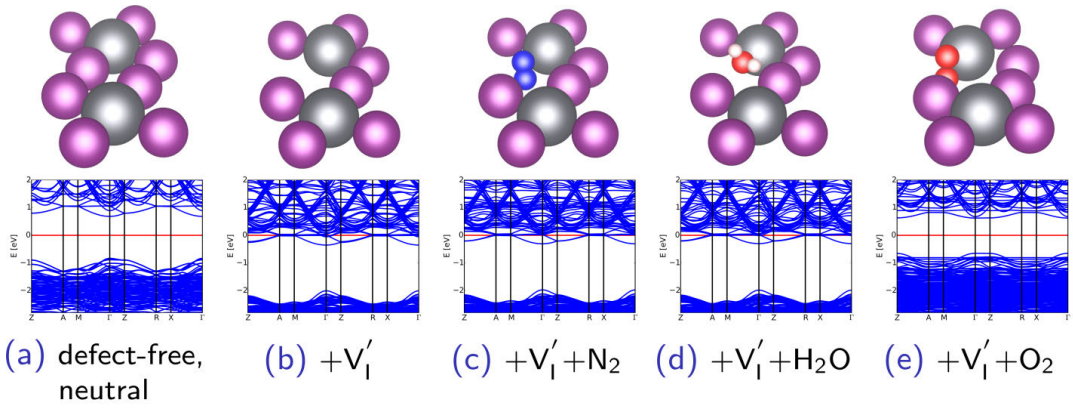

Figure B-10: (001) Surface atomic and electronic structures. Local atomic configuration in surface termination layer (top row) and band structure (bottom row) for the (001) surface of $MAPbI_3$ (cf. Figure 3-4 for (110) results). (a) Pristine uncharged surface, (b) negatively-charged iodine vacancy into which the following molecules are adsorbed; (c) N_2, (d) H_2O and (e) O_2. Key: purple - iodine, grey - lead, blue - nitrogen, red - oxygen, white - hydrogen. In the band structures the Fermi level is indicated by a red line.

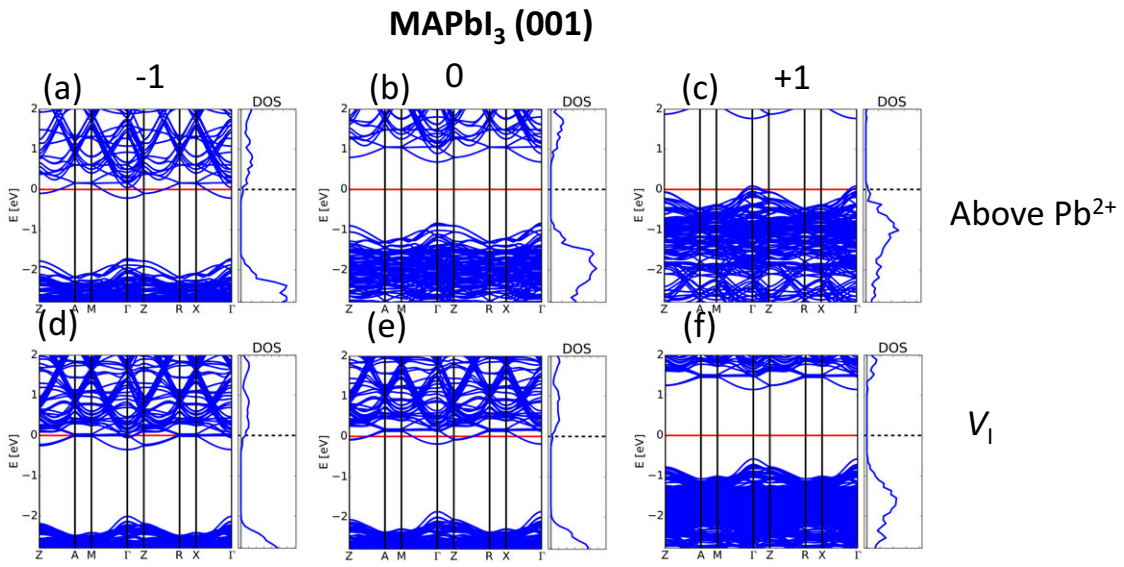

Figure B-11: Electronic structures and density of states (DOS) for the (001) surface of $MAPbI_3$ in the absence of any molecules. Columns 1, 2 and 3 correspond to the vacancies being negatively, neutral, and positively charged, respectively. (a)-(c) (row 1) corresponds to surface sites above Pb^{2+} on the PbI_2-terminated surface and (d)-(f) (row 2) in an iodine vacancy on defect-rich PbI_2 surface terminations. In the band structures the Fermi level is indicated by a red line.

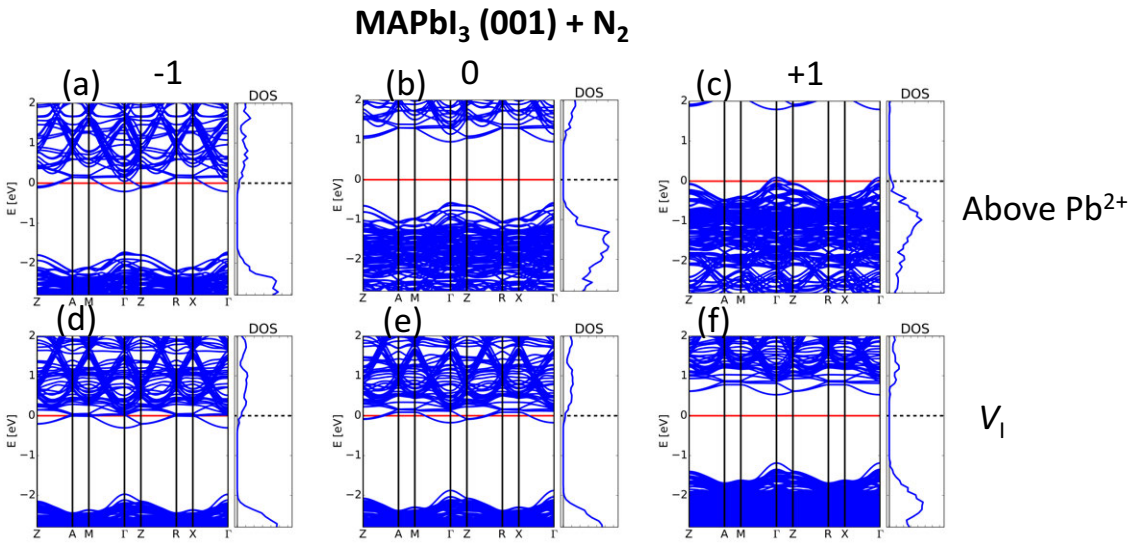

Figure B-12: Electronic structures and density of states (DOS) for the (001) surface of $MAPbI_3$ with adsorption of N_2. Columns 1, 2 and 3 correspond to the vacancies being negatively, neutral, and positively charged, respectively. (a)-(c) (row 1) corresponds to surface sites above Pb^{2+} on the PbI_2-terminated surface and (d)-(f) (row 2) in an iodine vacancy on defect-rich PbI_2 surface terminations. In the band structures the Fermi level is indicated by a red line.

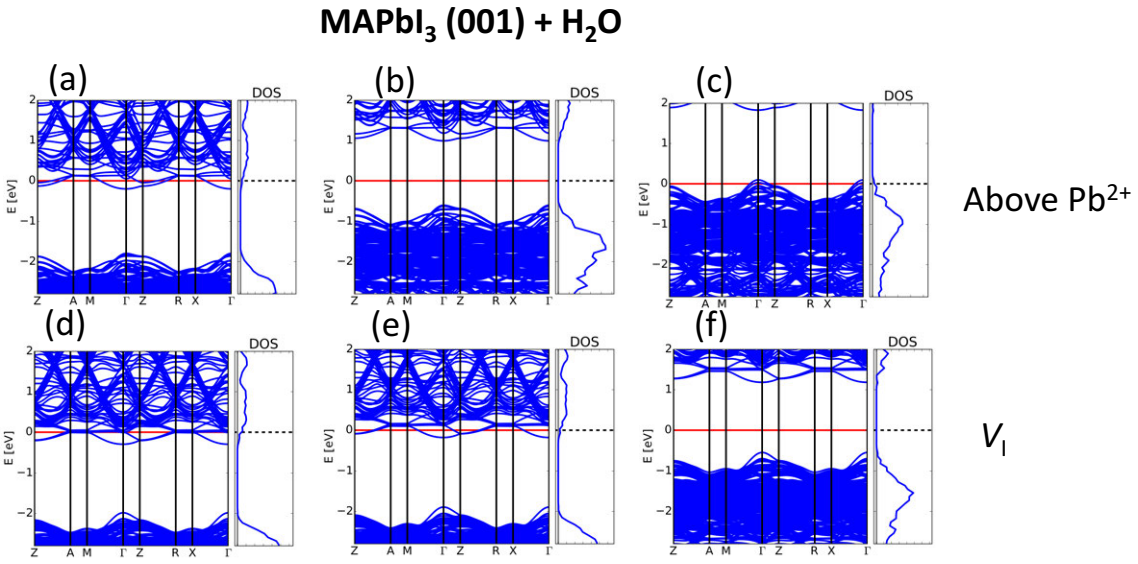

Figure B-13: Electronic structures and density of states (DOS) for the (001) surface of $MAPbI_3$ with adsorption of H_2O. Columns 1, 2 and 3 correspond to the vacancies being negatively, neutral, and positively charged, respectively. (a)-(c) (row 1) corresponds to surface sites above Pb^{2+} on the PbI_2-terminated surface and (d)-(f) (row 2) in an iodine vacancy on defect-rich PbI_2 surface terminations. In the band structures the Fermi level is indicated by a red line.

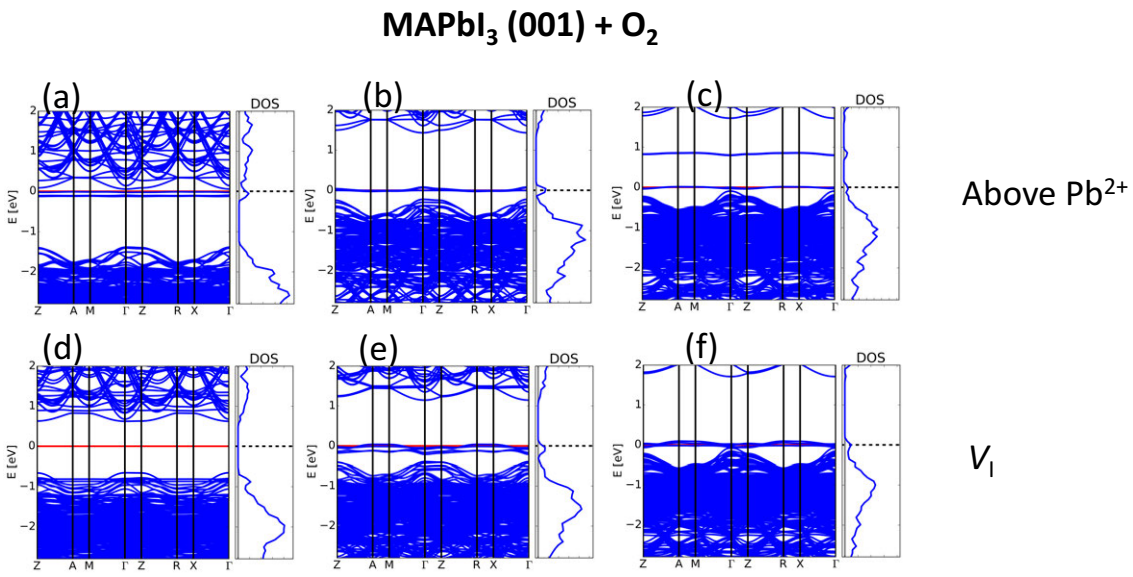

Figure B-14: Electronic structures and density of states (DOS) for the (001) surface of $MAPbI_3$ with adsorption of O_2. Columns 1, 2 and 3 correspond to the vacancies being negatively, neutral, and positively charged, respectively. (a)-(c) (row 1) corresponds to surface sites above Pb^{2+} on the PbI_2-terminated surface and (d)-(f) (row 2) in an iodine vacancy on defect-rich PbI_2 surface terminations. In the band structures the Fermi level is indicated by a red line.

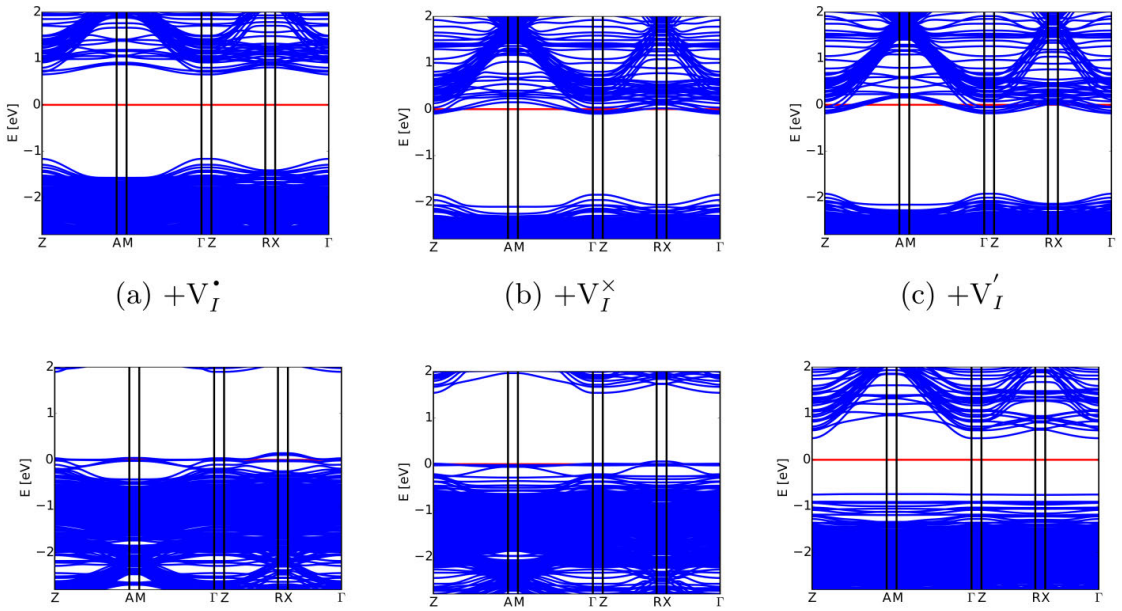

(a) $+V_I^{\bullet}$ (b) $+V_I^{\times}$ (c) $+V_I^{'}$

(d) $+V_I^{\bullet} + O_2$ (e) $+V_I^{\times} + O_2$ (f) $+V_I^{'} + O_2$

Figure B-15: Effect of vacancy charge state on photobrightening. Effect of iodine vacancy charge state on the photobrightening effect in an oxygen atmosphere on the (001) surface. All three types of surface vacancy (a-c) possess trap states. The photobrightening effect increases in the order: (d) positively charged, (e) neutral and (f) negatively charged (where we judge the effect by the final DOS near the Fermi level). In dark conditions all three charge states are possible but the intrinsic vacancy concentration will be much lower due to photo-induced iodine vacancy creation in the illuminated case.

Bibliography

[1] Michael L. Agiorgousis, Yi-Yang Sun, Hao Zeng, and Shengbai Zhang. Strong Covalency-Induced Recombination Centers in Perovskite Solar Cell Material CH 3 NH 3 PbI 3. *Journal of the American Chemical Society*, 136(41):14570–14575, oct 2014.

[2] Elham Halvani Anaraki, Ahmad Kermanpur, Ludmilla Steier, Konrad Domanski, Taisuke Matsui, Wolfgang Tress, Michael Saliba, Antonio Abate, Michael Grätzel, Anders Hagfeldt, and Juan-Pablo Correa-Baena. Highly efficient and stable planar perovskite solar cells by solution-processed tin oxide. *Energy & Environmental Science*, 9(10):3128–3134, 2016.

[3] Nicholas Aristidou, Christopher Eames, Irene Sanchez-Molina, Xiangnan Bu, Jan Kosco, M. Saiful Islam, and Saif A. Haque. Fast oxygen diffusion and iodide defects mediate oxygen-induced degradation of perovskite solar cells. *Nature Communications*, 8:15218, may 2017.

[4] Nicholas Aristidou, Irene Sanchez-Molina, Thana Chotchuangchutchaval, Michael Brown, Luis Martinez, Thomas Rath, and Saif A. Haque. The Role of Oxygen in the Degradation of Methylammonium Lead Trihalide Perovskite Photoactive Layers. *Angewandte Chemie - International Edition*, 2015.

[5] Kelsey K. Bass, R. Eric McAnally, Shiliang Zhou, Peter I. Djurovich, Mark E. Thompson, and Brent C. Melot. Influence of moisture on the preparation, crystal structure, and photophysical properties of organohalide perovskites. *Chem. Commun.*, 50(99):15819–15822, 2014.

[6] Andreas Baumann, Stefan Väth, Philipp Rieder, Michael C. Heiber, Kristofer Tvingstedt, and Vladimir Dyakonov. Identification of Trap States in Perovskite Solar Cells. *The Journal of Physical Chemistry Letters*, 6(12):2350–2354, jun 2015.

[7] Yu Bi, Eline M. Hutter, Yanjun Fang, Qingfeng Dong, Jinsong Huang, and Tom J. Savenije. Charge Carrier Lifetimes Exceeding 15 μs in Methylammonium Lead Iodide Single Crystals. *The Journal of Physical Chemistry Letters*, 7(5):923–928, mar 2016.

[8] Volker Blum, Ralf Gehrke, Felix Hanke, Paula Havu, Ville Havu, Xinguo Ren, Karsten Reuter, and Matthias Scheffler. Ab initio molecular simula-

tions with numeric atom-centered orbitals. *Computer Physics Communications*, 180(11):2175–2196, nov 2009.

[9] Geoffrey C. Bond. *Heterogeneous Catalysis*. Oxford University Press, Oxford, 1987.

[10] Ruy S. Bonilla, Frederick Woodcock, and Peter R. Wilshaw. Very low surface recombination velocity in n-type c-Si using extrinsic field effect passivation. *Journal of Applied Physics*, 116(5):054102, aug 2014.

[11] Michael Bowker. *The Basis and Applications of Heterogeneous Catalysis*. Oxford University Press, New York, 1998.

[12] BP. BP Statistical Review of World Energy. Technical report, 2017.

[13] Thomas M. Brenner, David A. Egger, Leeor Kronik, Gary Hodes, and David Cahen. Hybrid organic—inorganic perovskites: low-cost semiconductors with intriguing charge-transport properties. *Nature Reviews Materials*, 1(1):15007, jan 2016.

[14] Andrei Buin, Riccardo Comin, Jixian Xu, Alexander H. Ip, and Edward H. Sargent. Halide-Dependent Electronic Structure of Organolead Perovskite Materials. *Chemistry of Materials*, 27(12):4405–4412, jun 2015.

[15] Qi Chen, Huanping Zhou, Tze-Bin Song, Song Luo, Ziruo Hong, Hsin-Sheng Duan, Letian Dou, Yongsheng Liu, and Yang Yang. Controllable Self-Induced Passivation of Hybrid Lead Iodide Perovskites toward High Performance Solar Cells. *Nano Letters*, 14(7):4158–4163, jul 2014.

[16] Y. Chen, H. T. Yi, X. Wu, R. Haroldson, Y. N. Gartstein, Y. I. Rodionov, K. S. Tikhonov, A. Zakhidov, X. Y. Zhu, and V. Podzorov. Extended carrier lifetimes and diffusion in hybrid perovskites revealed by Hall effect and photoconductivity measurements. *Nature Communications*, 7(1):12253, dec 2016.

[17] Himchan Cho, S.-H. Jeong, M.-H. Park, Y.-H. Kim, Christoph Wolf, C.-L. Lee, Jin Hyuck Heo, Aditya Sadhanala, N. Myoung, Seunghyup Yoo, Sang Hyuk Im, Richard H. Friend, and T.-W. Lee. Overcoming the electroluminescence efficiency limitations of perovskite light-emitting diodes. *Science*, 350(6265):1222–1225, dec 2015.

[18] John C. de Mello, H. Felix Wittmann, and Richard H. Friend. An improved experimental determination of external photoluminescence quantum efficiency. *Advanced Materials*, 9(3):230–232, mar 1997.

[19] D. W. de Quilettes, Sarah M. Vorpahl, Samuel D. Stranks, Hirokazu Nagaoka, Giles E. Eperon, Mark E. Ziffer, Henry J. Snaith, and David S. Ginger. Impact of microstructure on local carrier lifetime in perovskite solar cells. *Science*, 348(6235):683–686, may 2015.

[20] Stefaan De Wolf, Jakub Holovsky, Soo-Jin Moon, Philipp Löper, Bjoern Niesen, Martin Ledinsky, Franz-Josef Haug, Jun-Ho Yum, and Christophe Ballif. Organometallic Halide Perovskites: Sharp Optical Absorption Edge and Its Relation to Photovoltaic Performance. *The Journal of Physical Chemistry Letters*, 5(6):1035–1039, mar 2014.

[21] Dane W. DeQuilettes, Susanne Koch, Sven Burke, Rajan K. Paranji, Alfred J. Shropshire, Mark E. Ziffer, and David S. Ginger. Photoluminescence Lifetimes Exceeding 8 μs and Quantum Yields Exceeding 30% in Hybrid Perovskite Thin Films by Ligand Passivation. *ACS Energy Letters*, 1(2):438–444, aug 2016.

[22] Dane W. DeQuilettes, Wei Zhang, Victor M. Burlakov, Daniel J. Graham, Tomas Leijtens, Anna Osherov, Vladimir Bulović, Henry J. Snaith, David S. Ginger, and Samuel D. Stranks. Photo-induced halide redistribution in organic–inorganic perovskite films. *Nature Communications*, 7(1):11683, dec 2016.

[23] Felix Deschler, Michael Price, Sandeep Pathak, Lina E. Klintberg, David-Dominik Jarausch, Ruben Higler, Sven Hüttner, Tomas Leijtens, Samuel D. Stranks, Henry J. Snaith, Mete Atatüre, Richard T. Phillips, and Richard H. Friend. High Photoluminescence Efficiency and Optically Pumped Lasing in Solution-Processed Mixed Halide Perovskite Semiconductors. *The Journal of Physical Chemistry Letters*, 5(8):1421–1426, apr 2014.

[24] Sergiu Draguta, Siddharatha Thakur, Yurii V. Morozov, Yuanxing Wang, Joseph S. Manser, Prashant V. Kamat, and Masaru Kuno. Spatially Non-uniform Trap State Densities in Solution-Processed Hybrid Perovskite Thin Films. *The Journal of Physical Chemistry Letters*, 7(4):715–721, feb 2016.

[25] Mao-Hua Du. Density Functional Calculations of Native Defects in CH 3 NH 3 PbI 3 : Effects of Spin–Orbit Coupling and Self-Interaction Error. *The Journal of Physical Chemistry Letters*, 6(8):1461–1466, apr 2015.

[26] Christopher Eames, Jarvist M. Frost, Piers R. F. Barnes, Brian C. O'Regan, Aron Walsh, and M. Saiful Islam. Ionic transport in hybrid lead iodide perovskite solar cells. *Nature Communications*, 6(1):7497, dec 2015.

[27] Giles E. Eperon, Severin N. Habisreutinger, Tomas Leijtens, Bardo J. Bruijnaers, Jacobus J. van Franeker, Dane W. DeQuilettes, Sandeep Pathak, Rebecca J. Sutton, Giulia Grancini, David S. Ginger, Rene A. J. Janssen, Annamaria Petrozza, and Henry J. Snaith. The Importance of Moisture in Hybrid Lead Halide Perovskite Thin Film Fabrication. *ACS Nano*, 9(9):9380–9393, sep 2015.

[28] Giles E. Eperon, David Moerman, and David S. Ginger. Anticorrelation between Local Photoluminescence and Photocurrent Suggests Variability in Contact to Active Layer in Perovskite Solar Cells. *ACS Nano*, 10(11):10258–10266, nov 2016.

[29] Hong-Hua Fang, Sampson Adjokatse, Haotong Wei, Jie Yang, Graeme R. Blake, Jinsong Huang, Jacky Even, and Maria Antonietta Loi. Ultrahigh sensitivity of methylammonium lead tribromide perovskite single crystals to environmental gases. *Science Advances*, 2(7):e1600534, jul 2016.

[30] Juan F. Galisteo-López, M. Anaya, M. E. Calvo, and H. Míguez. Environmental effects on the photophysics of organic-inorganic halide perovskites. *Journal of Physical Chemistry Letters*, 2015.

[31] Joseph L. Garrett, Elizabeth M. Tennyson, Miao Hu, Jinsong Huang, Jeremy N. Munday, and Marina S. Leite. Real-Time Nanoscale Open-Circuit Voltage Dynamics of Perovskite Solar Cells. *Nano Letters*, 17(4):2554–2560, apr 2017.

[32] G. Gordillo, C. A. Otálora, and A. A. Ramirez. A study of trap and recombination centers in MAPbI 3 perovskites. *Physical Chemistry Chemical Physics*, 18(48):32862–32867, 2016.

[33] Ronen Gottesman, Laxman Gouda, Basanth S. Kalanoor, Eynav Haltzi, Shay Tirosh, Eli Rosh-Hodesh, Yaakov Tischler, Arie Zaban, Claudio Quarti, Edoardo Mosconi, and Filippo De Angelis. Photoinduced Reversible Structural Transformations in Free-Standing CH 3 NH 3 PbI 3 Perovskite Films. *The Journal of Physical Chemistry Letters*, 6(12):2332–2338, jun 2015.

[34] G. Grancini, V. D'Innocenzo, E. R. Dohner, N. Martino, A. R. Srimath Kandada, E. Mosconi, F. De Angelis, H. I. Karunadasa, E. T. Hoke, and A. Petrozza. CH3NH3PbI3 perovskite single crystals: Surface photophysics and their interaction with the environment. *Chemical Science*, 2015.

[35] Wei Hao, Xiaodong Chen, and Shuzhou Li. Synergistic Effects of Water and Oxygen Molecule Co-adsorption on (001) Surfaces of Tetragonal CH 3 NH 3 PbI 3 : A First-Principles Study. *The Journal of Physical Chemistry C*, 120(50):28448–28455, dec 2016.

[36] Jun Haruyama, Keitaro Sodeyama, Liyuan Han, and Yoshitaka Tateyama. Surface Properties of CH 3 NH 3 PbI 3 for Perovskite Solar Cells. *Accounts of Chemical Research*, 49(3):554–561, mar 2016.

[37] Laura M. Herz. Charge-Carrier Mobilities in Metal Halide Perovskites: Fundamental Mechanisms and Limits. *ACS Energy Letters*, 2(7):1539–1548, jul 2017.

[38] Weixin Huang, Joseph S. Manser, Prashant V. Kamat, and Sylwia Ptasinska. Evolution of Chemical Composition, Morphology, and Photovoltaic Efficiency of CH3NH3PbI3Perovskite under Ambient Conditions. *Chemistry of Materials*, 2016.

[39] Eline M. Hutter, Giles E. Eperon, Samuel D. Stranks, and Tom J. Savenije. Charge Carriers in Planar and Meso-Structured Organic–Inorganic Perovskites:

Mobilities, Lifetimes, and Concentrations of Trap States. *The Journal of Physical Chemistry Letters*, 6(15):3082–3090, aug 2015.

[40] Eline M. Hutter, María C. Gélvez-Rueda, Anna Osherov, Vladimir Bulović, Ferdinand C. Grozema, Samuel D. Stranks, and Tom J. Savenije. Direct–indirect character of the bandgap in methylammonium lead iodide perovskite. *Nature Materials*, 16(1):115–120, jan 2017.

[41] IEA. World Energy Investment 2016. Technical report, 2016.

[42] Michael B. Johnston and Laura M. Herz. Hybrid Perovskites for Photovoltaics: Charge-Carrier Recombination, Diffusion, and Radiative Efficiencies. *Accounts of Chemical Research*, 49(1):146–154, jan 2016.

[43] Nathan Z. Koocher, Diomedes Saldana-Greco, Fenggong Wang, Shi Liu, and Andrew M. Rappe. Polarization Dependence of Water Adsorption to CH3NH3PbI3(001) Surfaces. *Journal of Physical Chemistry Letters*, 2015.

[44] Sibel Y. Leblebici, Linn Leppert, Yanbo Li, Sebastian E. Reyes-Lillo, Sebastian Wickenburg, Ed Wong, Jiye Lee, Mauro Melli, Dominik Ziegler, Daniel K. Angell, D. Frank Ogletree, Paul D. Ashby, Francesca M. Toma, Jeffrey B. Neaton, Ian D. Sharp, and Alexander Weber-Bargioni. Facet-dependent photovoltaic efficiency variations in single grains of hybrid halide perovskite. *Nature Energy*, 2016.

[45] Aurélien M. A. Leguy, Yinghong Hu, Mariano Campoy-Quiles, M. Isabel Alonso, Oliver J. Weber, Pooya Azarhoosh, Mark van Schilfgaarde, Mark T. Weller, Thomas Bein, Jenny Nelson, Pablo Docampo, and Piers R. F. Barnes. Reversible Hydration of CH 3 NH 3 PbI 3 in Films, Single Crystals, and Solar Cells. *Chemistry of Materials*, 27(9):3397–3407, may 2015.

[46] Tomas Leijtens, Giles E. Eperon, Alex J. Barker, Giulia Grancini, Wei Zhang, James M. Ball, Ajay Ram Srimath Kandada, Henry J. Snaith, and Annamaria Petrozza. Carrier trapping and recombination: the role of defect physics in enhancing the open circuit voltage of metal halide perovskite solar cells. *Energy & Environmental Science*, 9(11):3472–3481, 2016.

[47] Tomas Leijtens, Eric T. Hoke, Giulia Grancini, Daniel J. Slotcavage, Giles E. Eperon, James M. Ball, Michele De Bastiani, Andrea R. Bowring, Nicola Martino, Konrad Wojciechowski, Michael D. McGehee, Henry J. Snaith, and Annamaria Petrozza. Mapping Electric Field-Induced Switchable Poling and Structural Degradation in Hybrid Lead Halide Perovskite Thin Films. *Advanced Energy Materials*, 5(20):1500962, oct 2015.

[48] Richard I Masel. Principles of Adsorption and Reaction on Solid Surfaces. *Wiley Series in Chemical Engineering*, 1996.

[49] Owen D. Miller, Eli Yablonovitch, and Sarah R. Kurtz. Strong internal and external luminescence as solar cells approach the Shockley-Queisser limit. *IEEE Journal of Photovoltaics*, 2012.

[50] MIT. The Future of Solar Energy. *MIT Energy Institues*, 2015.

[51] Edoardo Mosconi, Jon M. Azpiroz, and Filippo De Angelis. Ab Initio Molecular Dynamics Simulations of Methylammonium Lead Iodide Perovskite Degradation by Water. *Chemistry of Materials*, 27(13):4885–4892, jul 2015.

[52] Edoardo Mosconi, Daniele Meggiolaro, Henry J. Snaith, Samuel D. Stranks, and Filippo De Angelis. Light-induced annihilation of Frenkel defects in organo-lead halide perovskites. *Energy & Environmental Science*, 9(10):3180–3187, 2016.

[53] Silvia G. Motti, Marina Gandini, Alex J. Barker, James M. Ball, Ajay Ram Srimath Kandada, and Annamaria Petrozza. Photoinduced Emissive Trap States in Lead Halide Perovskite Semiconductors. *ACS Energy Letters*, 2016.

[54] Christian Müller, Tobias Glaser, Marcel Plogmeyer, Michael Sendner, Sebastian Döring, Artem A. Bakulin, Carlo Brzuska, Roland Scheer, Maxim S. Pshenichnikov, Wolfgang Kowalsky, Annemarie Pucci, and Robert Lovrinčić. Water Infiltration in Methylammonium Lead Iodide Perovskite: Fast and Inconspicuous. *Chemistry of Materials*, 27(22):7835–7841, nov 2015.

[55] David Berney Needleman, Jeremy R. Poindexter, Rachel C. Kurchin, I. Marius Peters, Gregory Wilson, and Tonio Buonassisi. Economically sustainable scaling of photovoltaics to meet climate targets. In *2017 IEEE 44th Photovoltaic Specialist Conference (PVSC)*, pages 1–5. IEEE, jun 2017.

[56] Jenny Nelson. *The Physics of Solar Cells*. Number November. PUBLISHED BY IMPERIAL COLLEGE PRESS AND DISTRIBUTED BY WORLD SCIENTIFIC PUBLISHING CO., may 2003.

[57] Annie Ng, Zhiwei Ren, Qian Shen, Sin Hang Cheung, Huseyin Cem Gokkaya, Shu Kong So, Aleksandra B. Djurišić, Yangyang Wan, Xiaojun Wu, and Charles Surya. Crystal Engineering for Low Defect Density and High Efficiency Hybrid Chemical Vapor Deposition Grown Perovskite Solar Cells. *ACS Applied Materials & Interfaces*, 8(48):32805–32814, dec 2016.

[58] Wanyi Nie, Jean-Christophe Blancon, Amanda J. Neukirch, Kannatassen Appavoo, Hsinhan Tsai, Manish Chhowalla, Muhammad A. Alam, Matthew Y. Sfeir, Claudine Katan, Jacky Even, Sergei Tretiak, Jared J. Crochet, Gautam Gupta, and Aditya D. Mohite. Light-activated photocurrent degradation and self-healing in perovskite solar cells. *Nature Communications*, 7(1):11574, dec 2016.

[59] Wanyi Nie, Hsinhan Tsai, Reza Asadpour, J.-C. Blancon, Amanda J. Neukirch, Gautam Gupta, Jared J. Crochet, Manish Chhowalla, Sergei Tretiak, Muhammad A. Alam, H.-L. Wang, and Aditya D. Mohite. High-efficiency solution-processed perovskite solar cells with millimeter-scale grains. *Science*, 347(6221):522–525, jan 2015.

[60] Nakita K. Noel, Antonio Abate, Samuel D. Stranks, Elizabeth S. Parrott, Victor M. Burlakov, Alain Goriely, and Henry J. Snaith. Enhanced Photoluminescence and Solar Cell Performance via Lewis Base Passivation of Organic–Inorganic Lead Halide Perovskites. *ACS Nano*, 8(10):9815–9821, oct 2014.

[61] Nakita K. Noel, Severin N. Habisreutinger, Bernard Wenger, Matthew T. Klug, Maximilian T. Hörantner, Michael B. Johnston, Robin J. Nicholas, David T. Moore, and Henry J. Snaith. A low viscosity, low boiling point, clean solvent system for the rapid crystallisation of highly specular perovskite films. *Energy & Environmental Science*, 10(1):145–152, 2017.

[62] NREL. Solar cell efficiency chart. *Solar cell efficiency chart*, 2017.

[63] L. M. Pazos-Outon, Monika Szumilo, Robin Lamboll, Johannes M. Richter, Micaela Crespo-Quesada, Mojtaba Abdi-Jalebi, Harry J. Beeson, M. Vru ini, Mejd Alsari, Henry J. Snaith, Bruno Ehrler, Richard H. Friend, and Felix Deschler. Photon recycling in lead iodide perovskite solar cells. *Science*, 351(6280):1430–1433, mar 2016.

[64] John P. Perdew, Kieron Burke, and Matthias Ernzerhof. Generalized Gradient Approximation Made Simple. *Physical Review Letters*, 77(18):3865–3868, oct 1996.

[65] Michiel L. Petrus, Yinghong Hu, Davide Moia, Philip Calado, Aurélien M. A. Leguy, Piers R. F. Barnes, and Pablo Docampo. The Influence of Water Vapor on the Stability and Processing of Hybrid Perovskite Solar Cells Made from Non-Stoichiometric Precursor Mixtures. *ChemSusChem*, 9(18):2699–2707, sep 2016.

[66] Obadiah G. Reid, Mengjin Yang, Nikos Kopidakis, Kai Zhu, and Garry Rumbles. Grain-Size-Limited Mobility in Methylammonium Lead Iodide Perovskite Thin Films. *ACS Energy Letters*, 1(3):561–565, sep 2016.

[67] Xinguo Ren, Patrick Rinke, Volker Blum, Jürgen Wieferink, Alexandre Tkatchenko, Andrea Sanfilippo, Karsten Reuter, and Matthias Scheffler. Resolution-of-identity approach to Hartree–Fock, hybrid density functionals, RPA, MP2 and GW with numeric atom-centered orbital basis functions. *New Journal of Physics*, 14(5):053020, may 2012.

[68] Johannes M. Richter, Mojtaba Abdi-Jalebi, Aditya Sadhanala, Maxim Tabachnyk, Jasmine P.H. Rivett, Luis M. Pazos-Outón, Karl C. Gödel, Michael Price,

Felix Deschler, and Richard H. Friend. Enhancing photoluminescence yields in lead halide perovskites by photon recycling and light out-coupling. *Nature Communications*, 2016.

[69] Norina A. Richter, Sabrina Sicolo, Sergey V. Levchenko, Joachim Sauer, and Matthias Scheffler. Concentration of vacancies at metal-oxide surfaces: Case study of MgO(100). *Physical Review Letters*, 2013.

[70] Michael Saliba, Taisuke Matsui, Konrad Domanski, J.-Y. Seo, Amita Ummadisingu, Shaik M. Zakeeruddin, J.-P. Correa-Baena, Wolfgang R. Tress, Antonio Abate, Anders Hagfeldt, and M. Gratzel. Incorporation of rubidium cations into perovskite solar cells improves photovoltaic performance. *Science*, 354(6309):206–209, oct 2016.

[71] Denis Semwogerere and Eric R Weeks. Confocal Microscopy. *Encyclopedia of Biomaterials and Biomedical Engineering*, pages 1–10, 2005.

[72] Limin She, Meizhuang Liu, and Dingyong Zhong. Atomic Structures of CH 3 NH 3 PbI 3 (001) Surfaces. *ACS Nano*, 10(1):1126–1131, jan 2016.

[73] Dong Shi, Valerio Adinolfi, Riccardo Comin, Mingjian Yuan, Erkki Alarousu, Andrei Buin, Yin Chen, Sjoerd Hoogland, Alexander Rothenberger, Khabiboulakh Katsiev, Yaroslav Losovyj, Xin Zhang, Peter A. Dowben, Omar F. Mohammed, Edward H. Sargent, and Osman M. Bakr. Low trap-state density and long carrier diffusion in organolead trihalide perovskite single crystals. *Science*, 347(6221):519–522, jan 2015.

[74] Henry J. Snaith, Antonio Abate, James M. Ball, Giles E. Eperon, Tomas Leijtens, Nakita K. Noel, Samuel D. Stranks, Jacob Tse-Wei Wang, Konrad Wojciechowski, and Wei Zhang. Anomalous Hysteresis in Perovskite Solar Cells. *The Journal of Physical Chemistry Letters*, 5(9):1511–1515, may 2014.

[75] Samuel D. Stranks. Nonradiative Losses in Metal Halide Perovskites. *ACS Energy Letters*, 2(7):1515–1525, jul 2017.

[76] Samuel D. Stranks, Victor M. Burlakov, Tomas Leijtens, James M. Ball, Alain Goriely, and Henry J. Snaith. Recombination Kinetics in Organic-Inorganic Perovskites: Excitons, Free Charge, and Subgap States. *Physical Review Applied*, 2(3):034007, sep 2014.

[77] Samuel D. Stranks, Giles E. Eperon, Giulia Grancini, Christopher Menelaou, Marcelo J P Alcocer, Tomas Leijtens, Laura M. Herz, Annamaria Petrozza, and Henry J. Snaith. Electron-Hole Diffusion Lengths Exceeding 1 Micrometer in an Organometal Trihalide Perovskite Absorber. *Science*, 342(6156):341–344, oct 2013.

[78] Samuel D. Stranks, Pabitra K. Nayak, Wei Zhang, Thomas Stergiopoulos, and Henry J. Snaith. Formation of Thin Films of Organic-Inorganic Perovskites

for High-Efficiency Solar Cells. *Angewandte Chemie International Edition*, 54(11):3240–3248, mar 2015.

[79] Samuel D. Stranks and Henry J. Snaith. Metal-halide perovskites for photovoltaic and light-emitting devices. *Nature Nanotechnology*, 10(5):391–402, may 2015.

[80] Brandon R. Sutherland and Edward H. Sargent. Perovskite photonic sources, 2016.

[81] Carolin M. Sutter-Fella, Yanbo Li, Matin Amani, Joel W. Ager, Francesca M. Toma, Eli Yablonovitch, Ian D. Sharp, and Ali Javey. High Photoluminescence Quantum Yield in Band Gap Tunable Bromide Containing Mixed Halide Perovskites. *Nano Letters*, 16(1):800–806, jan 2016.

[82] Yuxi Tian, Maximilian Peter, Eva Unger, Mohamed Abdellah, Kaibo Zheng, Tõnu Pullerits, Arkady Yartsev, Villy Sundström, and Ivan G. Scheblykin. Mechanistic insights into perovskite photoluminescence enhancement: light curing with oxygen can boost yield thousandfold. *Physical Chemistry Chemical Physics*, 17(38):24978–24987, 2015.

[83] Alexandre Tkatchenko, Alberto Ambrosetti, and Robert A. DiStasio. Interatomic methods for the dispersion energy derived from the adiabatic connection fluctuation-dissipation theorem. *The Journal of Chemical Physics*, 138(7):074106, feb 2013.

[84] Hiroki Uratani and Koichi Yamashita. Charge Carrier Trapping at Surface Defects of Perovskite Solar Cell Absorbers: A First-Principles Study. *The Journal of Physical Chemistry Letters*, 8(4):742–746, feb 2017.

[85] K. Vandewal, L. Goris, I. Haeldermans, M. Nesládek, K. Haenen, P. Wagner, and J.V. Manca. Fourier-Transform Photocurrent Spectroscopy for a fast and highly sensitive spectral characterization of organic and hybrid solar cells. *Thin Solid Films*, 516(20):7135–7138, aug 2008.

[86] Michael Wahl. Time-correlated Single Photon Counting. *PicoQuant GmbH Technical Note*, 2014.

[87] Nana Wang, Lu Cheng, Rui Ge, Shuting Zhang, Yanfeng Miao, Wei Zou, Chang Yi, Yan Sun, Yu Cao, Rong Yang, Yingqiang Wei, Qiang Guo, You Ke, Maotao Yu, Yizheng Jin, Yang Liu, Qingqing Ding, Dawei Di, Le Yang, Guichuan Xing, He Tian, Chuanhong Jin, Feng Gao, Richard H. Friend, Jianpu Wang, and Wei Huang. Perovskite light-emitting diodes based on solution-processed self-organized multiple quantum wells. *Nature Photonics*, 10(11):699–704, nov 2016.

[88] Robert H Webb. Confocal optical microscopy. *Reports on Progress in Physics*, 59(3):427–471, mar 1996.

[89] Gert Jan A.H. Wetzelaer, Max Scheepers, Araceli Miquel Sempere, Cristina Momblona, Jorge Ávila, and Henk J. Bolink. Trap-Assisted Non-Radiative Recombination in Organic-Inorganic Perovskite Solar Cells. *Advanced Materials*, 2015.

[90] Xiaoxi Wu, M. Tuan Trinh, Daniel Niesner, Haiming Zhu, Zachariah Norman, Jonathan S. Owen, Omer Yaffe, Bryan J. Kudisch, and X. Y. Zhu. Trap states in lead iodide perovskites. *Journal of the American Chemical Society*, 2015.

[91] Zhengguo Xiao, Ross A. Kerner, Lianfeng Zhao, Nhu L. Tran, Kyung Min Lee, Tae-Wook Koh, Gregory D. Scholes, and Barry P. Rand. Efficient perovskite light-emitting diodes featuring nanometre-sized crystallites. *Nature Photonics*, 11(2):108–115, feb 2017.

[92] E. Yablonovitch, D. L. Allara, C. C. Chang, T. Gmitter, and T. B. Bright. Unusually Low Surface-Recombination Velocity on Silicon and Germanium Surfaces. *Physical Review Letters*, 57(2):249–252, jul 1986.

[93] Yasuhiro Yamada, Masaru Endo, Atsushi Wakamiya, and Yoshihiko Kanemitsu. Spontaneous Defect Annihilation in CH 3 NH 3 PbI 3 Thin Films at Room Temperature Revealed by Time-Resolved Photoluminescence Spectroscopy. *The Journal of Physical Chemistry Letters*, 6(3):482–486, feb 2015.

[94] Mengjin Yang, Yining Zeng, Zhen Li, Dong Hoe Kim, Chun-Sheng Jiang, Jao van de Lagemaat, and Kai Zhu. Do grain boundaries dominate non-radiative recombination in CH 3 NH 3 PbI 3 perovskite thin films? *Physical Chemistry Chemical Physics*, 19(7):5043–5050, 2017.

[95] Woon Seok Yang, Byung Wook Park, Eui Hyuk Jung, Nam Joong Jeon, Young Chan Kim, Dong Uk Lee, Seong Sik Shin, Jangwon Seo, Eun Kyu Kim, Jun Hong Noh, and Sang Il Seok. Iodide management in formamidinium-lead-halide-based perovskite layers for efficient solar cells. *Science*, 2017.

[96] Ye Yang, Mengjin Yang, David T. Moore, Yong Yan, Elisa M. Miller, Kai Zhu, and Matthew C. Beard. Top and bottom surfaces limit carrier lifetime in lead iodide perovskite films. *Nature Energy*, 2(2):16207, feb 2017.

[97] Wan-Jian Yin, Tingting Shi, and Yanfa Yan. Unusual defect physics in CH 3 NH 3 PbI 3 perovskite solar cell absorber. *Applied Physics Letters*, 104(6):063903, feb 2014.

[98] Jingbi You, Yang (Michael) Yang, Ziruo Hong, Tze-Bin Song, Lei Meng, Yongsheng Liu, Chengyang Jiang, Huanping Zhou, Wei-Hsuan Chang, Gang Li, and Yang Yang. Moisture assisted perovskite film growth for high performance solar cells. *Applied Physics Letters*, 105(18):183902, nov 2014.

[99] Linghai Zhang and Patrick H.L. Sit. Ab initio study of the role of oxygen and excess electrons in the degradation of CH 3 NH 3 PbI 3. *Journal of Materials Chemistry A*, 5(19):9042–9049, 2017.

[100] Wei Zhang, Sandeep Pathak, Nobuya Sakai, Thomas Stergiopoulos, Pabitra K. Nayak, Nakita K. Noel, Amir A. Haghighirad, Victor M. Burlakov, Dane W. DeQuilettes, Aditya Sadhanala, Wenzhe Li, Liduo Wang, David S. Ginger, Richard H. Friend, and Henry J. Snaith. Enhanced optoelectronic quality of perovskite thin films with hypophosphorous acid for planar heterojunction solar cells. *Nature Communications*, 6(1):10030, dec 2015.

[101] Zhenxuan Zhao, Xiangyu Chen, Huaqiang Wu, Xiaoming Wu, and Guozhong Cao. Probing the Photovoltage and Photocurrent in Perovskite Solar Cells with Nanoscale Resolution. *Advanced Functional Materials*, 26(18):3048–3058, may 2016.